The University Of Sheffield.

Strain Based Control of Magnetic Domain Walls

By:

James Wheelwright

A thesis submitted in partial fulfilment of the requirements for the degree of Doctor of Philosophy

The University of Sheffield
Faculty of Engineering
Department of Materials Science and Engineering

October 2015

Abstract

This work investigates the applicability of strain induced magnetic anisotropy in the control of magnetic domain walls in magnetically soft magnetostrictive nanostructures. The mechanical coupling of piezoelectric and magnetostrictive materials is investigated as a method of controlling the strain in the magnetic material. Two systems have been investigated. The first is a magnetic nanoring containing two transverse magnetic domain walls subjected to uniaxial strain and a rotating field. For this system an analytical model and finite element analysis are used to predict the effect of strain induced anisotropy on the domain walls. Experimental data for the system has also been presented. The second system is a notched magnetic nanowire subjected to uniaxial strain. The change depinning fields of domain walls from the notch at varying strains have been simulated and measured experimentally.

Acknowledgements

First and foremost I would like to thank my supervisor Prof. Dan Allwood for his help and support throughout my PhD and during my master's project. His knowledge and guidance has been invaluable to over the past years. I would also like to thank Prof. Mike Gibbs for his expert knowledge regarding magnetostriction and METGLAS in particular and also for his inspiring presence as my tutor during my first undergraduate year.

I would like to thank all of my colleagues in the SCAMMD research group with particular thanks to Dr Tom Hayward, Dr Matt Bryan and Dr Julian Dean for their help with learning many of the experimental methods used in my studies. I would also like to thank Dr Matt Hodges, Ruth Bradley and TJ for their support and friendship during my PhD.

Thanks also to Dr Andrew Rushforth for his offer of collaborative work, Dr. Mark Rosamond for his exceptional EBL skills, Paul Hawksworth for his skill and cheer and Dr Paul Fry for his assistance learning to use the cleanroom.

Thanks also to my family for their care and support throughout the years. And a final thankyou to my wonderful fiancé Isabel Virgo for her help and for her invaluable presence throughout my studies.

Contents

1 - Introduction

Nanoscale soft magnetic elements offer well defined magnetic domain configurations due to the strong shape anisotropy provided by their dimensions[1] and the limiting of domain walls provided by their small size[1]. These structures have generated much interest due to the possibility of data storage using the magnetisation states in nanostructures to encode data[3][4]. Due to this much work has been done on the control of the magnetic states of magnetic nanostructures in order to achieve reliable and repeatable encoding of data[3][4]. One of the most well studied systems with potential for data storage is the lithographically defined magnetic nanowire, i.e. a strip of soft magnetic material with very high length relative to its thickness and width dimensions. The strong shape anisotropy of a nanowire provides a single easy axis along the length of the wire allowing magnetisation in either direction. It has been suggested that domain walls in a nanowire could provide a non-volatile means of storing data with the potential for extremely high aerial density[3]. Because of this the control of domain walls in nanowires is of particular interest. It has been shown that domain walls can be moved through nanowires using an applied magnetic field[5] or by electric current (utilising the spin transfer torque effect)[6] and that the domain walls can be further controlled using artificial defects such as notches in the wire to pin domain walls in place[7]. Strain induced magnetic anisotropy has also been suggested as a novel method of controlling domain walls in nanowires with magnetic anisotropy gradients being a mechanism of both driving domain walls through the wire and providing pinning sites for the domain walls[8]. It was suggested that magnetostrictive nanowires coupled to a piezoelectric substrate could be locally strained in order to induce local strain induced anisotropy allowing for tuneable and switchable control of domain walls.

This work contains studies on the potential for strain induced anisotropy in control of magnetic domain walls in soft magnetostrictive nanowires.

In the second chapter some of the basic concepts of magnetic theory are outlined.

The third chapter contains a review of the literature relevant to applications utilising strain induced anisotropy and magnetic based memory devices. The first part reviews literature on magnetic nanowires and in particular the control of domain walls in nanowires. The second part then focuses on previous work on soft magnetic nanorings, which offer a potentially useful system in which to study the behaviour of domain walls in a magnetic anisotropy gradient. The third part considers the literature of 'multiferroic' materials in which piezoelectric and magnetostrictive properties are coupled allowing electronic control of magnetisation or magnetic control of electric polarisation[9] . This includes true multiferroics (homogeneous materials with both piezoelectric and magnetostrictive properties) and artificial multiferroics (materials which are a composite of mechanically coupled piezoelectric and magnetostrictive materials). The fourth part of this reviews the literature on magnetic random access memory with a focus on domain wall based memory. The fifth and sixth parts appraise the literature relating to the magnetostrictive properties of Metglas, an amorphous alloy of iron, and Galfenol, an alloy of iron and gallium, respectively. The seventh and final part reviews the literature on the fatigue of thin films, which is a potentially limiting factor on the lifetime of devices operated by repeatedly straining a magnetic element.

Chapter four contains details of the experimental methods used in this work.

In the fifth chapter magnetic nanorings are proposed as a system for studying the effects of an anisotropy gradient on the behaviour of domain walls in a magnetic nanowire. A nanoring is a form of curved nanowire and it is proposed that application of a uniaxial strain induced anisotropy to the ring system subjects domain walls in the ring to an anisotropy gradient. An experiment was proposed wherein an in-plane rotating magnetic field, producing a well defined response in unstrained rings, is used to probe the effect of induced magnetic anisotropy on the behaviour of domain walls with the perturbation of the system from the behaviour of an unstrained system provides a measurement for the effect of the anisotropy. Both analytical and finite element modelling were used in order to predict the effects of anisotropy gradients on transverse domain walls and to suggest ways to optimise the effect of strain induced magnetic anisotropy on domain walls. Initial experimental results are presented showing the effect of uniaxial strain on an array of Ni rings.

The sixth chapter proposes that uniaxial strain induced magnetic anisotropy has the potential to alter the depinning behaviour of magnetic domain walls from artificial pinning sites in soft magnetic nanowires. Finite element simulations are presented analysing the effect of uniaxial magnetic anisotropy on the depinning of transverse domain walls in wires with varying width and notch dimensions. Experimental data are also presented for the depinning of vortex domain walls from triangular notches in magnetic nanowires with varying notch depths and wire widths. From these results suggestions have been made for the optimisation of the control of domain wall depinning using strain induced uniaxial magnetic anisotropy in notched magnetic nanowires.

Chapter seven summarises the main outcomes of the experimental chapters five and six and also considers future work that emerges.

1.2 References

[1] R P Cowburn, *J. Phys. D: Appl. Phys.*, **33**, R1 (2000) [3] D.Atkinson, D.S.Eastwood and L.K.Bogart, *Appl. Phys. Lett.*, **92**, 022510 (2008)

[4] S. P. Parkin, M.Hayashi and L.Thomas, *Science*, **320**, 190 (2008)

[5] D.Atkinson, D.A.Allwood, G.Xiong, M.D.Cooke, C.C.Faulkner and R.P.Cowburn, *Nat. Mater.*, **2**, 85 (2003)

[6] N.Vernier, D.A.Allwood, D.Atkinson, M.D.Cooke and R.P.Cowburn, *Europhys. Lett.*, **65**, 526 (2004)

[7] A.Himeno, T.Ono, S.Nasu, K.Shigeto, K.Mibu, and T.Shinjo, *J. App. Phys.*, **93**, 8430 (2003)

[8] J.Dean, M.T.Bryan, T.Schrefl and D.A.Allwood, *J. Appl. Phys.*, **109**, 023915 (2011)

[9] C.Nan, M.I.Bichurin, S.Dong, D.Viehland and G.Srinivasan, *J. Appl. Phys.*, **103**, 031101 (2008)

2 - Background

2.1 - Magnetism

Magnetic phenomena have been known since ancient times when it was observed that the mineral magnetite could attract iron[1]. Later it was observed that an electric current produces a similar effect[1]. In both of these examples a magnetic field is responsible for the observed effect. A magnetic field $\boldsymbol{H}$ is accompanied by a magnetic induction $\boldsymbol{B}$ which in free space is[1]:

$$\boldsymbol{B} = \mu_0 \boldsymbol{H} \tag{2.1}$$

where μ_0 is the permeability of free space ($4\pi \times 10^{-7}$ N/A^2). Within a magnetic material the magnetic induction is[1]:

$$\boldsymbol{B} = \mu_0 (\boldsymbol{H} + \boldsymbol{M}) \tag{2.2}$$

where $\boldsymbol{M}$ is the magnetisation of the material. Materials can be characterised by their response to a magnetic field. The ratio of $\boldsymbol{M}$ to $\boldsymbol{H}$ is known as the susceptibility χ and indicates how responsive a material is to an applied magnetic field. Depending on the type of magnetism present in the material (which will be discussed below) this response may be linear or non-linear.[1]

The magnetisation in an atom arises due to the orbital angular momenta of the electrons orbiting the nucleus of the atom and the spin of the electrons themselves. The orbital momentum and spin of an electron combine to give the total angular momentum of an

electron and the combination of the angular momenta of the electrons gives the magnetic dipole moment of the atom. Due to the pairing of electrons in the electron shells of atoms only atoms with incomplete shells will have magnetic dipoles as the paired electrons' contributions cancel each other out.[2]

2.2 - Diamagnetism

The magnetisation in a diamagnetic material arises in opposition to any applied magnetic field and is proportional to the applied field. The magnetisation of a diamagnetic material can be calculated as[3]:

$$\boldsymbol{M} = \chi_d \boldsymbol{H} \tag{2.3}$$

where χ_p is the diamagnetic susceptibility. χ_d is negative and usually very small. [3]

Diamagnetism arises due to the change in orbital motion of electrons in an atom under an applied magnetic field and occurs in all atoms. The application of magnetic field generates currents in the atoms which according to Lenz's law oppose the applied field generating a magnetic moment opposing the field. This effect is so small however that it is only observable in materials with full outer shells such as the noble gases as their atoms have no net magnetic moment.[2]

2.3 - Paramagnetism

The magnetisation of a paramagnetic material aligns with an applied magnetic field and is proportional to the field, i.e[1]:

$$\boldsymbol{M} = \chi_p \boldsymbol{H} \tag{2.4}$$

where χ_p is the paramagnetic susceptibility. This is usually small, being on the order of 10^{-3} to 10^{-5}. Paramagnetism only occurs in materials with atoms which have a net magnetic moment and where the moments are weakly coupled to each other. In such materials thermal energy causes the moments to be randomly aligned resulting in no net magnetisation in the material without an applied field. When a field is applied a small fraction of the moments are deflected in the field direction resulting in a small magnetisation in the field direction.[2] Examples of paramagnetic materials include many transition metal salts which have highly localised f electrons in their outer shells which do not overlap with neighbouring atoms resulting in weak coupling of the magnetic moments.[2]

2.4 - Ferromagnetism

Ferromagnetic materials are substances that are paramagnetic at high temperatures but which when cooled below their Curie temperature (T_c) exhibit a non-linear response to magnetic field and much higher magnetisations than observed in either diamagnetic or paramagnetic materials. This magnetisation can also be retained under zero magnetic field. Below the Curie temperature the magnetisation in neighbouring atoms is aligned due to the Heisenberg exchange interaction described below resulting in large areas of uniform magnetisation known as domains.[1] The magnetisation in the domains will tend to align

with one of the crystallographic easy axes which arise due to magnetocrystalline anisotropy unless it is made energetically unfavourable to do so. In the area between domains, referred to as domain walls, the magnetisation rotates gradually from the magnetisation of one domain to the other. As temperature is increased up to the Curie temperature thermal agitation misorients the magnetic moments of the atoms in the material lowering its magnetisation until the Curie temperature is reached at which point spontaneous magnetisation vanishes.[1]

Comparisons of the responses of diamagnetic, paramagnetic and ferromagnetic materials to applied field are shown in Fig. 2.1. The maximum value of magnetisation for the material is the saturation magnetisation $\mathbf{M}_s$ and is reached once a high enough field is applied to orient all magnetic moments to the field direction.

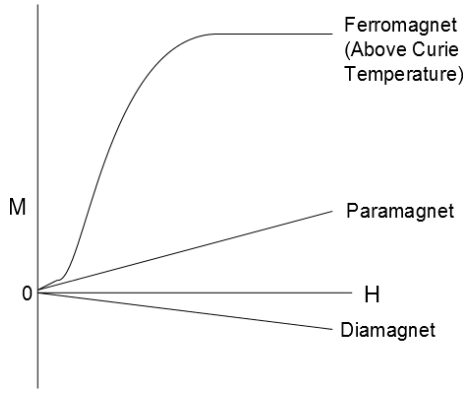

Fig.2.1 – Comparison of the magnetic response of diamagnetic, paramagnetic and ferromagnetic materials to an applied magnetic field.

Various magnetic energies contribute to the orientation of magnetic moments in a ferromagnetic material, as described below.

2.5 - Magnetostatic Energy

The magnetostatic energy E_M arises due to the opposition of the internal magnetic field (the demagnetising field) of a material to the magnetisation of the material. This demagnetising field arises as a direct result of the magnetisation in the material. The magnetostatic energy takes the form[1][3]:

$$E_M = \frac{1}{2}\mu_0 N \boldsymbol{M}^2 \tag{2.5}$$

where *N* is the demagnetising field tensor and is dependent on the shape of the sample giving rise to shape anisotropy. For example the magnetostatic energy of a thin film is low when the magnetisation lies in the plane of the film (i.e. $N \rightarrow 0$) and is high when the magnetisation is perpendicular to the film ($N \rightarrow 1$).[1] If the magnetisation is arranged into a 'flux closure' configuration so as to minimise stray fields the magnetostatic energy is minimised, an example of this is shown in Fig.2.2. Often materials with low magnetocrystalline anisotropy, such as permalloy (Ni80Fe20), have their magnetic structure dominated by the minimisation of magnetostatic energy and as such the magnetic structure will be highly shape dependent.

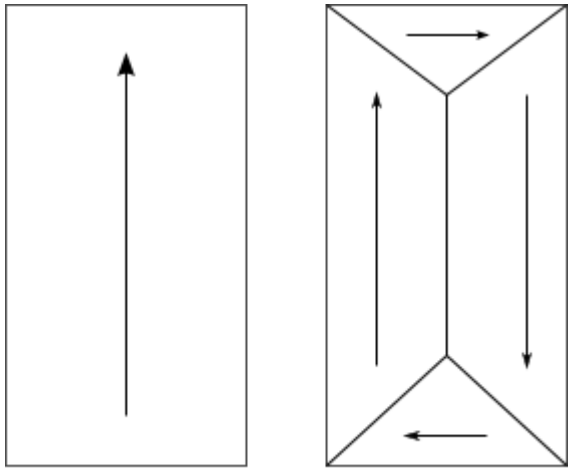

Fig.2.2 – a) A single domain magnetic configuration with high magnetostatic energy. b) A flux closed magnetic configuration with low magnetostatic energy. Arrows represent magnetisation direction.

2.6 - Magnetocrystalline Anisotropy Energy

The magnetocrystalline anisotropy energy E_K arises due to the crystal structure of a material and the spin-orbit interaction. The spins of electrons in a material are coupled to the orbits of the electrons. Since the orbits are coupled to the crystal lattice the spins will favour directions which allow the orbits to align with their low energy directions in the lattice.[1] Therefore this energy depends on the direction of the magnetisation with respect to the unit cell of the crystal and on the symmetry of the crystal unit cell itself. For example, for a cubic system E_K takes the form[1]:

$$E_{KC} = \boldsymbol{K}_1(\alpha_1{}^2\alpha_2{}^2 + \alpha_2{}^2\alpha_3{}^2 + \alpha_3{}^2\alpha_1{}^2) + \boldsymbol{K}_2\alpha_1{}^2\alpha_2{}^2\alpha_3{}^2 + \cdots \quad (2.6)$$

where α_1, α_2 and α_3 are the direction cosines of the magnetisation to the axes of the crystal unit cell. Usually the terms up to $\boldsymbol{K}_1$ are sufficient to represent the magnetocrystalline anisotropy energy with reasonable accuracy. The anisotropy energy of a uniaxial system takes the form:

$$E_{KU} = \boldsymbol{K}_U sin^2\theta_K \quad (2.7)$$

where θ_K is the angle between the uniaxial anisotropy $\boldsymbol{K}_U$ and the magnetisation direction. Magnetocrystalline anisotropy results in certain directions of magnetisation within the material being low energy or ‘easy’ directions and others being high energy or ‘hard’

directions.[2] Materials with high magnetocrystalline anisotropy, such as Nd-Fe-B magnets, have their magnetic structure dominated by magnetocrystalline anisotropy and their magnetisation will tend to align with the easy axis regardless of shape.

2.7 - Zeeman Energy

The Zeeman energy arises due to the alignment of a material's magnetisation to an external magnetic field (***H***). The Zeeman energy for a single magnetic moment takes the form:

$$E_Z = -\mu_0 \boldsymbol{m} \,.\, \boldsymbol{H} cos\theta \tag{2.8}$$

where θ is the angle between the magnetisation vector and the magnetic field vector. The total Zeeman energy of a material can be calculated by integrating with respect to the volume of the material. An increasing applied magnetic field will cause magnetisation in a ferromagnetic material to align to the field direction. This magnetisation switching is mediated by domain nucleation, magnetic domain wall motion and rotation of magnetic moments in domains.[2]

2.8 - Exchange Energy

The exchange energy is the energy resulting from the relative directions of adjacent atomic moments within a material and has quantum and magnetostatic components. For a pair of atoms, *a* and *b*, with spins $\boldsymbol{S_a}$ and $\boldsymbol{S_b}$ the exchange energy is[1]:

$$E_{ab} = -2J_{ab}\boldsymbol{S_a}.\boldsymbol{S_b} \tag{2.9}$$

where J_{ab} is the exchange integral of the material and the value of J_{ab} gives rise to the type of magnetic order in the material. A positive exchange integral results in ferromagnetism as the exchange energy is minimised when magnetic moments are aligned parallel to each other while a negative exchange integral results in antiferromagnetism as the exchange energy will be minimised when magnetic moments are antiparallel. As the main contribution to the exchange energy is quantum it is a very short range effect usually only affecting nearest neighbour atoms. [1]

2.9 - Magnetostrictive Energy

When a magnetic material is strained a magnetostrictive energy arises due to the effects of displacement of the atoms in the material. It arises from a change in the electronic interactions of neighbouring atoms and the resulting changes to the spin-orbit interaction.[2] Magnetostrictive energy thus has similarities to the magnetocrystalline anisotropy.

The magnetostrictive energy can be calculated for any combination of internal stresses (eg. from defects) and externally applied stresses as follows:

$$E_{\sigma} = -\frac{3}{2}\lambda_s\left\{\sum_{i=1}^{3}\sigma_{ii}{\gamma_i}^2 + \sum_{i\neq j}\sigma_{ij}\gamma_i\gamma_j\right\} \tag{2.10}$$

The simplest case of a uniaxially applied strain causes preferred directions in the magnetisation direction, i.e. an effective uniaxial anisotropy. The magnetostrictive energy E_{λ} takes the form:

$$E_{\lambda} = \boldsymbol{K_{eff}} sin^2\theta_{\lambda} \tag{2.11}$$

where K_{eff} is the effective anisotropy constant for the applied strain and θ_λ the angle between the magnetisation direction and the anisotropy direction. The value of K_{eff} can be found for a uniaxial strain as follows:

$$\boldsymbol{K_{eff}} = \frac{3\lambda_s \boldsymbol{\sigma}}{2} \tag{2.12}$$

or more usefully:

$$\boldsymbol{K_{eff}} = \frac{3\lambda_s \varepsilon E}{2} \tag{2.13}$$

where λ_s is the saturation magnetostriction, $\boldsymbol{\sigma}$ is the applied stress, ε is the applied strain and E is the Young's modulus of the material. λ_s is the maximum resultant magnetostrictive strain that results from obtaining uniform magnetisation by the application of a magnetic field. The magnetostrictive effect is a change in strain within a magnetic material due to the change is magnetisation in response to an applied magnetic field in order to minimise the magnetostrictive energy of the material. The inverse effect of applied strain changing the magnetic configuration and magnetisation of a material is known as the Villari effect [1] and is caused by strain-induced magnetic anisotropy. It can be seen from Eq. 2.13 that in applications where the aim is to use strain induced anisotropy it is desirable to use materials with high values of λ_s and E.

2.10 - Domains and Domain Walls

The magnetic system energy of a ferromagnetic material is often minimised by the formation of multiple uniformly magnetised regions called domains, for example the 'flux closure' state referred to in the discussion on magnetostatic energy [3]. An example of a high magnetostatic energy single domain and low magnetostatic energy flux closure state are shown in Fig.2.2.

Bloch showed that the boundary between domains is many atoms thick [3] as the energy associated with this region (referred to as the domain wall) is reduced when the magnetisation direction changes gradually across the wall. Fig.2.3 shows a Bloch wall between two domains with antiparallel domains.

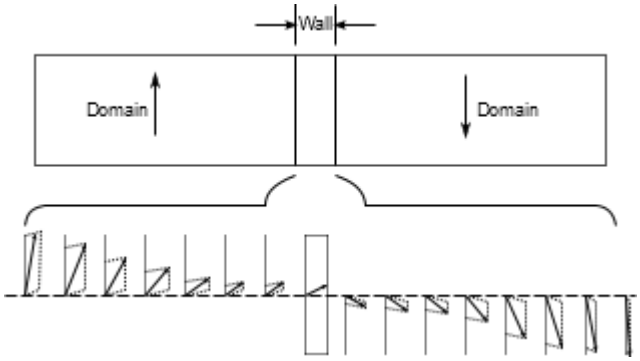

Fig.2.3 – Schematic of the progression of magnetic moments (shown by arrows) across a Bloch wall.

The exchange energy is minimised when the angle between neighbouring moments are small, i.e. for wide domain walls. The magnetocrystalline anisotropy, magnetostatic and strain anisotropy energies are minimised when moments remain aligned with an easy axis in the material, causing a preference for smaller domain walls. Therefore the width of a domain wall depends on the interaction of these energies as the exchange interaction favours very wide walls while the minimisation of anisotropy energy favours very narrow walls.[3]

2.11 - Magnetisation Reversal and Hysteresis

When a ferromagnetic material is subjected to a magnetic field domains with magnetisation direction close to the field direction begin to grow at the expense of other

domains. The growth of the domains occurs by movement of the domain walls in the material. The higher the field the more these domains will grow until the other domains are annihilated leaving a single domain. When the magnetisation is saturated the magnetisation will be aligned with the field direction even if this is not in one of the easy axis directions. If the field is removed the dipoles will once again align with the easy axis.[2] The movement of domain walls required for magnetic reversal is mediated by pinning of the domain walls in the material at defects such as grain boundaries and dislocations which pin the domain walls magnetostatically. The field must be high enough to overcome the magnetostatic energy of the pinned domain wall for the magnetic reversal to continue. When the field is removed the demagnetising field of the material will act to partially reverse the material in the opposite direction, however as the demagnetising field will be much smaller than the saturation field the magnetostatic interaction of the domain walls with the defects will be sufficient to prevent full reversal of the material resulting in a remanent magnetisation. Applying an external field in the opposite direction repeats the same process switching the magnetisation of the sample to lie in the opposite direction.[2]

2.12 - References

[1] De Lacheisserie, E.T, 1993, Magnetostriction Theory and Applications, CRC Press

[2] Spaldin N., 2003, Magnetic Materials Fundamentals and Applications, Cambridge university Press

[3] Bozorth, R.M, 1993, Ferromagnetism, IEEE Press, New York

3 - Literature Review

This chapter contains a review of literature relevant to magnetic memory and devices based on the control of magnetic properties by applied strain.

3.1 - Magnetic Nanowires

As the dimensions of magnetic elements are reduced to the nanoscale the domain structures become limited by the geometry of the element due to the relatively high energy associated with magnetic domains and domain walls in such small volumes. One geometry that has received much interest is the nanowire geometry where long (up to several micrometres) elements are formed with low widths and thicknesses. The strong shape anisotropy associated with such a geometry provides a strong easy axis along the length of the wire if magnetocrystalline anisotropy is low. Of particular interest has been the ability of this geometry to contain domain walls which can then be moved within the wire using an electric current[1] or a magnetic field[2]. Domain walls in wires offer opportunities for logic[3], memory[4][5] and sensing devices[6], however realising such devices relies on the ability to control domain walls in wires.

Domain walls in nanowires are usually referred to as either head-to-head or tail-to-tail in order to differentiate between walls which have the magnetisation in the opposing domain oriented towards each other (head-to-head) or away from each other (tail-to-tail). Furthermore, the domain wall can be either a transverse wall with a continuous rotation of moments between domains and a characteristic V shape (see Fig.3.1[7]) or a vortex wall where a full vortex exists between the two domains (see Fig.3.2[7]). Asymmetric transverse walls can also exist within a narrow range of wire dimensions (see Fig.3.3[7]) but will not be

considered here. Nakatani et al. calculated a phase diagram for the three domain wall types in nanowires with varying width and thickness.[7] The final property of the wall to consider is its chirality. In the case of the transverse wall this refers to whether the magnetisation direction at the centre of the wall is oriented up or down. For vortex walls the chirality refers to whether the vortex is clockwise or anticlockwise.

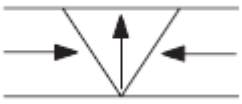

Fig.3.1 – Transverse domain wall.[7]

Fig.3.2 – Vortex domain wall.[7]

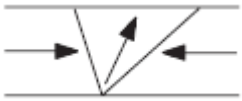

Fig.3.3 – Asymmetric transverse domain wall.[7]

The first requirement in using such structures is the ability to controllably introduce a domain wall into the nanowire. This is most easily achieved using a domain wall 'nucleation pad' of a larger patterned region at one end of a magnetic nanowire[8]. Casey et al. showed that in elements consisting of wide and a narrow wire sections (see Fig.3.4 [9]) the magnetisation reversal of the entire element is controlled by the wider section allowing the narrower section to switch at a lower field than a single wire of the same narrow width.[9] This reduced switching field is the basis for the nucleation pads used in geometries using nanowires. A wide section is used as it can switch easily and 'inject' a domain wall into the narrower nanowire section. Casey et al. confirmed the dominant role of wire width in the switching of wire elements (see Fig.3.5 [10]) and showed that in elements where nucleation

of the reverse domain switches the wire length and volume of the wire have little effect on the switching field. This is because the domain nucleation only occurs in a small activation area of the wire. Casey et al. later showed that because of this wires made from very thin films become superparamagnetic even at room temperature.[11]

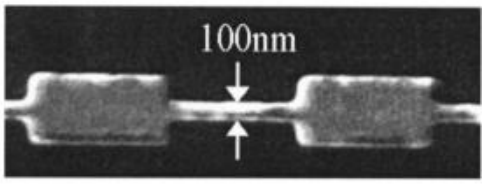

Fig.3.4 – Image of structures used in experiment by Casey et al.[11]

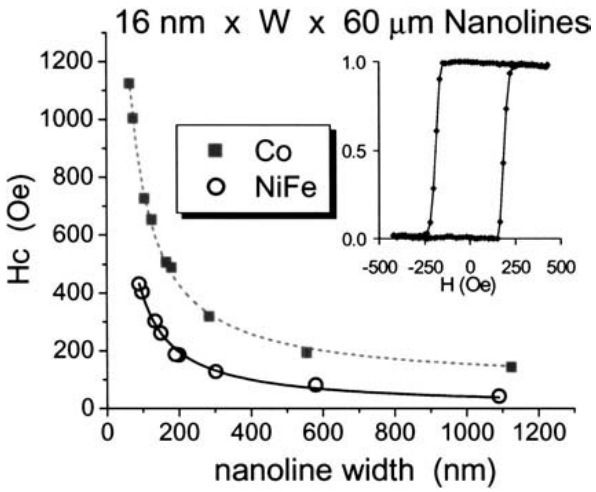

Fig.3.5 – Plot showing switching field of nanolines with varying width.[11]

The most common methods used to control domain walls in a nanowire are constrictions or protrusions in the wire. These are used to 'pin' domain walls by providing energy wells or barriers which halt a domain wall's propagation through its wire. Faulkner et al. used an L shaped geometry (see Fig.3.6 [12]) consisting of an injection pad, a smooth corner and a wire with a triangular notch. The purpose of the L geometry is to separate the field required to inject the domain wall and the field required for it to propagate through the notch, thus allowing small notches with propagation fields potentially lower than the injection field to

be examined. The data from this experiment (see Fig.3.7 [12]) show that the depinning field of a domain wall from the notch increases with notch depth.[12]

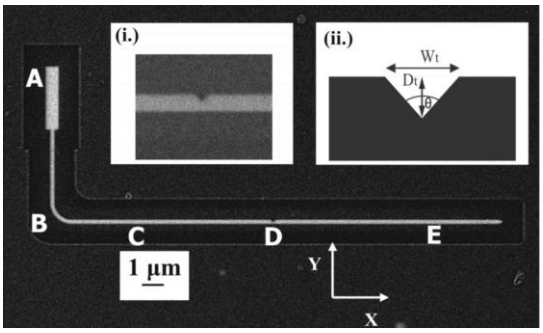

Fig.3.6 – Image of structures used in experiment by Faulkner et al. Site A is injection pad used to introduce domain walls into the structure. D is notch used to pin domain walls.[12]

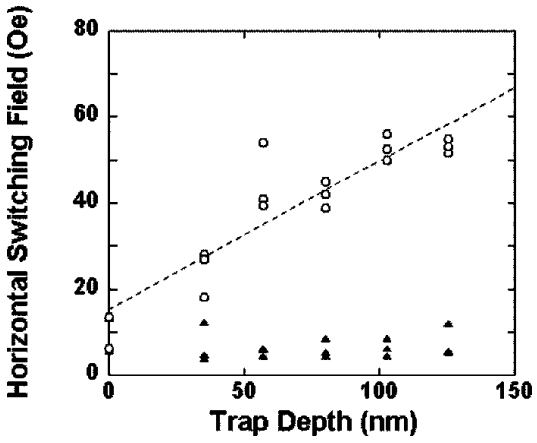

Fig.3.7 – Switching fields for sites C (black triangles) and E (white circles). The switching fields represented by the white circles represent the depinning fields of domain walls from the notch.[12]

Allwood et al. performed an experiment using domain wall 'diodes' [13]. The experiment investigated domain wall depinning from a trap consisting of a triangle with wires out of its apex and base (see Fig.3.8 [13]).[13] This kind of trap is symmetric with a line of symmetry along the wire length and therefore domain walls of opposite chirality will behave identically, in order to avoid confusion traps with this property will be referred to here as

'symmetric'. Traps with a line of symmetry perpendicular to the wire will simply be described as notches or traps and those without a line of symmetry perpendicular to the wire will be referred to as 'diodes'. Therefore using this convention the diodes used in this experiment were symmetric. The propagation of a domain wall through the apex of the diode and out through the base was found to be governed by a series of weak pinning sites provided by defects such as edge roughness. It was shown that due to the more abrupt expansion of the domain wall required to propagate it through the base of the diode's triangle, requiring a large increase in the domain wall energy, a significantly higher field was required to propagate the domain wall through this single large energy barrier. Because of this difference in the required field a domain diode can be used to allow domain wall propagation in only one direction through a wire.[13]

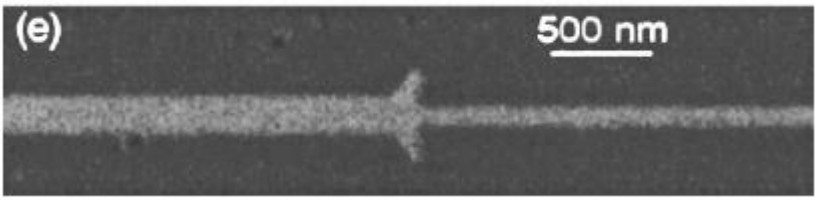

Fig.3.8 – Image of a domain wall diode structure as investigated by Allwood et al.[13]

Lendecke et al. showed that the depinning field from a triangular notch decreased with increased temperature from 5K to 50K.[14] This temperature dependence was modelled using the Kurkijärvi model to represent the domain wall hopping over a single energy barrier. The energy barrier heights obtained using this model were significantly higher than the thermal energy of the system at room temperature showing that the applied field is the primary driver for depinning. [14]

Petit et al. were able to investigate the energy landscape experienced by transverse domain walls encountering T-shaped traps (see Fig.3.9 [15]) consisting of a branch perpendicular to

a nanowire. As this is an asymmetric trap design they were able to vary domain wall chirality and magnetisation direction to access four different energy landscapes in the arm of the trap (see Fig.3.10 [15]). Using a technique wherein the domain wall is propagated into the trap using a magnetic field followed by application of a reverse field the energy landscape of the trap can be probed. The results show that traps can become of energy barrier, energy wells or a barrier with energy wells on either side, depending on the precise magnetic configuration of the domain wall and surrounding domains (see Fig.3.11 [15]).

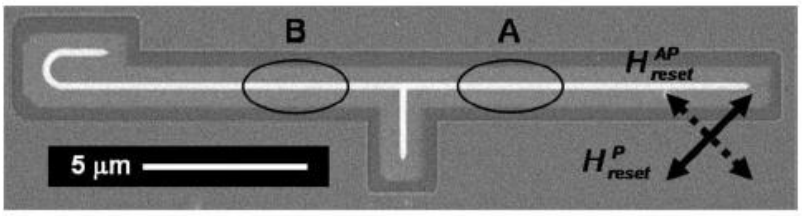

Fig.3.9 – Image of the T shaped domain wall trap structure investigated by Petit et al.[15]

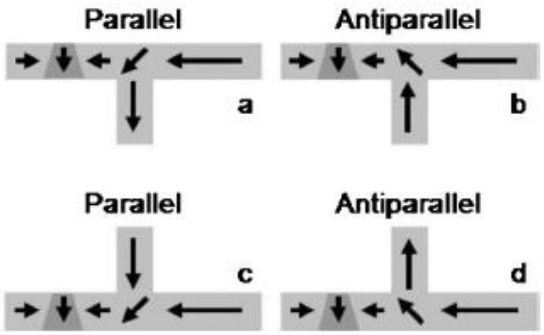

Fig.3.10 – Schematics of the four possible domain wall – trap interactions in the experiment by Petit et al. The four configurations depend on the magnetisation direction in the trap and the domain wall chirality with respect to the trap.[15]

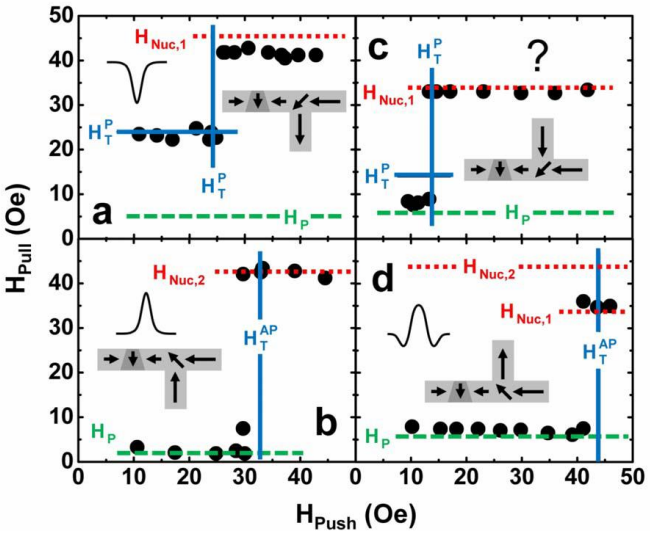

Fig.3.11 – Energy landscapes of the four possible interactions of a transverse domain wall in a nanowire with a T-junction showing (a) potential well, (b) energy barrier, (c) inconclusive results and (d) energy barrier with energy wells either side..[15]

Petit et al. later applied the same technique to study notches and also traps consisting of smaller perpendicular protrusions than their previous experiment [16]. The shorter protrusion simplifies the experiment somewhat as the magnetisation in this type of trap does not have the two possible directions as in the previous experiment and instead follows the edges of the protrusion due to shape anisotropy (see Fig.3.12 [16]). Similarly the magnetisation at a notch follow the shape of the notch (see Fig.3.13 [16]). The energy landscapes found for these two notch types are shown in Fig.3.14 [16] for the two possible chiralities of a transverse domain wall. These results show that a notch too can act as an energy well or barrier and that chirality is an important factor in the depinning field at an asymmetric domain wall.

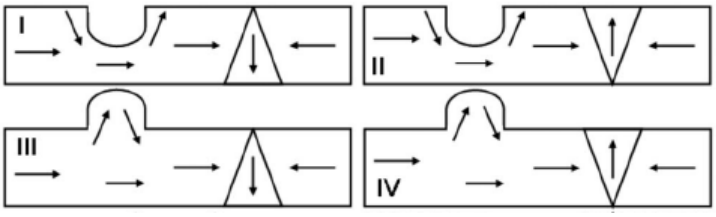

Fig.3.12 and 3.33 – Schematics of the magnetisation at protrusion and notch type traps and the possible chiralities of interacting domain walls.[16]

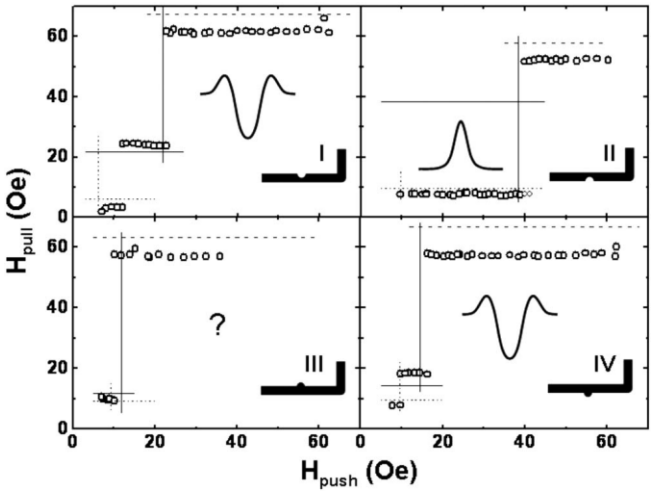

Fig.3.14 – Energy landscapes for the four possible interactions as defined by the notch/protrusion and domain wall chirality combinations in Fig.3.13.[16]

Bogart et al. studied domain wall pinning using asymmetrical notches of different shape in order to study the effects of domain wall chirality and notch shape on pinning strength. Both triangular and rectangular notches were studied as shown in Fig.3.15 [17]. The rectangular notch was found to be a more effective pinning site. However it was observed that the wire width has a greater influence on the depinning field than the shape of the notch. It was also observed that while the notch depth increases the depinning field significantly this effect reaches a plateau at around 60% of the wire width. It was also shown that the chirality of the domain wall influenced the depinning field; micromagnetic

simulations suggested that transverse walls with moments pointing towards the notch were the more strongly pinned chirality.[17]

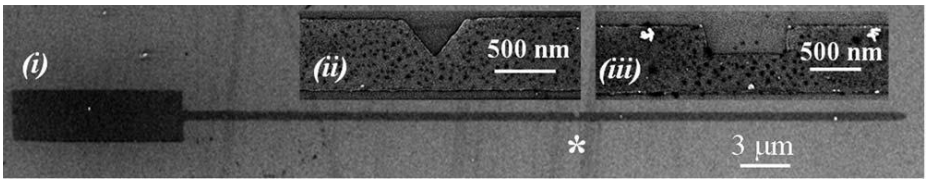

Fig.3.15 – Images of notch types and wire/pad structure used in experiment by Bogart et al.[17]

Im et al. studied the stochastic nature of domain wall depinning from notches using magnetic transmission soft x-ray microscopy [18]. They observed that the depinning field varies during repeated cycles in the same structure. The distribution of depinning field varies with wire width and notch depth. As a measure of the spread of depinning fields the standard deviation of the depinning field was plotted against these two dimensions of the wire (see Fig.3.16 [18]). Im et al. attribute the stochastic nature of depinning to variations in the domain wall structure at the notch and suggest that thermal effects are not the major cause. The evidence for this claim is the non-Gaussian distributions they observed. Therefore it is suggested that limiting the number of domain wall structures that can be generated at a notch or presented to a notch will make the depinning field more reproducible.[18]

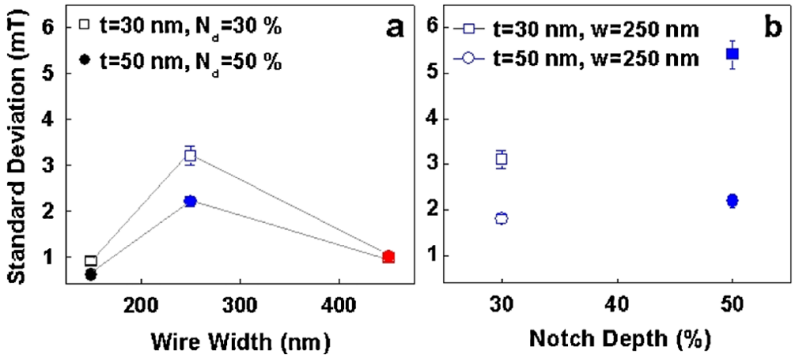

Fig.3.16. – Spread of the depinning fields of domain walls from a notch with (a) varying wire width and (b) varying notch depth(N_d), (as % of wire width). The spread is measured as standard deviation.[18]

Akerman et al. also studied the stochastic nature of domain wall depinning [19]. This study included a variety of symmetrical notches (square, triangular, square left, square right, elliptical and circular). Symmetrical notches were chosen in order to eliminate the effect of domain wall chirality. They used anisotropic magnetoresistance (AMR) measurements in order to detect even very small changes in the domain wall profile. Fig.3.17 [19] shows the probability of domain wall pinning at these notches and the standard deviation of the depinning field. Stochastic variations in depinning were observed for all notch types. It was concluded that square notches offer the highest probability of pinning and a low standard deviation. The AMR showed that even for very small differences in the domain wall profile a change in depinning field was observed. [19]

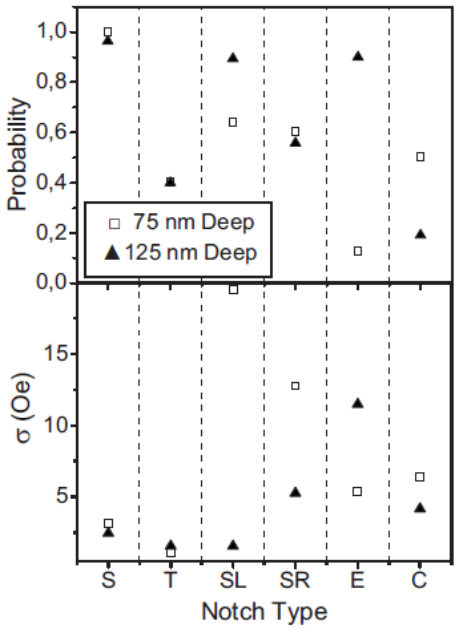

Fig.3.17 – Pinning probability and spread of depinning fields for different notch shapes. S-square, T-triangular, SL-square left, SR-square right, E-elliptical and C-circular.[19]

When propagating a domain wall through a wire the domain wall velocity increases proportionally to the applied field up to a field referred to as the Walker breakdown field (H_w)[20]. Above this field the domain wall structure fluctuates and periodically reverses its movement direction lowering its overall velocity in the direction of the magnetic field [32][21]. This effect is likely to lower the speed of domain wall based devices and reduce reliability due to changes in domain wall structure.

Possible methods of suppressing Walker breakdown include application of a transverse magnetic field[22] use of underlayers[23] and the use of in plane uniaxial anisotropy[24]. Simulations by Dean et al. showed that the effect of anisotropy should be strongest when the anisotropy is applied perpendicular to the nanowire. It was suggested that the superposition of anisotropies can be treated as a change in the effective dimensions of the wire with wire behaving as it would if it were thinner and wider.[24]

From these sources it can be seen how domain walls can be introduced into nanowires, propagated through the wire and pinned in specific sites.

3.2 - Magnetic Nanorings

This section will review the literature regarding symmetric circular rings. There is also a limited discussion of the behaviour of nanodiscs as they can be seen as the limit of circular rings where the diameter of the hole is equal to zero.

Thanks to its very high symmetry the nanoscale circular ring geometry (from here on referred to as the ring geometry) offers a uniquely balanced environment for studying magnetic behaviour [25]. Five remanent states of the ring geometry have been identified. The first of these is the 'vortex' state in which the moments in the ring align to the circumference producing a zero stray field state (see Fig.3.18 [26]). The vortex state in a ring is similar to the vortex state in nanoscale disks with the exception that the hole in the centre of the ring removes the need for a high exchange energy vortex core in the centre of the vortex as is seen in disks (see Fig.3.18 [26]). The vortex state has received interest as a potential unit of storage in M-RAM[27] due to the stability of the state and the two possible configurations (clockwise/anticlockwise vortex).

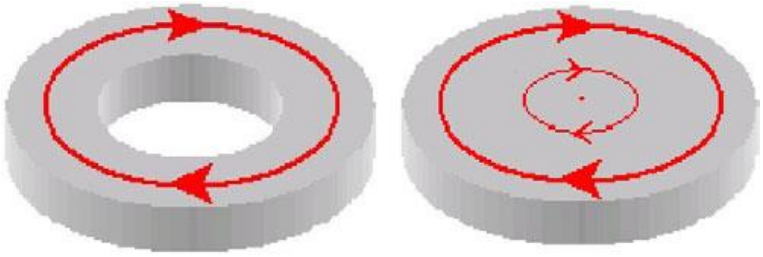

Fig.3.18 – Schematics of vortex magnetisation in a ring (left) and a disk (right). Arrows represent magnetisation direction. Note the out of plane vortex core in the centre of the disk.[26]

The second remanent state is the 'onion' state, so called as the two domains of this state resemble the two sides of an onion sliced lengthwise (see Fig.3.19 [26]). The onion state consists of two domains, one clockwise and one anticlockwise, with a pair of domain walls on opposite sides of the ring[28].

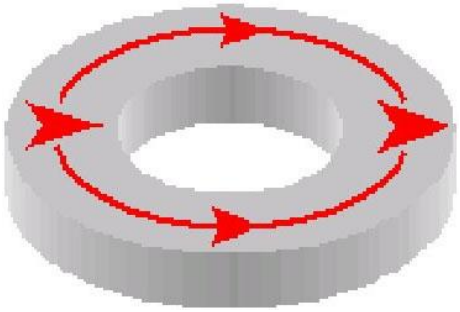

Fig.3.19 – Schematic of a magnetic onion state in a soft magnetic ring.[26]

The third remanent state is the twisted state in which a localised 360° domain wall is present in the ring. This state is metastable with respect to the vortex state. [29] The twisted state has also been proposed for use in M-RAM [29] but nonetheless has received much less interest than the vortex and onion state. The fourth state is the vortex core state where single vortex wall is present in the ring [30]. The fifth state is the vertical onion state

which can occur in very thick rings and consists of two domain walls which are oriented out of the plane of the ring [31].

In order to utilise the ring geometry an understanding of the effects of the ring dimensions is required. The three dimensions of interest are the ring width (*w*) the ring outer diameter (d) and the film thickness (*t*), shown schematically in Fig.3.20. The effect of some material properties will however be briefly mentioned.

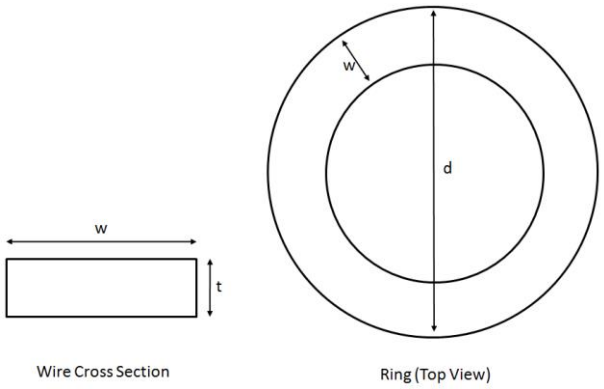

Fig.3.20 – Schematic of a ring structure showing the defining dimensions of a ring. Width (w), diameter (d) and thickness (t).

The dimensions of a ring affect the stability of the magnetisation states due to the competing magnetostatic and exchange energies [28]. The behaviour of rings has mostly been studied in the context of the switching between states. Y.G.Yoo et al. studied arrays of Co rings with varying *w*, *d* and *t* in order to construct a switching phase diagram (Fig.3.22) [28]. They identified two types of switching which they refer to as single and double switching. Single switching refers to a transition from one onion state directly into an onion state oriented in the opposite direction (which shall be referred to as the reverse onion state). Single switching can be a nucleation free process where the domain walls of the onion state move around the ring to align with the applied field or a process in which a reverse domain nucleates and switches the ring. Double switching refers to a process in

which the onion state switches first to a vortex state then to the reverse onion state. The onion to vortex transition occurs when one of the domain walls depins and annihilates the other and is only possible due to imperfections such as edge roughness acting as local pinning sites on the domain walls; a perfect ring would only exhibit single switching as both domain walls would move at the same field. An example hysteresis loop showing a double switching event is shown in Fig.3.21 [28]. It was found that *t* had the greatest effect on the switching behaviour with thinner rings exhibiting single switching due to the reduced stability of the vortex state as the exchange energy is dominant. A smaller effect is seen for increased *w* where spins align less strongly to the ring allowing a reverse domain to nucleate more easily and thus allowing single switching before domain wall depinning can occur. Similarly reducing *D* allows easier nucleation of a reverse domain making single switching more likely. These trends are shown in Fig.3.22[47]

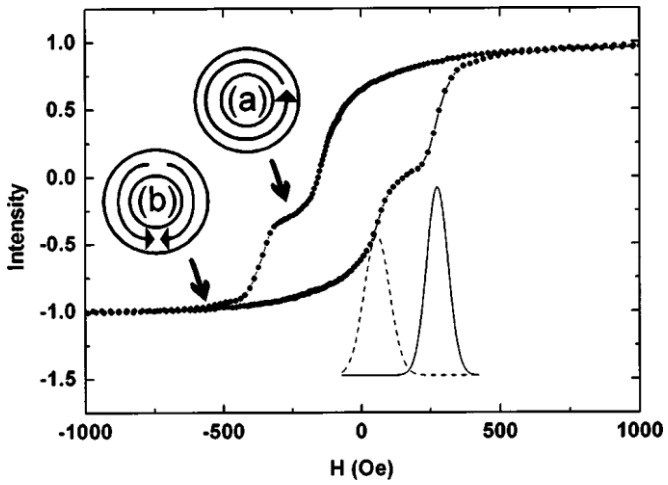

Fig.3.21 – Hysteresis loop for double switching in a ring showing double stepped loop and indicating magnetic structure of the ring in each section of the loop.[28]

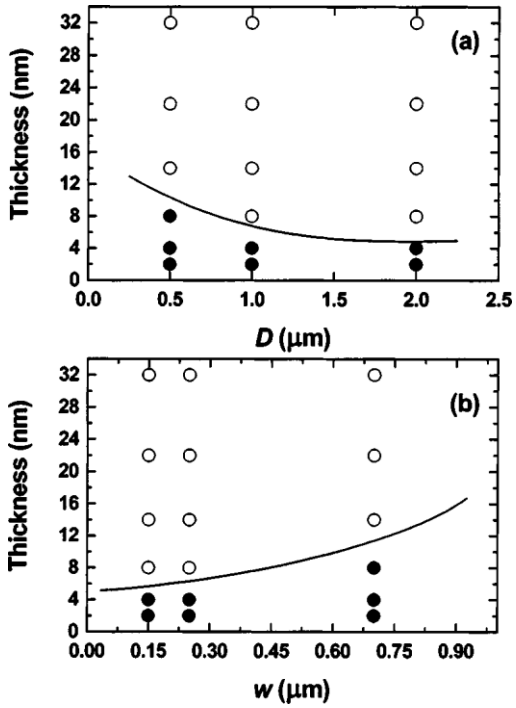

Fig.3.22 – Phase diagrams showing switching regime with varying t, diameter (D) and w. Open circles indicate double switching and closed circles indicate single switching.[28]

Castaño et al. studied the twisted state in Co rings with D from 160nm-520nm. The rings were cycled from onion to reverse onion state and observed using magnetic force microscopy (MFM). In each ring the onion state switched sequentially to the twisted state, the vortex state and finally to the reverse onion state. Each of these states was available at remanence with appropriate field cycling. The twisted state is metastable and transition to the vortex state occurs by decomposition of the 360° domain wall.[29] Structures where a stable vortex state is present during switching are described as having triple switching.[30] The stability of the vortex state decreases with increasing D and w leading to a smaller stability range or even suppression of the vortex state. Castaño et al. advise that as transitions in rings are controlled by domain movement, creation and annihilation, defects in the ring have a large effect on the switching behaviour. [29]

Klaüi et al. studied Ni-Fe and Co rings in order to construct a phase diagram of the single, double and triple switching mechanisms for different ring geometries. They concluded that the thickness of the ring is the main factor affecting the switching behaviour with thin rings showing single switching. They observed that triple switching only occurs in rings with a width large enough to accommodate the vortex core. In rings with a large diameter triple switching is suppressed due to the difficulty nucleating a vortex caused by the low curvature around the circumference which reduces the twisting of the spins. Therefore, when D is high double switching occurs. A phase diagram showing the ranges for these switching types is shown in Fig.3.23 [30].

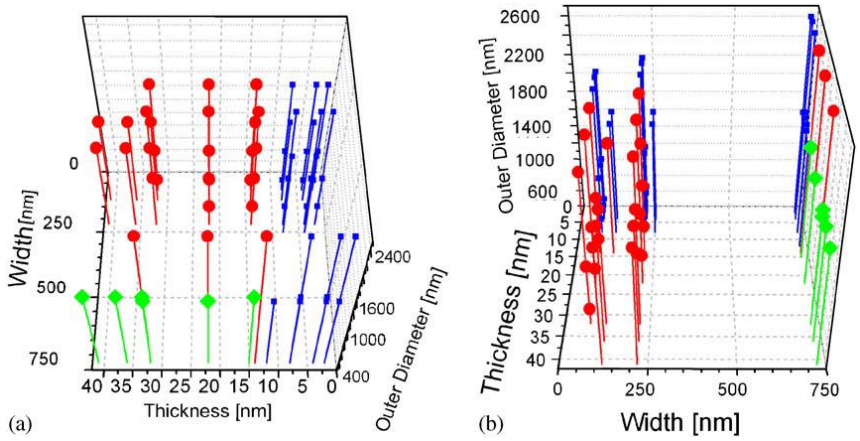

Fig.3.23 – Switching phase diagrams showing switching mechanism for rings of various dimensions. Blue(square) - single switching, red(circle) – double switching, green(diamond) – triple switching.[30]

It has also been observed that as D is increased the separation of the switching fields from onion to vortex and vortex to reverse onion is increased making it easier to access the desired state reliably [30]. It is thus possible to engineer rings in which the onion/reverse onion state is easily obtainable at remanence.

Zhang et al used Monte Carlo simulations in order to construct a comprehensive phase diagram of the switching processes in rings (Fig.3.24 [31]). The wider range of thicknesses than used in previous studies allowed them to identify the vertical onion state. As had been observed in previous studies the height is the most important dimension in determining the switching behaviour. Zhang et al. showed that it is specifically the height of the ring compared to the exchange length of the material which is important.[31]

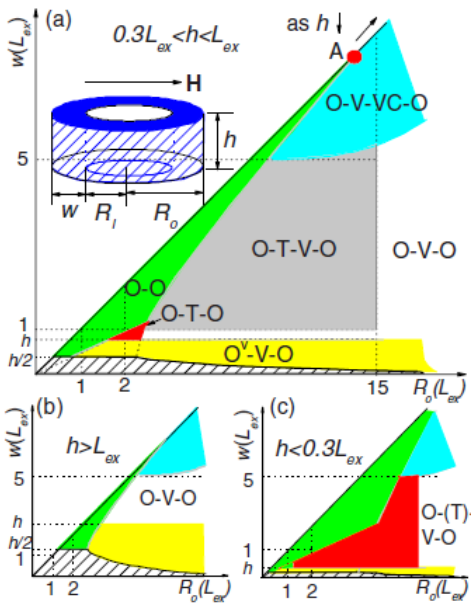

Fig.3.24 - Switching phase diagrams by Zhang et al. Choice of diagram is determined by the height of the ring (h) compared to the exchange length of the material (L_{ex}). The switching regimens are described by the structures present during switching. O – onion, V – vortex, VC – vortex core, T – twisted, O^V – vertical onion. a,b and c show data for three thickness conditions.[31]

The behaviour of circular nanomagnets can be seen as a special case of ring structures where the diameter is twice the width of the ring. Soft magnetic disks with sufficiently large dimensions have a preference to form a vortex magnetic configuration. If a field is applied in plane the vortex core is pushed out of the disc and it is saturated in plane. If the disc is small enough the magnetostatic energy of the vortex core will become unfavourable and

the disc be magnetised as a single domain oriented in the plane of the film. Such structures have been proposed for use as they simulate a single 'giant spin'. Cowburn et al. found experimentally the phase diagram for the vortex state and single domain sate in small (sub-micrometre) discs (see Fig.3.25 [32]). The single domain state is stabilised at lower thicknesses and diameters [32].

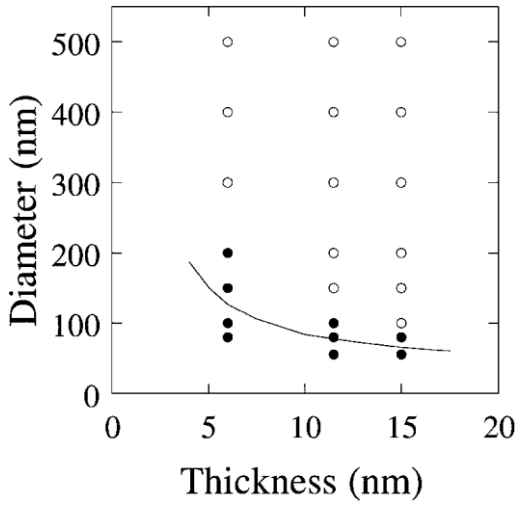

Fig.3.25 – Phase diagram for circular nanomagnets. Open circles represent multidomain states; filled circles represent stable single domain states.[32]

From these works the behaviour of specific ring geometries can be predicted such that the desired remanent states should be accessible. The switching processes in any ring geometry should also be predictable if desired.

3.3 - Multiferroics

Multiferroic materials are materials which exhibit two or more of the ferroic properties of ferroelectricity, ferroelasticity and ferromagnetism[33]. Coupling these properties in principle will create powerful multifunctionality. The most common type of multiferroics are materials with combined ferroelectricity and ferromagnetism, the combination of these

two properties is often referred to as the magnetoelectric (ME) effect. In such a material application of a magnetic field induces an electric polarisation (direct ME effect) and conversely application of an electric field will induce a magnetisation in the sample (converse ME effect). The first multiferroic material, nickel-iodine boracite, was discovered by Ascher et al [34]. A range of other multiferroic materials have been discovered since (e.g. $LiCoPO_4$[33], yttrium iron garnet[33], $TbPO_4$[33]), however none of the single phase multiferroics yet discovered has a strong ME effect[33].

In order to produce multiferroic materials with a strong ME effect, composites have been produced which combine highly piezoelectric materials with highly magnetostrictive materials [35]. By mechanically coupling these materials the ME effect can be induced in the composite. In the direct ME effect application of the magnetic field deforms the magnetostrictive material, which duly deforms the piezoelectric material it is coupled to, inducing an electric polarisation. In the converse ME effect application of an electric field deforms the piezoelectric material, due to the mechanical coupling the magnetostrictive material is strained inducing magnetisation. Examples of these 'artificial' multiferroic composites include PZT/Ni-ferrite particulate composites[35], laminar composites of PZT with magnetic oxides [35] and bilayer/sandwich composites of PZT and Terfenol-D [35].

ME materials, whether composite or single phase, can be described by an ME coupling coefficient (α) which relates electric polarisation (P) and magnetic field (H) as [35]:

$$\frac{\partial P}{\partial H} = \alpha \tag{3.1}$$

In composite multiferroics α can be calculated as [35]:

$$\alpha = k_c e_m e \tag{3.2}$$

Where e_m is the piezomagnetic coefficient of the magnetic phase, e is the piezoelectric coefficient of the piezoelectric phase and k_c is a coupling factor between zero and one. The coupling factor represents the strength of the mechanical coupling between the two phases [35]. Clearly the development of a multiferroic composite with high α requires all three of these component values to be as high as possible.

Common materials chosen because of their high piezoelectric coefficient include lead zircanate titanate (PZT)[35], lead manganese titanate-lead niobate (PMN-PT)[35], barium titanate[35] and polyvinylidene fluoride (PVDF)[35]. Materials chosen for their high magnetostriction include Galfenol ($Fe_{1-x}Ga_x$)[35], Terfenol-D ($Tb_{1-x}Dy_xFe_2$)[35] and Metglas®[35].

Multiferroic composites are commonly categorised by the connectivity of their constituent materials, for example, particulate type, laminate type and fibre/rod type (Fig.3.26) [35].

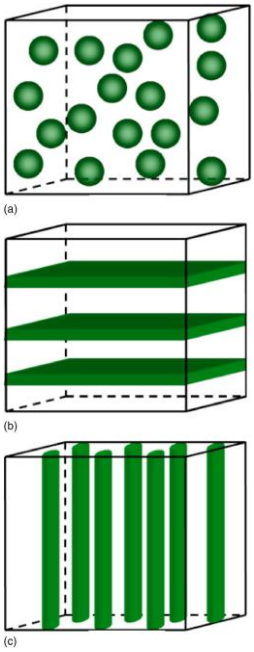

Fig.3.26 – Examples of multiferroic composite connectivities. From top to bottom: 0-3 (particulate type), 2-2 (laminate type), 1-3 (fibre/rod type).[35]

It has also been observed that the magnetoelectric effects of composites are greatly enhanced if the material is subjected to an alternating magnetic or electric field with a frequency at or near to the resonance of the piezomagnetic or piezoelectric material respectively. Fig.3.3. A shows an example of the response of a $CoFe_2O_4$/PZT bilayer to alternating electric field at varying frequencies with a peak in the value of α at the resonance frequency of 350 kHz.[35]

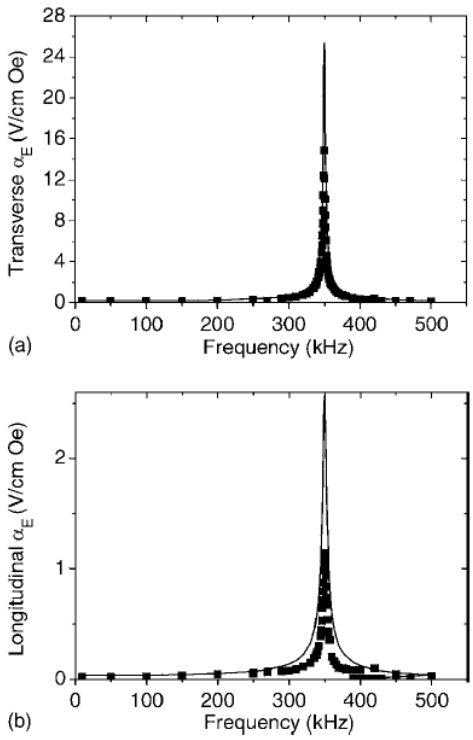

Fig.3.27 - Respone of a $CoFe_2O_4$/PZT bilayer to alternating electric field at varying frequencies.[35]

While it is common for multiferroics literature to refer to an electric field induced magnetisation, it is more correct to describe how the strain transferred to the magnetostrictive component induces uniaxial magnetic anisotropy. This induced anisotropy can be used to control the behaviour of the magnetic component in various ways, including rotation of magnetic domains to create an overall magnetisation. The strain induced uniaxial anisotropy generated by a uniaxial strain in an elastically isotropic material can be calculated as shown in Eqn.2.11.

Zavaliche et al. described the use of an electric field induced magnetic anisotropy in a hybrid multiferroic nanostructure [36] of magnetostrictive $CoFe_2O_3$ pillars embedded in a ferroelectric $BiFeO_3$ matrix. The pillars displayed a strong out of plane anisotropy and required large fields of around 10 kOe to switch completely between the two out of plane

magnetisation directions. The stress induced by the ferroelectric matrix under an applied electric field induced an in plane magnetic anisotropy in the pillars allowing the moments to rotate in plane more easily and thus lowering the field required to switch the pillars between states with a voltage of -16V allowing 60% of the pillar's volume to switch at a field of 580 Oe.[36]

Chung et al. studied Ni nanobar structures on lead zirconate titanate (PZT).[37] Using MFM to observe the domain structure in the nanobars they applied an electric field to the sample in order to apply stress to the nanobars. The induced anisotropy altered the domain structures to transitional S-shaped structures which reverted back to the original domain structure when the electric field was removed (see Fig.3.28 [37]).[37] Later work by Chung et al. [38] again using Ni nanobars on PZT substrates found that transitional domain structures obtained under applied electric fields were very similar to those observed under small applied magnetic fields (Fig.3.29).

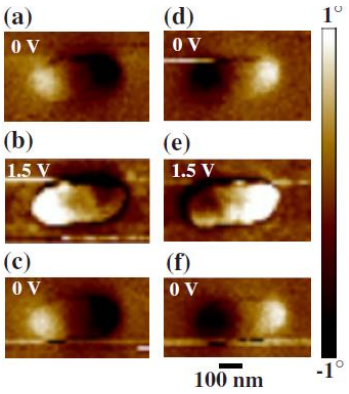

Fig.3.28 – Magnetic force microscopy images of domain changes in nanobars with application of voltage (stress). Images (a)-(c) show the reversible process for domain structures oriented one way along the nanobar easy axis and (d)-(f) for domain structures oriented the other way (from [37]).

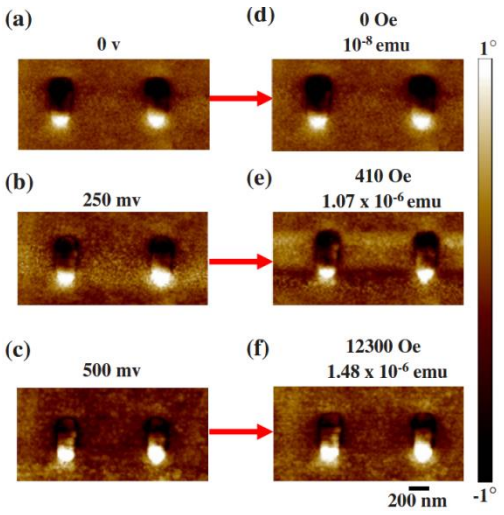

Fig.3.29 – Magnetic force microscopy images of domain structure changes (a)-(c) due to stress compared to changes induced by (d)-(f) applied magnetic field (from [38]).

Weiler et al. deposited polycrystalline evaporated Ni films onto PZT actuators [39]. They showed that the in plane easy axis of the film could be rotated by 90° by the application of strain from the piezoelectric actuator. This result showed that the stress induced anisotropy was strong enough to overcome all other contributions to the in plane anisotropy.[39]

Brintlinger et al. studied a Galfenol ($Fe_{70}Ga_{30}$) thin film deposited onto a $BaTiO_3$ film.[40] They calculated that with an applied voltage a uniaxial magnetic anisotropy of 25 kJ/m^3 could be applied to the Galfenol film. They used Lorenz microscopy to directly observe the effect of the applied anisotropy on the magnetic domain structure of the Galfenol film and were able to observe the reversible movement of domain walls as the applied voltage was increased. [12]

Brivio et al. measured the magnetic properties of Fe deposited by molecular beam epitaxy onto $BaTiO_3$ with varying applied electric field [41]. They observed that the coercivity of the Fe film could be changed significantly when an electric field was applied (Fig.3. 3.8). The

magnitude of the change in coercivity is dependent on the temperature at which the measurement is taken as the $BaTiO_3$ film changes phase from orthorhombic to tetragonal at 290K. The orthorhombic form (measured at 250K) exhibited a greater influence on the (magnetic) coercivity of Fe, with it more than halving in value for one polarity of voltage (see Fig.3.30 [41]). They also demonstrated that an applied positive voltage induced an increase in the out of plane uniaxial anisotropy.[41]

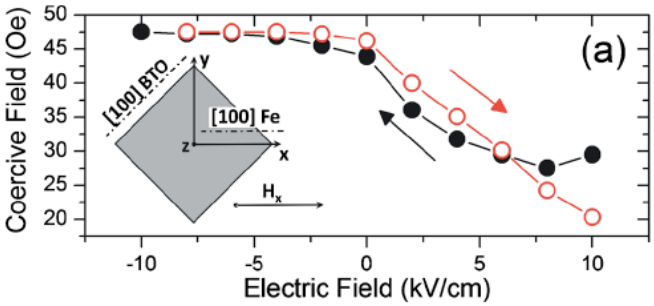

Fig.3.30 – Data showing the reduction in coercivity with application of positive electric fields to Fe on [100] $BaTiO_3$ (from [41]).

Hockel et al. patterned Ni rings with an outer diameter of 2µm, inner diameter of 1.4µm and thickness of 35nm onto single crystal PMN-PT [42]. By applying a voltage to the PMN-PT substrate they were able to strain the rings inducing a uniaxial anisotropy. The rings were initialised to the onion state and the domain structure observed using magnetic force microscopy. It was observed that the induced anisotropy caused the domain walls in the ring to rotate and align approximately with the induced anisotropy (see Fig.3.31 [42]). This rotation of the domain walls was permanent with removal of the applied electric field.[14]

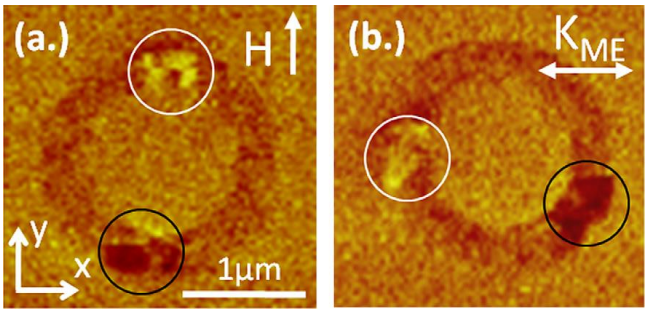

Fig.3.31 – MFM images showing behaviour of Ni rings on PMN-PT. Image (a) shows the initialised onion state with domain walls highlighted. Image (b) shows the new orientation of the same domain wall on application of uniaxial anisotropy $K_{ME}=K_u$.[42]

3.4 - Magnetic Memory

Magnetic data storage is already used extensively in hard disc drives (HDDs) but remains rare in random access memory (RAM) [43] which still overwhelmingly uses semiconductor technology. It has been suggested that magnetic technologies could be more energy efficient and non-volatile than ferroelectric based RAM [5]. What follows is a review of some proposed dynamic magnetic memory concepts and their extension to magnetic domain wall logic concepts.

Atkinson et al. suggested the use of deliberately notched wires as a magnetic random access memory (MRAM) storage elements.[4] By using a wire with two notches, one on either side of the wire, this proposed memory cell offers multibit storage as there are more than two possible states available depending on the position (or presence) of the domain wall and the orientation of the domains in the wire (see Fig.3.32 [4]). It was also proposed that such a structure incorporated into a magnetic tunnel junction could allow each of the states to be read as different resistances. [4]

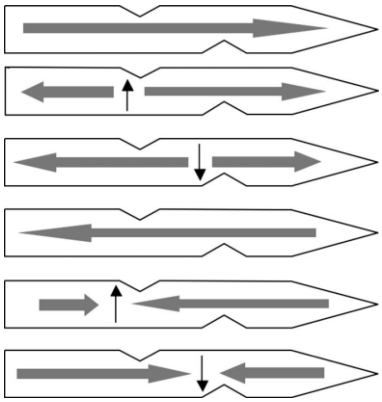

Fig.3.32 – Possible states in a double notched wire allowing for a multibit memory element [1]. Grey arrows show domain magnetisation and black arrows domain wall magnetisation.

Parkin et al. proposed the use of a patterned nanowire containing many domain walls that could be moved through the wire in synchrony using pulses of spin polarised current. The domains between the domain walls could represent data in this form of shift register. If this technology could be adapted to a 'vertical' structure (see Fig.3.33 [5]) it would offer extremely high memory density. The controllable movement of domain walls is critical to prevent domain walls from meeting and annihilating, which would result in the loss of data, therefore reducing the stochasticity of domain wall movement is the key challenge to this system. [2]

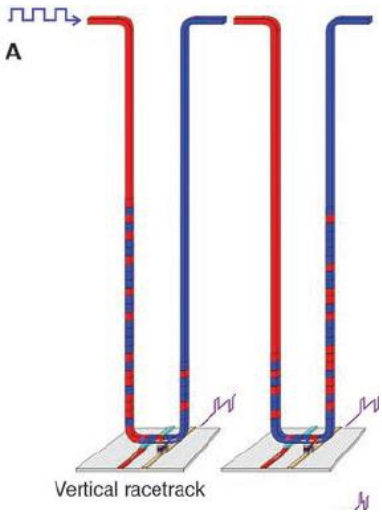

Fig.3.33 – Schematic of vertical ‘racetrack’ memory. Red and blue sections represent opposite magnetisation directions allowing for binary data storage.[5]

Bromberg *et al*. proposed the use of a ‘chain link’ shift register (shown in Fig.L) to allow controllable movement of domain walls through a racetrack like memory.[44] In this system domain walls in sections of electrically insulating nanowire are driven by applying current to a connected spin transfer torque layer. The insulating nanowire sections are connected at their ends allowing domain walls to propagate through the system controllably by applying current only to the desired STT layers.[44]

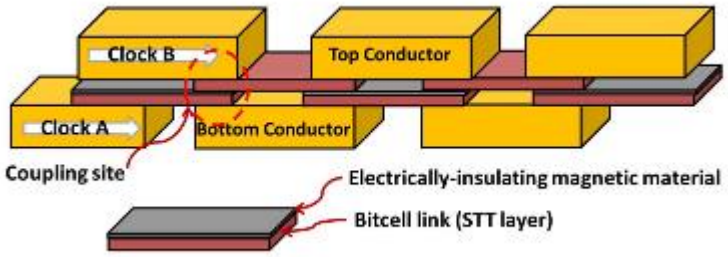

Fig.3.34 – Schematic of the proposed ‘chainlink’ shift register. Electrically insulating magnetic elements are linked at their ends and domain wall movement controlled by selective application of current to the STT layers.[44]

Franken *et al*. showed that more predictable domain wall motion could be achieved in nanowires by inducing a varying anisotropy in a perpendicularly magnetised Pt/Co/Pt multilayer.[45] By subjecting the wires to varying irradiation by focussed ion beam they produced an anisotropy landscape with a 'ratchet' effect on domain walls propagated using magnetic field allowing them to move in one direction only. Energy minima in the landscape produced predictable positions for the domain walls.[45]

Yang *et al*. have shown that racetrack memory based on synthetic antiferromagnets offers the possibility of high energy efficiency and memory density. They showed that domain walls in synthetic antiferromagnets subjected to current pulses can propagate at very high velocities approaching 800 m/s when the magnetisation of the racetrack is near to zero. The stability of the propagating domain walls in the system offers the possibility of densely packed domain walls allowing for increased memory density.[46]

In an alternative to systems driven by magnetic field and spin polarised current, Dean *et al*.[47] proposed a method of controlling domain walls in a racetrack-like memory system using strain-induced magnetic anisotropy gradients to move the domain walls controllably with energy barriers large enough to avoid stochastic behaviour due to thermal effects.[47] The proposed 'artificial multi-ferroic' device (see Fig.3.35 [47]) consists of a magnetostrictive nanowire under a piezoelectric film with patterned electrical contacts overlaid on the film. The operating principle is that voltage applied to appropriate contacts produces non-uniform strains in the piezoelectric film. These are then coupled to the magnetostrictive nanowire inducing a magnetic anisotropy gradient in the wire. Domain walls will experience this as an energy gradient and move into the associated energy well. This study used finite element modelling to show how controllable domain wall movement and selective pinning in the wire could be achieved [47].

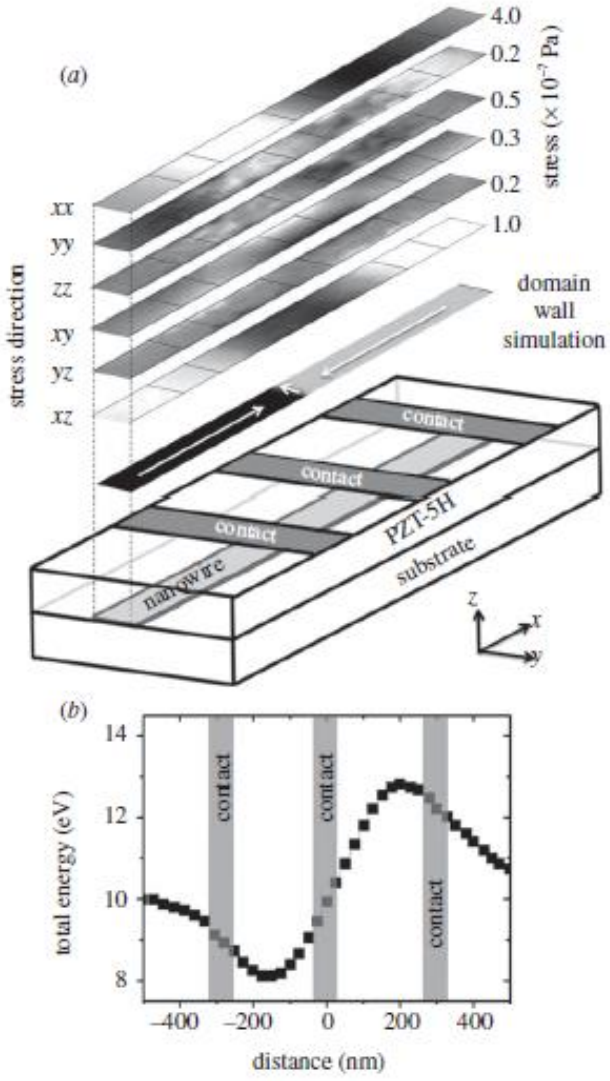

Fig.3.35 – (a) Calculated linear and torsional stress stress terms in a magnetostrictive nanowire resulting from voltage-induced strain in a coupled PZT piezoelectric film. (b) Plot of calculated energy landscape in the wire with the energy minimum providing domain wall trap.[47]

Lei *et al.*[48] demonstrated strain induced pinning of domain walls in a device similar to that proposed by Dean *et al.* The device used by Lei *et al*. shown in Fig.3.36 consisted of a nanowire of a spin valve multilayer applied to a PZT layer with Ti/Au electrodes to control the strain at the wire midpoint.

Investigation by moke demonstrated that the propagation field of domain walls through the strained region could be controlled by varying the voltage applied to the electrodes as shown in Fig.K. Lei *et al*. propose that elements of this type could form the basis of logic or memory devices.[48]

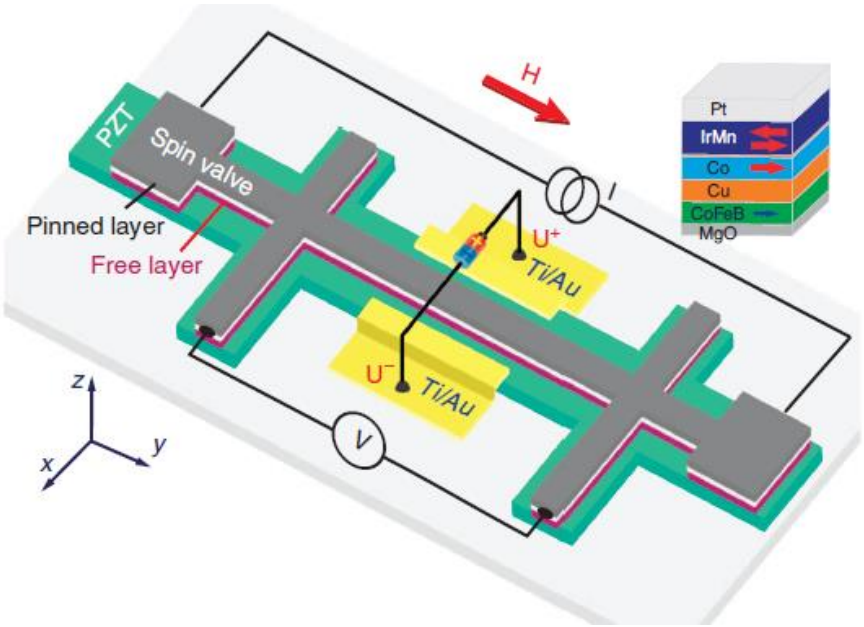

Fig.3.36 – Diagram of the device studied by Lei et al. consisting of a nanowire structure of a spin valve multilayer deposited onto PZT with Ti/Au electrodes at the midpoint allowing control of strain at the midpoint.[48]

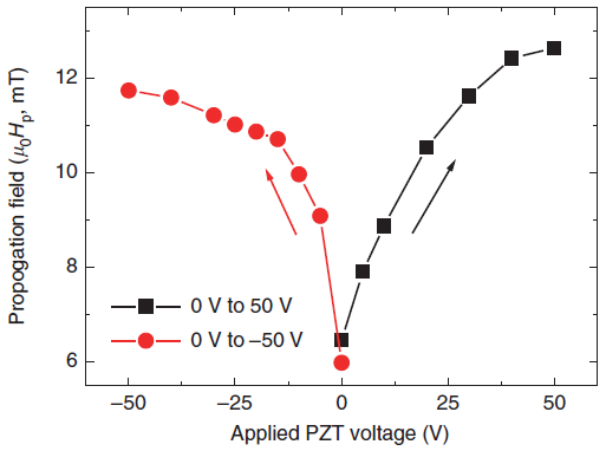

Fig.3.37 – Variation of domain wall propagation field at the strained midpoint with varying applied voltage.[48]

Various MRAM technologies have been proposed using spin transfer torque (STT) to switch the magnetic layer in magnetic tunnel junctions (MTJ).[43] This technology is limited by the requirement to pass a current through the bit. The need to use a current increases the power consumption and limits miniaturisation of transistors limiting both the efficiency and the storage density of such a technology.[43] Other MRAM devices based on magnetic tunnel junctions have been proposed which utilise stress induced anisotropy to aid the switching of MTJs by STT or even to perform the switching purely magnetoelectronically lowering energy requirements of the devices.[43] Using the magnetoelectric effect offers an attractive solution to the problems inherent in STT-MRAM as the stress induced anisotropy can be achieved using a voltage rather than a current thus limiting the power requirements of the device.[43] Fig.3.38 shows the power requirements and write times of various types of RAM technology showing that magnetic RAM and in particular magnetoelectric RAM (Me-RAM) offer very attractive power consumption and write time values.[43]

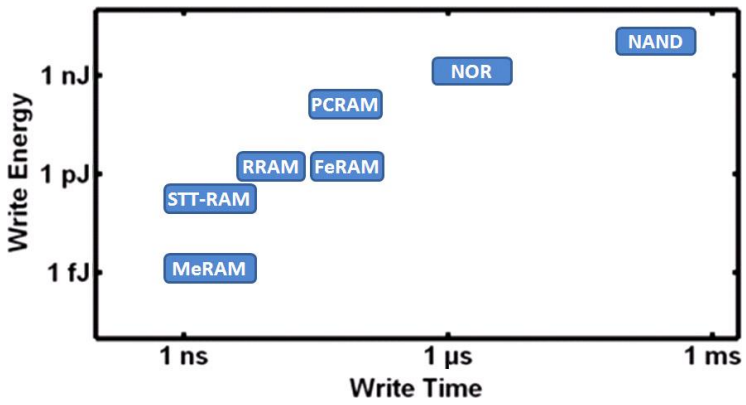

Fig.3.38 – Plot showing write time and energy for various RAM technologies. Magnetoelectric RAM offers the possibility of very fast and efficient RAM [43].

3.5 - Metglas®

Metglas refers to a range of amorphous metallic alloys, the most well known of which are the ferromagnetic alloys based on Fe and B. The lack of a crystal structure gives Metglas alloys unique and attractive magnetic and physical properties – for instance, magneto-crystalline anisotropy (K_1) is zero. This allows other energy terms to dominate the magnetic structure of the material to a much greater extent than is usually observed in other materials. This review will concentrate on their magnetoelastic properties.

The most common form of amorphous alloy is as a long ribbon, due to the need for rapid quenching from melt, and early work appears in the literature regarding this form [49]. Thin films can also be deposited by sputtering and this method is covered by some of the more modern literature.

It was realised that the magnetoelastic (and other) properties could be improved by appropriate treatment of the as-spun ribbon. Two basic types of treatment were developed: stress[49] annealing and field annealing[50]. The annealing process induces an easy axis in the direction of the stress/field.

Early in its development, Egami et al. [49] found that applying stress along the length of ribbons of various Metglas compositions increased the remanence and in some cases lowered the coercivity. The high yield strength of the alloys meant there was no plastic deformation in these cases. Removal of the elastic stress returned the properties to their original values, however it was observed that some of the improvements could be retained by annealing with the applied stress.[49]

Spano et al. [50] later produced field annealed amorphous metallic ribbons by annealing the ribbon with a large magnetic field applied in the plane of the sample but perpendicular to the ribbon length.

The orientation of the field and the annealing temperature were chosen to induce the largest magnetoelastic coupling and they interpreted the magnetoelastic behaviour of the annealed ribbon to a simple domain rotation process.[50] Squire et al. [51] developed a model to describe the effect of field angle on annealing. The model also illustrates how the Young's modulus of the material varies in an applied field (a phenomenon known as the ΔE effect). A plot of ΔE effect against applied field for various angles of field annealing relative to the long axis of METGLAS ribbon is shown in Fig.3.39.[51]

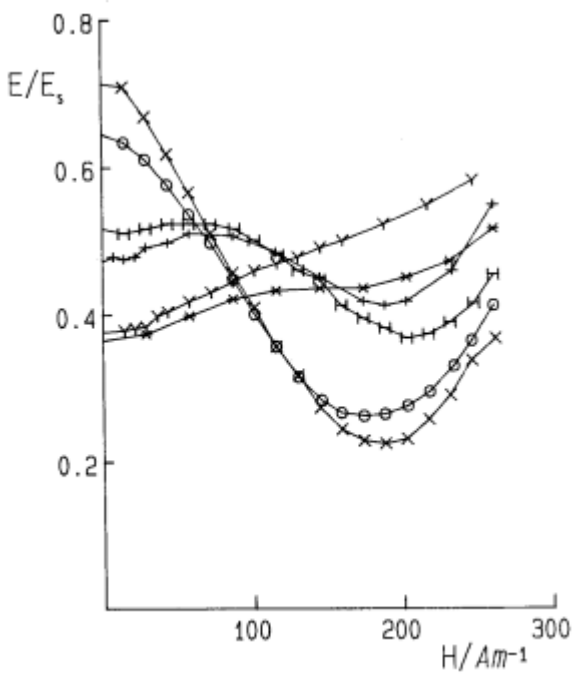

Fig.3.39 – Plot of ΔE effect for various angles of field annealing against applied field (x-90°. o-80°, H-75°, +-70°, Y-6°, *-60°).[51]

The domain structure of the model (shown in Fig.3.40 [51]) consists of domains oriented at an angle *a* from perpendicular to the ribbon. The moments in the domains are distributed

randomly from the mean angle by an angle *b*. Note that ideally *a* should be the angle of the field used during annealing but this will not necessarily be the case. This model fits well with experimental results. [51]

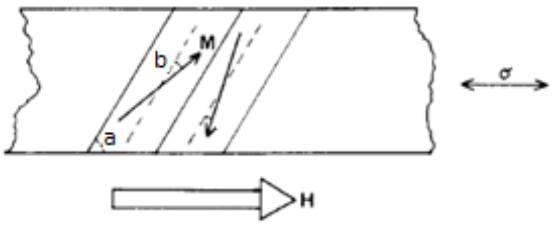

Fig.3.40 – Schematic showing the domain structure used in the model developed by Squire et al.[51]

Thomas et al. studied the effect of the anisotropy induced by field annealing.[52] The expected stripe domains in the direction of the annealing field were observed (see Fig.3.41 [52]). Measurement of M-H loops, λ-H curves and λ_e showed behaviour predicted by moment rotation. Since magnetostriction occurs by moment rotation the ability to induce an easy axis as demonstrated by Thomas et al. offers a means to maximising magnetostriction in amorphous metallic magnets. The results also showed evidence of a distribution of moment orientations around the easy axis as in the model by Squire et al.[52] The results also showed that maximum magnetostriction is achieved before the induced anisotropy from annealing has been reached. Therefore the annealing time and temperature should be chosen to minimise the induced anisotropy in order to achieve maximum magnetostriction [52]. Wallace et al. demonstrated that field annealing also alters the properties of sputtered Metglas films giving their sample's permeability an increased stress dependence.[53]

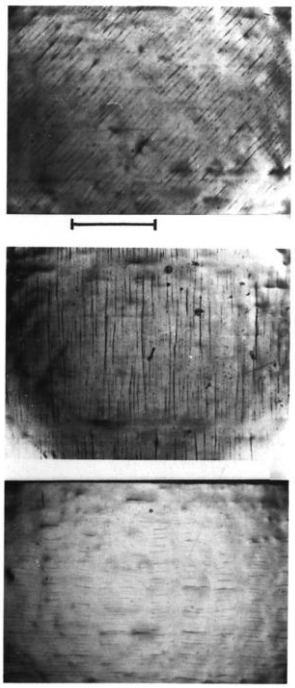

Fig.3.41 – Magneto optical images of magnetic domains in METGLAS ribbon aligned to different field annealing directions.[52]

Lu et al. [54] showed that sputtering a thin film with a 'forming field' applied in the plane of the substrate has a similar effect to a field annealing process. This results in as-deposited films with well-oriented domain structure and saturation magnetostriction of 30 ppm, similar to the value for bulk material. The use of a forming field allows the use of substrates that would not be able to resist the temperatures required for an annealing process. The stray field from magnetron sources can result in radial domain patterns in sputtered Metglas films in the absence of any other forming field (Fig.3.42 [55]), which results in poor magnetoelastic properties. A more uniform alignment can be achieved by positioning the substrate away off-centre to the magnetron [55]. Straining the substrate during growth also orients the domains uniaxially by introducing a stress-induced anisotropy in the film upon removal of the strain [55]. Post-deposition field annealing or strain annealing can also be effective in re-aligning the magnetic easy axis [55]. Varying the strength of the applied field

or stress allows the induced anisotropy to be controlled in the film. Example domain structures induced by these treatments can be seen in Fig.3.43 [55].

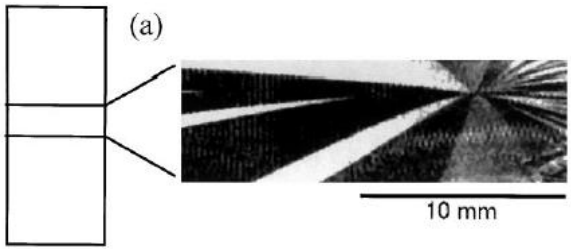

Fig.3.42 – Image of the radial domain pattern induced by the stray field from the RF magnetron sputter gun source used during deposition of a METGLAS film.[55]

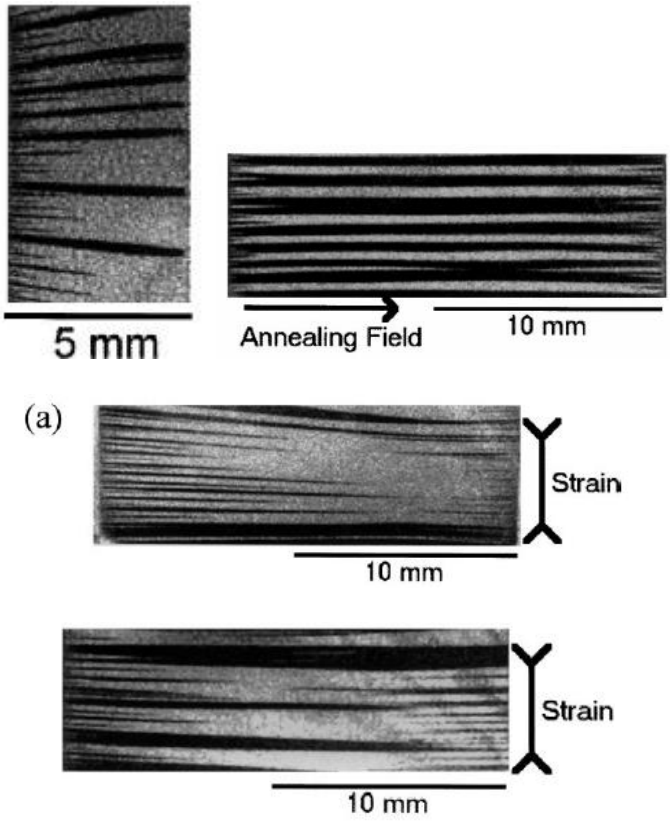

Fig.3.43 – Aligned domain induced by in order: forming field deposition, field annealing, deposition under strain and strain annealing.[55]

3.6 - Galfenol

Galfenol refers to alloys with a composition $Fe_{1-x}Ga_x$. These alloys are attractive as magnetostrictive materials with high saturation magnetostriction, low brittleness and low anisotropy field. This makes them useful in applications where the high brittleness and anisotropy of Terfenol-D alloys is unacceptable. This section will briefly review the literature with regards to obtaining optimal magnetostrictive properties in the bulk and thin film forms.

Bulk Galfenol alloys are composed of three main phases which depend on the Ga content (see Fig. 3.15 [56]). At low Ga content of up to 18% a disordered body centre cubic phase (A2) of Ga solid solution in α-Fe is present.[56] With a rapid quench this phase can be stabilised up to a Ga content of 20%. As the Ga concentration is increased further an ordered body centre cubic phase ($D0_3$) forms. At concentrations of Ga higher than 25% a face centre cubic phase ($L1_2$) forms alongside the $D0_3$ phase.

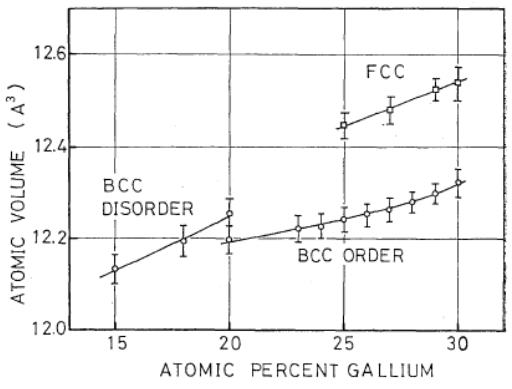

Fig.3.45 – Phase dependence of Galfenol on Ga content.[56]

The variation of the saturation magnetostriction with Ga content in single crystal Galfenol appears to be complicated with two peaks (Fig.3.46) [57]. The first corresponds to the

maximum Ga content which can be achieved without forming $D0_3$ (note however that it has also been suggested that nanoprecipitates of $D0_3$ are essential for the high magnetostriction in the A_2 phase [58]). After this peak the magnetostriction decreases due to the mixture of A2 and $D0_3$ phases. The second peak corresponds to the presence of just the $D0_3$ phase and the magnetostriction is then reduced with increasing Ga content as other phases form.[57] The saturation magnetostriction values shown reach values as high as 440ppm, however these values are for single crystals of Galfenol. Polycrystalline Galfenol exhibits lower magnetostriction due to the random orientation of the grains.[57]

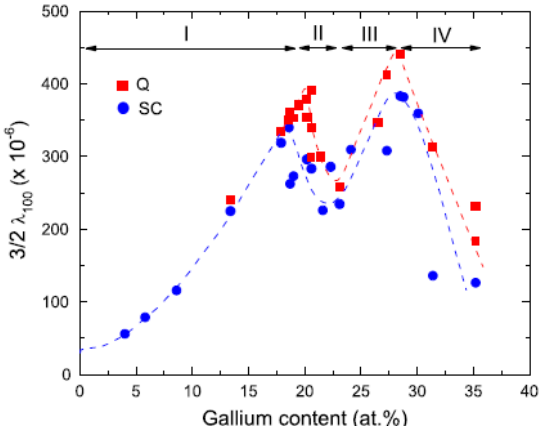

Fig.3.46 – Plot showing the magnetostriction of Galfenol with varying Ga content. Blue circles represent slow cooled alloy and red squares represent quenched alloy.[24]

Rafique et al. studied the effect of varying Ga content on the crystalline anisotropy of single crystal Galfenol [59]. It was found that both K_1 and K_2 reduce to nearly zero at a Ga content of 20% (see Fig.3.47 [59] and Fig.3.48 [59]). As with Metglas, this composition gives the opportunity for magnetostatic (i.e. shape anisotropy) and magnetoelastic energy terms to determine domain structure and magnetic characteristics.

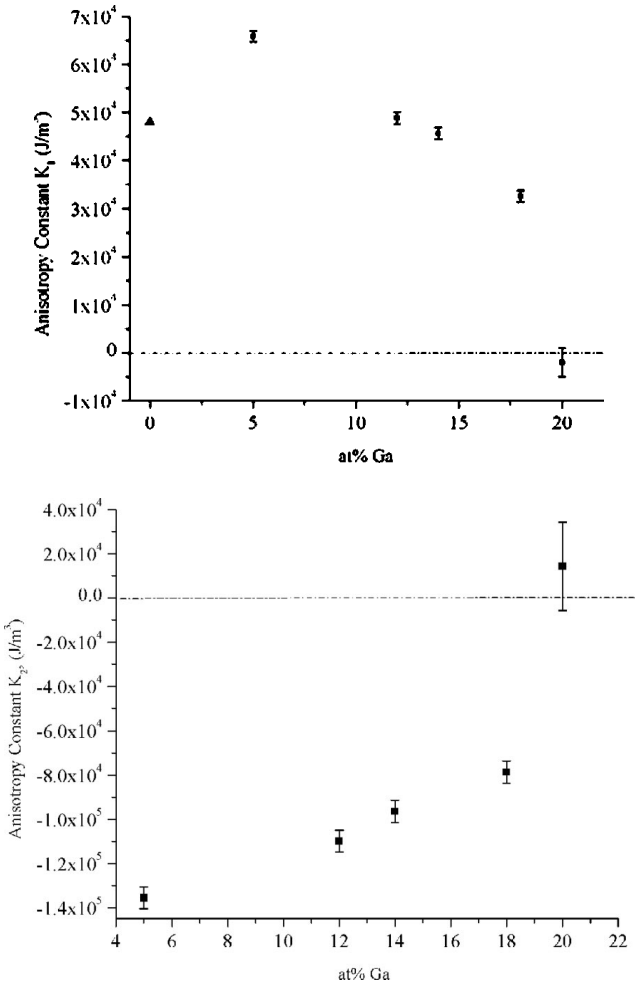

Fig.3.47 and 3.39 - Plots showing the anisotropy constants K_1 and K_2 of Galfenol with varying Ga content.[59]

It is possible to deposit Galfenol as a thin film altering the magnetostrictive properties of the material[60][61][62]. In polycrystalline thin films the film thickness limits the magnetostrictive properties. Javed et al. studied the effect of film thickness on the properties of $Fe_{80}Ga_{20}$ films [60]. It was shown that as film thickness is reduced the grain size and the effective saturation magnetostriction decrease (see Fig.3.49 [60] and Fig.3.50 [60]). It was also shown that the films were magnetically isotropic with the exception of the 20nm thick film which had a weak in plane anisotropy.[60]

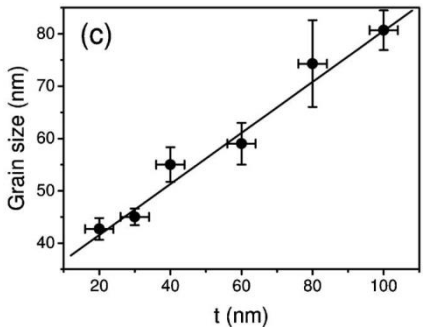

Fig.3.49 – Plot showing variation of grain size in Galfenol thin films with varying film thickness (t).[60]

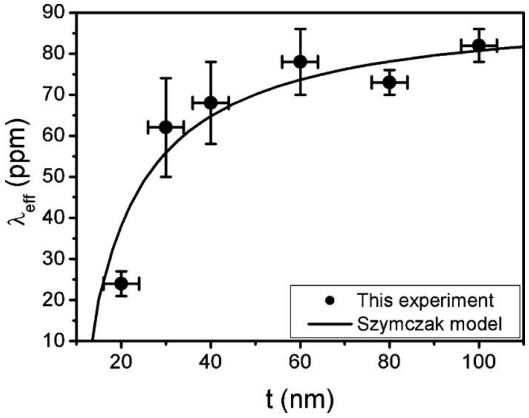

Fig.3.50 – Plot showing variation of effective saturation magnetostriction of Galfenol with varying film thickness (t).[60]

Javed et al. showed that growth of thin films with a forming field produces a pronounced uniaxial anisotropy in the film and reduced the effective saturation magnetostriction.[61] However, results from Wang et al. showed that effective saturation magnetostriction increased with the use of a forming field.[29]

Dean et al. simulated Galfenol thin films with grains randomly oriented and with a degree of texture and showed that a Galfenol film with in plane aligned crystallites could have significantly improved magnetostrictive properties.[63]

3.7 - Thin Film Fatigue

With the growing interest in thin film technologies the properties of thin films have become an important area of research. Due to the highly restricted length scale associated with the film thickness the properties of a film can vary greatly from the bulk properties. One property of particular interest in applications where a thin film or element is deformed is fatigue as this may determine the lifetime of thin film devices.

Kraft et al. [64] set out to perform a systematic study of the effect of film thickness on the fatigue properties of metal films. Using Ag films deposited onto a SiO_2 cantilever the fatigue behaviour of the films were probed by applying a varying load shown as P in Fig.3.51 [64]. By measuring the beam stiffness the onset of damage could be detected as a decrease in stiffness. Fig.3.52 [64] summarises results from a range of film thicknesses and maximum applied strains for a test duration of $3.9x10^6$ cycles. The results indicate that thinner films can withstand a greater maximum strain without damage formation. A Cu film was also tested using a tensile test method with the Cu film deposited onto a polyimide substrate. Kraft et al. studied the damage morphology of the Ag and Cu films and observed extrusions within large grains and intergranular cracks where small grains were present (see Fig.3.53 [64]).

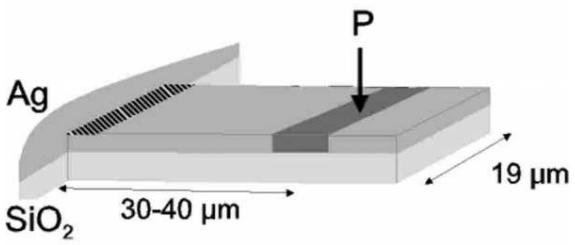

Fig.3.51 – Schematic of thin film fatigue test performed by Kraft et al. Load P is applied to a cantilever with Ag thin film deposited onto it.[64]

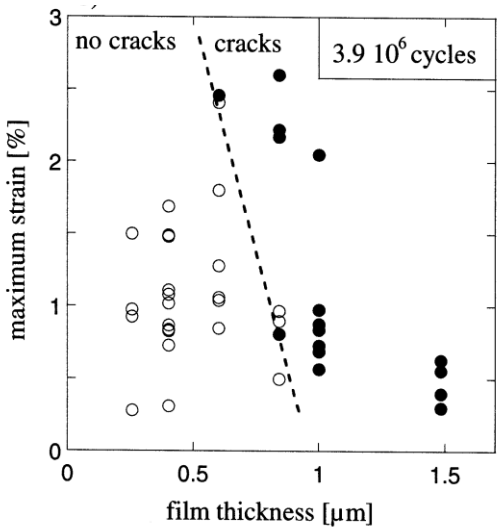

Fig.3.52 – Example of thin film fatigue data showing the increased resistance to damage of films with reduced thickness.[64]

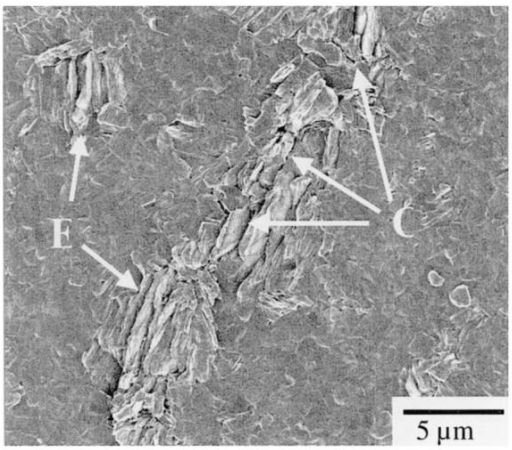

Fig.3.53 – Examples of thin film fatigue damage types. E indicates extrusions and C indicates intergranular cracking.[64]

Zhang et al. studied the literature on thin film fatigue and constructed a phase diagram of fatigue mechanisms (see Fig.3.54 [65]). Region I of the diagram corresponds to bulk-like fatigue behaviour where the dimensions of the film are large enough to allow for the dislocation structures typical of a bulk specimen. Region II is an intermediate region with fatigue mediated by dislocation 'tangles' and small surface extrusions. Region III represents

'small volume' behaviour where the dislocation structures associated with bulk behaviour are suppressed as they are too large to exist in such a small volume. At such small volumes fatigue is caused by cracking along grain boundaries and twin boundaries, voiding at grain boundaries and diffusion of the grain boundaries. The diagram also indicates the film dimensions where the film thickness or the grain size controls the fatigue mechanism of the films. Suppression of the bulk fatigue mechanisms is responsible for the enhanced fatigue resistance of thin films. A region IV is also shown on the phase diagram and represents a hypothetical region for extremely thin films with very fine grains where alternative fatigue mechanisms are expected to exist.[65]

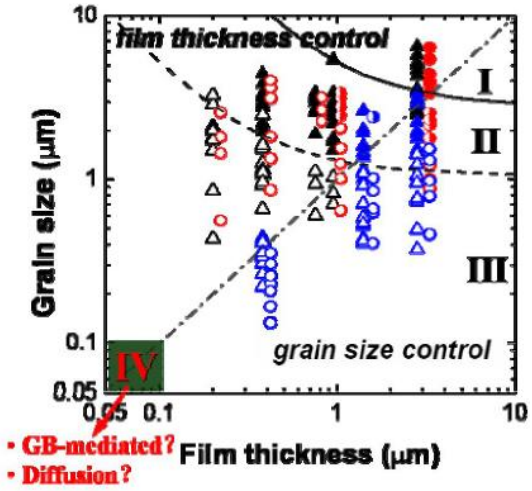

Fig.3.54 – Plot showing the variation of thin film fatigue mechanisms with grain size and film thickness. The plot also shows which of the two dimensions (grain size or film thickness) dominates the properties. Area IV on the plot indicates a hypothetical very thin film region where even the fatigue mechanisms of thin films are inhibited.[65]

Sim et al. studied Ag films deposited onto polymer substrates [66]. By measuring the electrical resistance of the films the onset of fatigue damage could be detected as an increase in the resistance of the film. A resistance increase of 25% was chosen as the criterion for failure. The study showed that the adhesion of the film to the substrate is an

important factor in determining the fatigue resistance of thin films with more strongly bonded films showing greater fatigue resistance. It was proposed that debonding from the substrate was associated with two distinct types of failure involving plastic deformation, the first being the formation of extrusions and the second being localised necking of the film in debonded areas of the film. Both these mechanisms lead to crack formation. It was suggested however that in thinner films (<200nm) a brittle intergranular cracking mechanism is responsible for fatigue and so adhesion will not improve the fatigue life in this case [66].

It can be seen from the literature that the film thickness and grain size of a metallic film have a major influence on the fatigue life of the film. Reducing either of these dimensions improves fatigue life by inhibiting the mechanisms which lead to crack formation and failure of the material. It has been shown also that the adhesion of a film to its substrate influences the fatigue life. As of yet the fatigue properties of very thin films (<100nm) have not been studied, however it is expected that films of this type will have higher fatigue resistance still due to suppression of even the fatigue mechanisms associated with sub-micrometre films.

3.8 - Summary

This review has highlighted the key concepts required to undertake a study on strain based control of domain walls. Information on nanowire and ring structures has been reviewed to show how these structures can be used to contain and control domain walls. Information on multiferroics has been reviewed in order to show how magnetic properties can be controlled electronically in systems with coupled ferroelectric and ferromagnetic properties.

3.9 – References

[1] N.Vernier, D.A.Allwood, D.Atkinson, M.D.Cooke and R.P.Cowburn, *Europhys. Lett.*, **65**, 526 (2004)

[2] D.Atkinson, D.A.Allwood, G.Xiong, M.D.Cooke, C.C.Faulkner and R.P.Cowburn, *Nat. Mater.*, **2**, 85 (2003)

[3] D.A.Allwood, G.Xiong, C.C.Faulkner, D.Atkinson, D.Petit and R.P.Cowburn, *Science*, **309**, 1688 (2005)

[4] D.Atkinson, D.S.Eastwood and L.K.Bogart, *Appl. Phys. Lett.*, **92**, 022510 (2008)

[5] S. P. Parkin, M.Hayashi and L.Thomas, *Science*, **320**, 190 (2008)

[6] D.A.Allwood and M.R.J., Gibbs, Patent Number(s): WO2009004293-A2 ; GB2452474-A ; WO2009004293-A3

[7] Y.Nakatani, A.Thiaville and J.Miltat, *J. Magn. Magn. Mater.*, **290**, 750 (2005)

[8] R.P.Cowburn, D.A.Allwood, G.Xiong, and M.D.Cooke, *J. App. Phys.*, **91**, 6949 (2002)

[9] W.Casey, H.Li, B.S.Han and J.Shi, *J. Appl. Phys.*, **91**, 10, 6943 (2002)

[10] W.Casey and J.Shi, *Appl. Phys. Lett.*, **84**, 5, 759 (2004)

[11] W. Casey and J.Shi, *J. Appl. Phys. Lett.*, **95**, 11, 7031 (2004)

[12] C. Faulkner M.D.Cooke, D.A.Allwood, D.Petit, D.Atkinson and R.P.Cowburn, *J. Appl. Phys.*, **95**, 11, 6717 (2004)

[13] D.A.Allwood, G.Xiong and R.P.Cowburn, *Appl. Phys. Lett.*, **85**, 14, 2848 (2004)

[14] P.Lendecke, R.Eiselt, G.Meier and U.Merkt, *J. Appl. Phys.*, **103**, 073909 (2008)

[15] D.Petit, A.V.Jausovec, H.T.Zeng, E.Lewis, L.O'Brien, D.Read and R.P.Cowburn, *Phys. Rev. B*, **79**, 214405 (2009)

[16] D.Petit, A.V.Jausovec, D.Read and R.P.Cowburn, *J. Appl. Phys.*, **103**, 114307 (2008)

[17] L.K.Bogart, D.S.Eastwood and D.Atkinson, *J. Appl. Phys.*, **104**, 033904 (2008)

[18] M.Im, L.Bocklage, P.Fischer and G.Meier, *Phys. Rev. Lett.*, **102**, 147204 (2009)

[19] J.Akerman, M.Muñoz, M.Maicas and J.L.Prieto, *Phys. Rev. B*, **82**, 064426 (2010)

[20] G.S.D.Beach, C.Nistor, C.Knutson, M.Tsoi and J.L. Erskine, *Nat. Mater.*, **4**, 741 (2005)

[21] N.L.Schryer Walker, L. R., *J. Appl. Phys.*, **45**, 12, 5406 (1974)

[22] M.T.Bryan, T.Schrefl, D.Atkinson, and D.A.Allwood, *J. App. Phys.*, **103**, 073906 (2008)

[23] Jun-Young Lee, Ki-Suk Lee, and Sang-Koog Kim, *App. Phys. Lett.*, **91**, 122513 (2007)

[24] J.Dean, M.T.Bryan, D.A.Allwood, S.Bance, M.A.Bashir, G.Hrkac, A.Goncharov and T.Schrefl, *IEEE Trans. Magn.*, **45**, 10, 4067 (2009)

[25] T.J.Hayward, T.A.Moore, D.H.Y.Tse, J.A.C.Bland, F.J.Castaño and C.A.Ross, *Phys. Rev. B*, **72**, 184430 (2005)

[26] M.Kläui, C.A.F.Vaz, L.Lopez-Diaz and J.A.C.Bland, *J. Phys Condens. Matter*, **15**, R985 (2003)

[27] K.Yamada, S.Kasai, Y.Nakatani, K.Kobayashi, H.Kohno, A.Thiaville and T.Ono, *Nat. Mater.*, **6**, 269 (2007)

[28] Y.G.Yoo, M.Kläui, C.A.F.Vaz, L.J.Heyderman and J.A.C.Bland, *Appl. Phys. Lett.*, **82**, 15, 2470 (2003)

[29] F.J.Castaño, C.A.Ross, A.Eilez, W.Jung and C.Frandsen, *Phys. Rev. B*, **69**, 144421 (2004)

[30] M.Kläui, C.A.F.Vaz, L.J.Heyderman, U.Rüdiger and J.A.C.Bland, *J. Magn. Magn. Mater.*, **290**, 61 (2005)

[31] W.Zhang and S.Haas, *Phys. Rev. B*, **81**, 064433 (2010)

[32] R.P.Cowburn, D.K.Koltsov, A.O.Adeyeye, M.E.Welland and D.M.Tricker, *Phys. Rev. Lett.*, **83**, 5, 1042 (1999)

[33] M.Fiebig, *J. Phys. D: Appl. Phys.*, **38**, R123 (2005)

[34] E.Ascher, H.Rieder, H.Schmid and H.Stössel, *J. Appl. Phys.*, **37**, 3, 1404 (1966)

[35] C.Nan, M.IBichurin, S.Dong, D.Viehland and G.Srinivasan, *J. Appl. Phys.*, **103**, 031101 (2008)

[36] F.Zavaliche, T.Zhao, H.Zheng, F.Straub, M.P.Cruz, P.L.Yang, D.Hao and R.Ramesh, *Nano Lett.*, **7**, 6, 1586 (2007)

[37] T.Chung, S.Keller and G.P.Carman, *Appl. Phys. Lett.*, **94**, 132501 (2009)

[38] T.Chung, K.Wong, S.Keller, K.L.Wang and G.P.Carman, *J. Appl. Phys.*, **106**, 103914 (2009)

[39] M.Weiler, A.Brandlmaier, S.Geprägs, M.Althammer, M.Opel, C.Bihler, H.Huebl, M.S.Brandt, R.Gross and S.T.B.Goennenwein, *New J. Phys.*, **11**, 013021 (2009)

[40] T.Brintlinger, S.Lim, K.H.Baloch, P.Alexander, Y.Qi, J.Barry, J.Melngailis, L.Salamanca-Riba, I.Takeuchi and J.Cumings, *Nano Lett.*, **10**, 1219 (2010)

[41] S.Brivio, D.Petti, R.Bertacco and J.C.Cezar, *Appl. Phys. Lett.*, **98**, 092505 (2011)

[42] J.L.Hockel, A.Bur, T.Wu, K.P.Wetzlar and G.P.Carman, *Appl. Phys. Lett.*, **100**, 022401 (2012)

[43] P.K.Amiri and K.L.Wang, *Spin*, **2**, 1240002 (2012)

[44] D.M.Bromberg, D.H.Morris, L.Pileggi, and J.Zhu, *IEEE Trans. Mag*., **49**, 4394 (2012)

[45] J.H.Franken, H.J.M.Swagten and B.Koopmans, *IEEE Trans. Mag.*, **48**, 3219 (2012)

[46] Yang, K. Ryu and S.Parkin, *Nat. Nanotechnol.*, **10**, 221 (2015)

[47] J.Dean, M.T.Bryan, T.Schrefl and D.A.Allwood, *J. Appl. Phys.*, **109**, 023915 (2011)

[48] N.Lei *et al.*, Nat. Commun., 4:1378 (2013)

[49] T.Egami, P.J.Flanders and C.D.Graham, *Appl. Phys. Lett.*, **26**, 3, 128 (1975)

[50] M.L.Spano, K.B.Hathaway and H.T.Savage, *J. Appl. Phys.*, **53**, 2667 (1982)

[51] P.T.Squire and M.R.J.Gibbs, *IEEE Trans. Magn.*, **25**, 5, 3614 (1989)

[52] A.P.Thomas and M.R.J.Gibbs, *J. Magn. Magn. Mater.*, **103**, 97 (1992)

[53] J.L.Wallace, *J. Appl. Phys.*, **73**, 10, 5360 (1993)

[54] Y.Lu and A.Nathan, *Appl. Phys. Lett.*, **70**, 4, 526 (1997)

[55] M.Ali, R.Watts, W.J.Karl and M.R.J.Gibbs, *J. Magn. Magn. Mater.*, **190**, 199 (1998)

[56] N.Kawamiya, K.Adachi and Y.Nakamura, *J. Phys. Soc. Jpn.*, **33**, 5, 1318 (1972)

[57] Q.Xing, Y.Du, R.J.McQueeney and T.A.Lograsso, *Acta Mater.*, **56**, 4536 (2008)

[58] H.Cao, P.M.Gehring, C.P.Devreugd, J.A.Rodriguez-Rivera, J.Li and D.Viehland, *Phys. Rev. Lett.*, **102**, 127201 (2009)

[59] S.Rafique, J.R.Cullen, M.Wuttig and Jun Cui, *J. Appl. Phys.*, **95**, 11, 6939 (2004)

[60] A.Javed, N.A.Morley and M.R.J.Gibbs, *J. Appl. Phys.*, **107**, 09A994 (2010)

[61] N.A.Morley, A.Javed and M.R.J.Gibbs, *J. Appl. Phys.*, **105**, 07A912 (2009)

[62] B.W.Wang, S.Y.Li, Y.Zhou, W.M.Huang, S.Y.Cao, *J. Magn. Magn. Mater.*, **320**, 769 (2008)

[63] J.Dean, M.T.Bryan, N.A.Morley, G.Hrkac, A.Javed, M.R.J.Gibbs and D.A.Allwood, *J. Appl. Phys.*, **110**, 043902 (2011)

[64] O.Kraft, R.Schwaiger and P.Wellner, *Mat. Sci. Eng.*, **A319**, 919 (2001)

[65] G.P.Zhang, *Thermal, Mechanical and Multi-Physics Simulation Experiments in Microelectronics and Micro-Systems, 2007. EuroSime 2007. International Conference on*, 1 (2007)

[66] G.Sim, Y.Hwangbo, H.H.Kim, S.B.Lee and J.J.Vlassak, *Scr. Mater.*, **66**, 915 (2012)

4 - Experimental Methods

In this chapter the experimental methods used in this work are described. The techniques described are used in the production of patterned magnetic structures and in the characterisation of their structure and behaviour.

4.1 - Electron Beam Lithography

Electron beam lithography (EBL) is used in the preparation of resists for the deposition of magnetic structures below the resolution achievable using optical lithography. This is possible because the wavelength of the electrons used in EBL is lower than the wavelength of light used in optical lithography. Fig.4.1 shows the stages involved in producing a pattern using a positive resist.

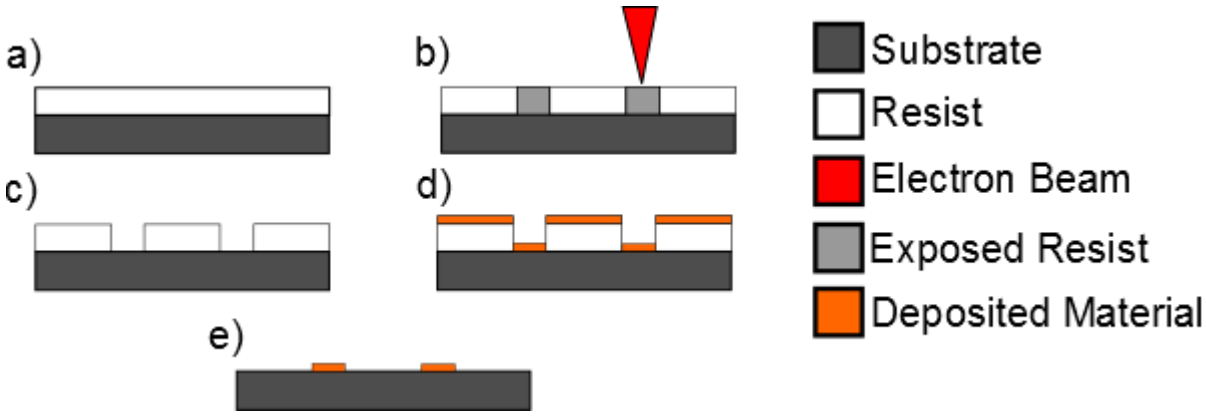

Fig.4.1 – Stages of EBL using a positive resist.

The five stages of EBL shown in Fig.4.1 are described below.

In the first stage a resist material is applied to a substrate material (Fig. 4.1a). When producing magnetic nanostructures the most common substrate material is silicon wafer as

it provides an extremely smooth surface onto which structures can be deposited. The most common resist material is poly(methyl methacrylate) (PMMA) as it provides a cheap and reliable positive resist. The resist is applied to the substrate by spin coating with a solution containing the resist material. This provides an approximately even thickness of resist across the substrate material and allows control of the resist thickness by controlling the concentration of the resist material in solution or the spin speed. The higher the concentration of the resist solution the higher its viscosity resulting in a thicker layer being formed during spin coating. After spin coating, heating is used to evaporate the solvent to leave the resist layer on the surface of the substrate. The thickness of a PMMA resist can typically range from 50nm up to 5µm.

Next a focussed electron beam scans the resist with the desired pattern (Fig. 4.1b). The electrons in the beam have sufficient energy to penetrate through the resist and into the substrate below. Where the resist has been exposed to the electron beam its properties are altered. In the case of PMMA (and other 'positive' electron beam resists) the degree of cross linking of polymer chains is decreased in the exposed material. Note that when using a negative resist, exposure to the electron beam increases the degree of cross-linking.

The resist is then 'developed' in a solvent for a controlled time at a controlled temperature in order to remove material at a predictable rate. This resist development process allows comparable results to be achieved reproducibly. In the case of a positive resist the previously exposed resist material dissolves at a much faster rate than the unexposed material uncovering the substrate material where the exposed resist has been dissolved away (Fig. 4.1c). The opposite is true of a negative resist so that resist development leaves the substrate covered where the resist has been exposed. In either case, after dissolving

the desired amount of resist the sample must then be rinsed in a solvent which will not remove any more material. This can be iso-propanol when using a PMMA resist.

Once the resist is ready, the final desired material can be deposited onto the sample using any one of a number of thin film deposition methods (e.g. evaporation, sputtering). Where the resist has been removed the material will be deposited onto the substrate. Where the resist has not been removed the material is deposited onto the surface of the resist (Fig. 4.1d).

The final stage of the process is 'lift off'. A solvent is used to dissolve the remaining resist material thus removing any deposited material on the resist from the sample and leaving only the material deposited on the substrate behind (Fig. 4.1e). The process is usually aided by use of an ultrasonic bath, which speeds up the removal of the resist and helps prevent the removed material from being deposited on the surface of the substrate.

4.2 - Thermal Evaporation

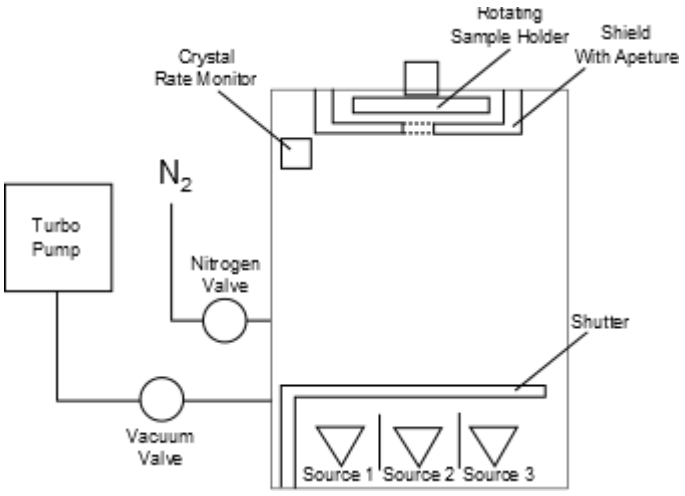

Fig.4.2 – Schematic diagram of the thermal evaporation chamber used in this work.

Thermal evaporation is a thin film deposition technique that uses a resistively heated crucible to evaporate a material inside a vacuum chamber in order to deposit the material onto a substrate. The use of a vacuum reduces contamination of the film by oxygen, increases the amount of evaporated material which reaches the substrate and reduces the temperature required to achieve a high enough vapour pressure for evaporation to occur.

Fig.4.2 shows a schematic representation of the custom-built Wordentec thermal evaporator used in this work. Three evaporation sources are available and the rotating sample holder has slots for up to five substrates allowing for multiple films to be deposited per pump down. The thickness of the deposited film can be monitored in real time using the quartz crystal rate monitor. Thickness is calculated using the density and acoustic impedance of the material along with a tooling factor. The tooling factor is calculated by plotting the actual thickness of calibration samples measured using AFM against the reported thickness from the rate monitor as shown in Fig.4.3.

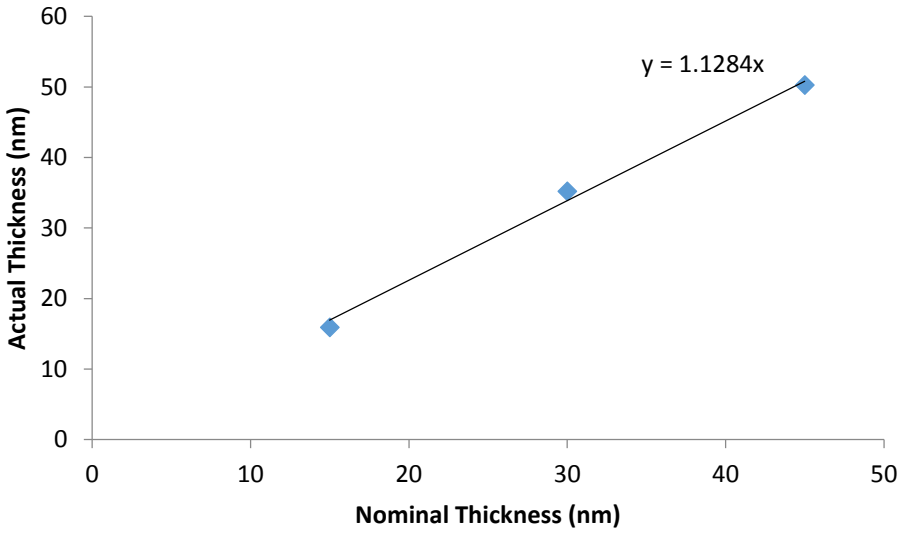

Fig.4.3 – Tooling factor calculation for Ni. The tooling factor is equal to the gradient of the line of best fit, 1.1284.

The material to be deposited is placed in powder form into a crucible. The crucible is placed in the chamber, which is then sealed and the pressure reduced using a vacuum pump. The Wordentec evaporator uses a rotary-backed turbomolecular pump to achieve base pressures lower than 10^{-7} mTorr. Once at working pressure the crucible is heated by applying an electric current. This is done in stages so as not to thermally shock the crucible and damage it. The material is first allowed to evaporate slowly (e.g. <1 nm/s on the crystal rate monitor) for a short time (few minutes) without being deposited on substrates to allow impurities to be driven off. This stage is referred to as bake out and is required to improve the purity of the film. The applied current is ramped back down and the chamber is allowed to return to a suitable working pressure before heating the material again in order to deposit onto a substrate. When heated the partial pressure of the material increases causing it to evaporate. The vapour condenses once it reaches a cool surface such as the substrate or rate monitor where it forms a film.

4.3 - Sputtering

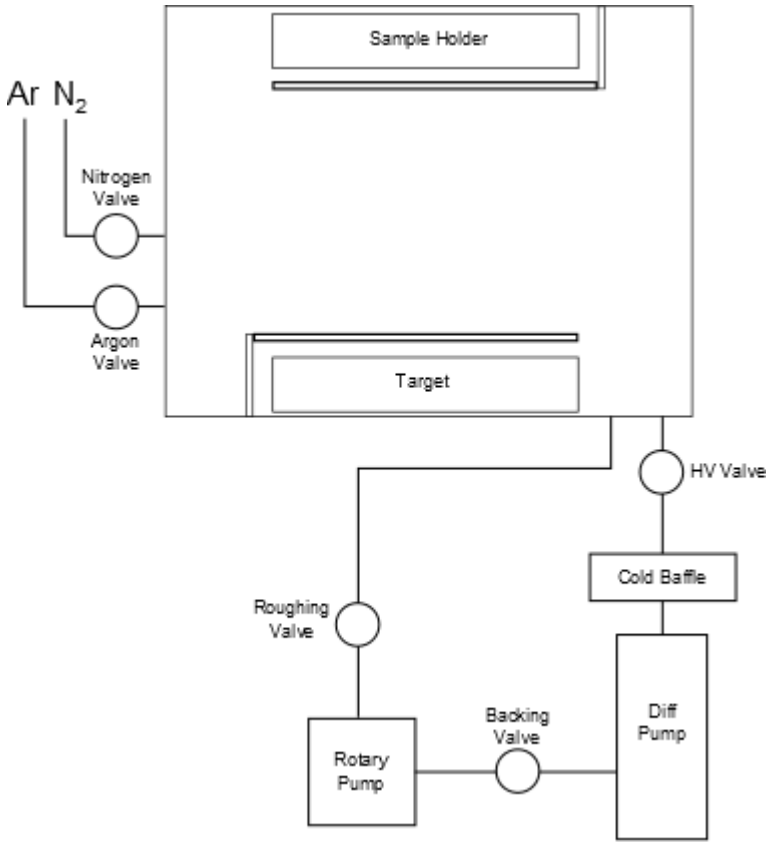

Fig.4.4 – Schematic diagram of the DC sputtering chamber used in this work.

Sputtering is a thin film deposition technique which uses a plasma to bombard a material with ions in order to eject material onto a substrate.

Fig.4.4 shows a schematic of the Nordiko NM2000 RF magnetron sputtering system used in this work. Sputtering is performed in a vacuum chamber as this allows for high purity of deposited films, good deposition rates and is necessary for the creation of a plasma. First the substrate and a target made of the material to be deposited are placed into the chamber. Once the evacuated chamber has reached a low base pressure (2E-6 Torr) an inert gas, in this case argon, is pumped into the chamber at a low pressure (5E-3 Torr)). A large negative voltage is applied to the target, made of the material to be deposited, causing argon atoms in the chamber to be ionised by the electric field produced in the

chamber. The electrons from the ionised atoms can also ionise other atoms as they are ejected, this effect can be further enhanced by the use of a magnetron which uses a large magnetic field to confine ejected electrons near to the target increasing the intensity of the plasma near to the target. The positively charged atomic nuclei are attracted towards the target due to the large negative electric field and bombard the target surface transferring energy to the atoms of the target material. This causes them to be ejected into the chamber where they may reach and be deposited onto the substrate.

Magnetic materials such as the METGLAS used in this work may be deposited with anisotropy induced by the magnetic field from the magnetron. This can lead to a degree of uncontrolled and non-uniform anisotropy in the films, which can compromise their use. To avoid this, the Nordiko sputterer has a pair of permanent magnets attached to the sample holder which apply a strong uniaxial field to the film as it forms to induce a controlled uniaxial anisotropy.

4.4 - Focussed Magneto Optic Kerr Effect

The magneto optic Kerr effect (MOKE) refers to the rotation of the plane of polarisation of light reflected from a magnetic sample due to magnetic circular dichroism caused by the magnetisation in the sample. Since the change in polarisation is close to proportional to the magnetisation it is a useful effect to use when measuring magnetisation changes of thin films and nanostructures as it gives results quickly, is non-destructive, requires no special sample preparation and is highly surface sensitive. Fig.4.5 shows the basic components of a MOKE system.

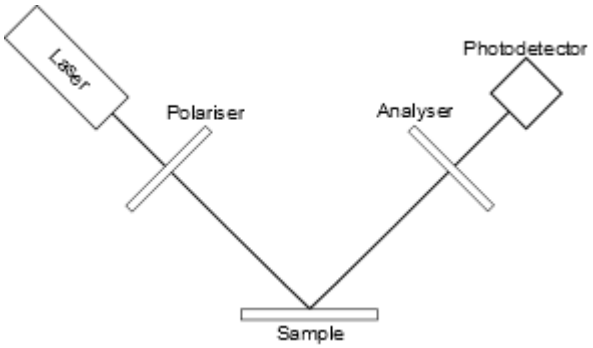

Fig.4.5 – Basic components of a MOKE system.

Light from a laser source is plane polarised using a polariser. The plane polarised light is reflected from the sample and the reflected beam passes through a polariser referred to as the analyser. The analyser is set at an angle close to that which would filter out the plane polarised beam. The intensity of the beam is then recorded using a photodetector. Any rotation of polarisation in the reflected beam due to the magnetisation in the sample is converted by the analyser into a change in the intensity of the light incident on the photodetector. The change in polarisation can be considered to be proportional to the magnetisation in the sample[1]. Therefore the change in the intensity of the beam measured by the photodetector can be considered to be proportional to the magnetisation of the sample.

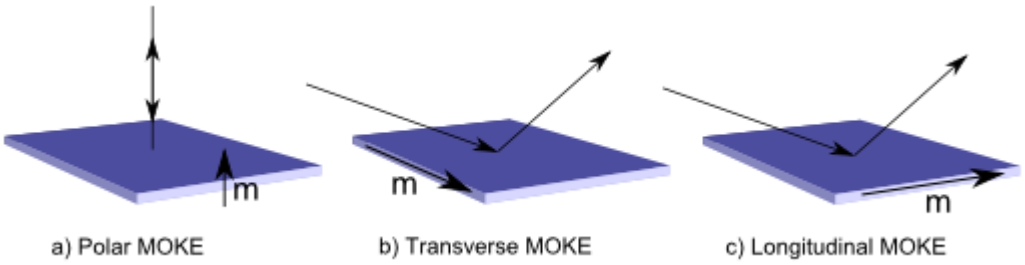

Fig.4.6 – The three possible geometries of MOKE measurements.

There are three possible geometries possible when making MOKE measurements which depend on the orientation of the magnetisation of the sample with relation to the incident beam. Transverse and longitudinal MOKE both measure in plane magnetisation while polar MOKE measures out of plane magnetisation. In transverse MOKE the beam direction is perpendicular to the field direction, in Longitudinal MOKE the beam is parallel to the field direction and in polar MOKE the beam is usually perpendicular to the sample surface.

In this study a focussed MOKE system was used to allow analysis of magnetic nanostructures. The optical components of the system are shown in Fig.4.7. A 2W Coherent Verdi laser emitting light of 532 nm wavelength was used. This has very low noise performance (as low as 0.02% from 10Hz-1GHz) but the high power beam (0.2W for measurements) was attenuated to 10% of its original intensity to avoid sample heating. A Glan-laser polariser was used to plane polarise the beam and a neutral density filter is also included which could be moved into the beam path to attenuate the beam intensity further during alignment. An optional quartz polarisation rotator was used to select between S and P-polarised light. A white light source was directed into the beam path using a beam splitter and the white light and laser are focussed onto the sample surface using a condenser lens to achieve a beam spot size of 4 µm x 7 µm. An objective lens after the sample was used to image the reflected white light and beam onto a CCD camera using a pellicle beam splitter in order to observe the surface features of the sample. A quarter wave plate was used to remove any ellipticity from the reflected beam before the analysing polariser. A photodetector is used to measure the intensity of the beam passing through the analyser.

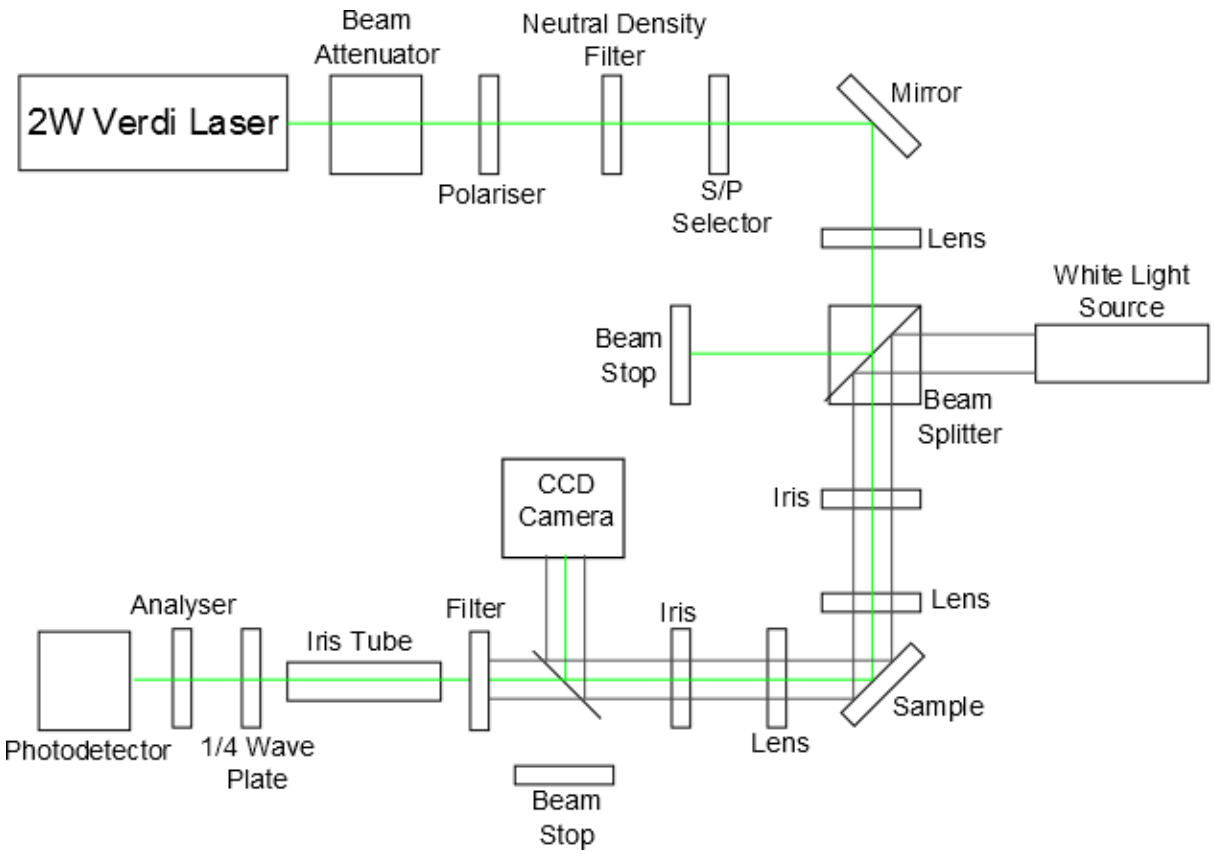

Fig.4.7 – Diagram of the optical components of the focussed MOKE system.

The electronic components of the system are shown in Fig.4.8. The system can be controlled using the PC. Waveforms from the PC are sent to Kepco bipower power amplifiers which supply current to the a quadrupole electromagnet around the sample to apply magnetic fields in the horizontal (x) and vertical (y) directions. The induced emf from pick up coils around electromagnet pole pieces are monitored with two of the available four analogue input channels (channels 1 and 2) of a 1 GHz Agilent digital storage oscilloscope (DSO). These allow the field profiles to be measured. The frequency and amplitude of the field waveform is controlled from the PC. The frequency of the waveform provides a reference signal for a lock in amplifier to amplify the signal from the photodetector in order to filter out components of the photodetector signal not associated with the sample's response to the applied magnetic field and is used when finding the location of samples. A square wave of the same frequency is also sent to the digital input

channel 0 the DSO as a reference signal. Analogue channel 3 of the DSO measures the signal from the photodetector. Multiple field cycles are recorded on the DSO to allow subsequent multi-cycle averaging upon transferal of data to the PC. The signal-to-noise ratio of measurements is improved further by multi-trace averaging on the DSO. Transferral of the data from the DSO to the PC allows a parametric plot of magnetic field and Kerr signal to be created to observe magnetic hysteresis loops of samples. Samples are mounted on an XYθ translation stage that allows sub-micrometre sample positioning. The stage controller can be operated using software on the PC.

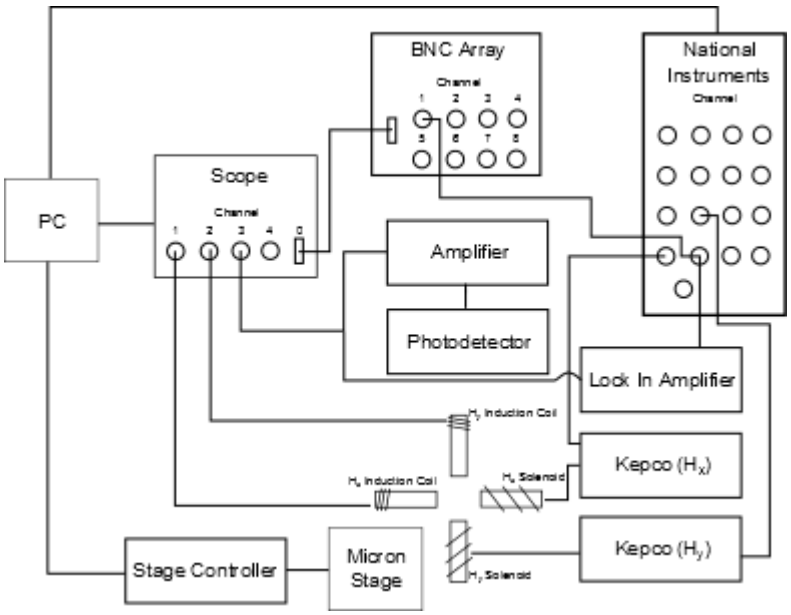

Fig.4.8 – Diagram of the electrical components of the focussed MOKE system.

4.5 - Atomic Force Microscopy / Magnetic Force Microscopy

Atomic force microscopy (AFM) is a widely used imaging technique that provides a three dimensional image of the surface topography of a sample with nanometre resolution. It is particularly useful as measurements can be made without the need for vacuum systems or special preparation of the sample (beyond the need for the sample to fit into the system).

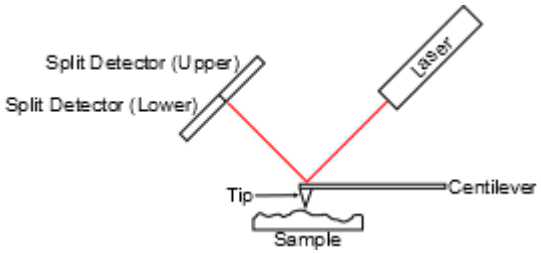

Fig.4.9 – Diagram of an AFM system.

In AFM a probe (usually Si with a length of around 20 µm and a tip radius of around 10 nm) on the end of a cantilever is scanned over the surface of the sample. The probe is controlled by a piezoelectric stack allowing very fine control (sub-Ångstrom) of the probe height over the sample and the fine movement required to scan the probe over the surface. The probe interacts with the surface of the sample causing the cantilever to be deflected depending on the surface forces experienced by the probe. The deflections of the cantilever are measured by reflecting a laser from the cantilever onto a quadrant photodiode with deflections being registered due to the change in the amount of the reflected beam incident on the different sections of the photodetector (as shown in Fig.4.10). It can be seen in Fig. 4.10a that attraction of the probe to the surface causes more of the beam to be reflected into the lower half of the detector while the probe being repelled from the surface reflects more of the beam into the upper half of the detector.

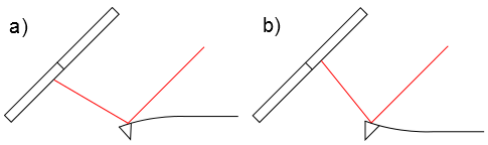

Fig.4.10 – Diagram showing the detection of cantilever deflection by a split photodetector. a) Detection of upward deflection due to laser in upper section of detector. b) Detection of downward deflection due to laser in lower section of detector.

The AFM system used in this work has settings for contact mode measurements and for tapping mode measurements. In contact mode the probe is simply scanned over the surface of the sample. The topology of the sample can then either be measured by keeping the scan height of the probe constant and measuring the deflection of the cantilever or by using a feedback loop to keep the deflection of the cantilever constant by adjusting the scan height of the probe. In tapping mode the cantilever is oscillated and the distance from the sample surface is measured by adjusting the scan height of the cantilever using a feedback loop to keep the frequency of the oscillation constant as the frequency changes due to the tip's interaction with the sample. The advantage of tapping mode is that the reduced contact with the sample surface reduces wear on both the probe and on the sample.

It is also possible to measure the magnetic profile of a sample using a technique called magnetic force microscopy (MFM). In MFM the probe is coated with a magnetic material (e.g. Co) which is magnetised such that the cantilever is deflected when the probe interacts with stray magnetic field from the sample. This makes it useful for imaging magnetic configurations such as domain walls or samples with out of plane magnetisation.

4.6 - Micromagnetic Modelling

Micromagnetic simulations use the Landau Lifshitz Gilbert equation (LLG equation) of motion to calculate the spatially varying magnetisation dynamics of magnetic elements. This equation allows the time varying magnetisation of a magnetic material to be calculated based on the material properties, shape and external field applied to the material. The LLG equation is shown below[3]:

$$\frac{d\boldsymbol{M}_S}{dt} = \gamma_G\left[\boldsymbol{M}_S \times \boldsymbol{H}_{eff}\right] - \frac{\propto_G}{\boldsymbol{M}_S}\left[\boldsymbol{M}_S \times \frac{d\boldsymbol{M}_S}{dt}\right] \quad (4.1)$$

$\frac{d\boldsymbol{M}_S}{dt}$ is the time derivative of the magnetisation $\boldsymbol{M}_S$, γ_G is the gyromagnetic ratio and $\propto_G$ is the Gilbert damping. $\boldsymbol{H}_{eff}$ is the effective field experienced by the material taking into account the applied field, demagnetising field and contributions from the exchange and anisotropy of the material.

In micromagnetic simulation the simulated object is meshed to divide it into small elements and the LLG equation is solved for these cells giving an approximation of the magnetisation state throughout the material. In general the smaller the cell size is the more accurate this estimate will be, though the LLG equation will not provide accurate results at atomic scales as it describes the behaviour of a space containing multiple atoms. Two methods are commonly used known as finite element method (FEM) and finite difference method (FDM).

FEM and FDM are methods of solving systems of partial differential equations (PDEs) in order to simulate a system. FDM is the simpler of the techniques and involves the discretisation of the PDE using a square network. A Taylor expansion is used in order to approximate the differential equations. Though it is a simpler system than FEM the need for a square network makes it less suitable for complex geometries.

In FEM an integral form of the governing equations is used allowing for more complex geometries to be simulated since this does not require any special mesh structure to be implemented.

Two micromagnetic packages have been used in this study in order to simulate the behaviour of nanoscale magnetic structures.

The first is femme[5]. This code is suitable for the study of time varying magnetisation and time varying magnetic fields. Femme is a finite element code. Pre-processing for the simulations performed using femme was done using GiD[6] in order to define the geometry of the problems and for meshing. Visualisation of the data from femme simulations was performed using Paraview[7].

The second micromagnetic simulation package was MuMAX[8]. MuMAX is a finite difference code. MuMAX offers the ability to simulate MFM images from the calculated stray field of simulated elements.

4.7 - Substrate Preparation

In order to achieve the highest possible strains on deposited nanostructures a novel multicomponent substrate was designed. Fig.4.11 shows a cross section of the substrate. A Si wafer was used as a base in order to provide rigidity to the substrate preventing the aluminium and PMN-PT layers from breaking apart from each other, it also provides a very flat base for the device. The PMN-PT was sandwiched between two pieces of aluminium which acted as electrodes using a gold filled epoxy to bond the aluminium to the PMN-PT. A gold filled epoxy was used as its conductivity allows for a high electric field across the PMN-PT when a voltage was applied to the aluminium electrodes. The material used to bond the aluminium and PMN-PT sandwich structure to the Si wafer was an epoxy as the two aluminium electrodes must be electrically insulated from each other. The device was capped with a planarising layer of hydrogen silsesquioxane (HSQ) to provide an extremely low surface roughness, the thickness of this layer is 30 – 60 nm reducing the strain relaxation through the planarising layer to a minimum. The planarising layer was used as even after polishing the best results achieved were a peak to trough depth on the order of 10nm as can be seen in the AFM scan in Fig.4.12.

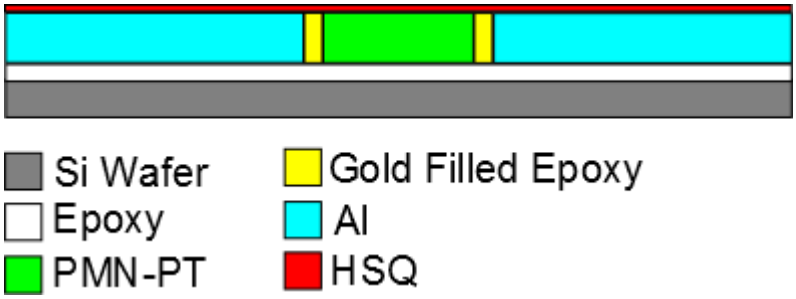

Fig.4.11 – Cross section of multi component substrate.

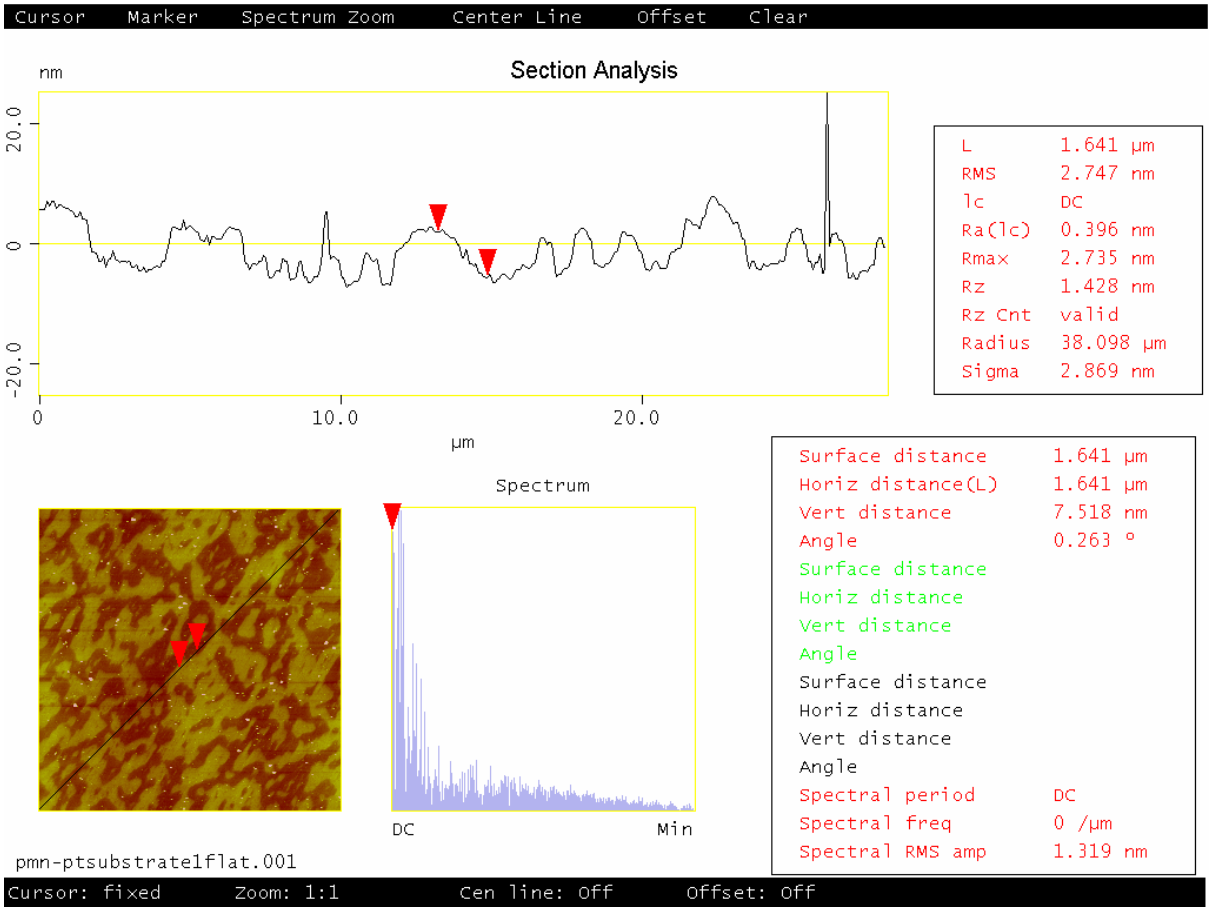

Fig.4.12 – AFM scan of polished PMN-PT single crystal.

Due to time constraints and problems during manufacture this device was not used however the manufacturing process was as follows:

1.) Aluminium electrodes were attached to a PMN-PT single crystal using gold-filled epoxy. The dimensions of the PMN-PT were 10mm x 10mm x 1mm and the dimensions of the electrodes were 10mm x 10mm x 4.5mm.
2.) The device was ground down to a thickness of 1mm making it a suitable thickness for use in EBL. This was done first with a rough grit sandpaper for speed and then with a fine grit to smooth off the surface.
3.) The sample was cleaned in an ultra-sonic bath using first acetone then iso-propanol then bonded to a 10mm x 10mm section of silicon wafer using epoxy.
4.) The device was mounted onto a metal cylinder using wax on the base of the wafer and briefly ground using very fine grit sand paper to level the top surface with the bottom surface.
5.) The sample was removed then cleaned again in acetone followed by iso-propanol ready to be mounted for polishing. To ensure that the sample could be removed from a cold epoxy mount it was first mounted in PMMA. To achieve this a glass slide was coated in Buehler release agent and the sample placed onto the slide PMN-PT side down. Sufficient PMMA was then applied to the substrate to fully coat the back and sides.
6.) Once the PMMA had set the substrate was removed from the slide and cold mounted in epoxy with the PMMA side down.
7.) The substrate was then polished in stages using diamond suspensions of decreasing grit size 6µm, 3µm and 1µm. Each stage was performed for 30 minutes using an Automet automatic polishing wheel set to counter-rotate. The sample had to be cleaned well after each stage to prevent diamond particles from previous stages contaminating later stages. The surface was inspected using optical microscopy after each stage to determine whether extra time was necessary. The finish could be refined further using colloidal silica.

8.) The polished substrate was then removed from the epoxy mount by dissolving the PMMA in acetone then cleaned using iso-propanol.

9.) A layer of HSQ was applied to the surface of the substrate by spin coating. The stages described from this point on are the steps necessary to prepare the substrate for EBL.

10.) The HSQ surface was primed by dehydrating with hexamethyldisiloxane (HMDS). The HMDS was applied by spin coating then baked a 120°C for 2 min. The sample was then cleaned in iso-propanol to remove any excess HMDS.

11.) PMMA resist was applied by spin coating and baked at 180°C for 5 min to evaporate the solvent in the resist.

12.) 15nm of aluminum was deposited onto the surface of the resist by evaporation in order to prevent charge build up during EBL which could cause displacements in the PMN-PT damaging the quality of the final resist.

4.8 - References

[1] Spaldin N., 2003, Magnetic Materials Fundamentals and Applications, Cambridge University Press

[2] H.Kronmeller and M.Faehnle, Micromagnetism and the Microstructure of Ferromagnetic Solids, 2003, Cambridge University Press

[3] Kronmüller H. and Fähnle M., Micromagnetism and the Microstructure of Ferromagnetic Solids, 2003, Cambridge University Press

[4] http://www.eng.utah.edu/~cs6220/HandBook.pdf

[5] http://suessco.com/en/simulations/solutions/femme-software/

[6] http://gid.cimne.upc.es/

[7] http://www.paraview.org/

[8] A. Vansteenkiste, *AIP Advances*, **4**, 107133 (2014)

5 - Uniaxial Stress Applied to Magnetostrictive Rings

Much work has been done on the control of domain walls in magnetic nanowires due to potential applications in magnetic memory [1][3]. Much of this work has focussed on the use of applied magnetic field to drive the domain walls through the wire[2], applied current to drive the domain walls through the wire [3] and artificial defects such as notches to 'pin' domain walls in place [4][5]. Recently it has been proposed that anisotropy gradients in a magnetic nanowire could both drive a domain wall through the wire and create pinning sites in the wire due to the energy landscape created by an anisotropy gradient [5]. It was suggested that the anisotropy gradient could be controlled using an artificial multiferroic system to induce magnetic anisotropy using strain [5].

In this chapter a simple system is introduced and characterised theoretically for observing the effect of an anisotropy gradient on domain walls. Preliminary experimental results are also presented. The operating principle of ferromagnetically soft, magnetostrictive ring structures on a piezoelectric substrate is as follows. Magnetic fields are used to initialise rings into the onion state (see §3.2). Voltage applied across the piezoelectric substrate will induce a strain, which is coupled to the rings. This uniaxial strain will create a uniaxial magnetic anisotropy in the rings. A rotating in-plane magnetic field could then be applied to drive the domain walls around the rings. However, the detailed trajectory of the domain walls would result from a combination of sample constraints (material, geometry), applied magnetic field and strain-induced uniaxial magnetic anisotropy. A schematic showing this experiment is shown in Fig.5.1.

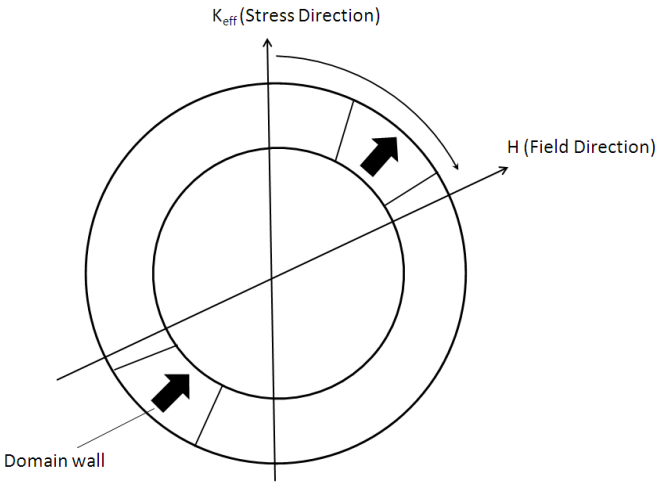

Fig.5.1 – Schematic showing the key features of magnetostrictive rings in a rotating field.

This experiment has a number of advantages. The ring can be thought of as being similar in behaviour to a straight wire in that the cross section of the wire forming the ring is identical to that of a straight wire and the domain walls in the ring can be driven along this wire. The fact that it is curved means that the uniaxial anisotropy is applied at a varying angle compared to the magnetisation direction of the domain wall as it travels around the wire. Because of this the domain walls will experience the uniaxial strain as a strain gradient in the wire with strain components along and transverse to the wire radius changing continuously. This uniform stress is much easier to achieve than the more complex stress gradients which would need to be applied in experiments using straight wires.

The use of the rotating field in addition to the applied stress makes it much easier to control the domain walls than using stress alone since the rotating field creates a well-defined response with the domain walls tracking the applied field direction. The applied anisotropy is expected to perturb this response. The experiment should be compatible with MOKE measurements, as with previous studies of rings [6], in order to see the effect that the applied anisotropy has in perturbing the domain walls.

The ring itself is a convenient structure to use as it can be easily initialised to contain the domain walls required for this experiment.

Having outlined the basic design of the experiment this chapter will describe results obtained from finite element and analytical modelling which have been analysed in order to inform the design of the experiment to maximise the effect of anisotropy and predict experimental results.

5.1 - Analytical Ring Model

5.1.1 - Design of Model

In order to gain insight into the ways uniaxial anisotropy will affect the domain walls present in the onion state of magnetic nanorings an analytical model was developed based on finding energy minima for the system.

In order to develop the model assumptions were made regarding the shape and magnetisation state of the ring. Firstly the ring is assumed to be perfectly circular. The magnetisation in each of the two onion state domains is assumed to follow the curve of the ring perfectly due to the strong shape anisotropy of the structure and the assumption that a soft magnetic material has been used. The domain walls are assumed to be transverse both due to small wire dimensions of the ring and the nature of the onion state. It is also assumed that the domain walls always lie directly opposite each other. The magnetic moments in the domain walls are assumed to be perpendicular to the edge of the ring at their centres and vary linearly to be parallel to the edge of the ring at their boundaries. The variation of the magnetisation in transverse domain walls can be modelled more accurately

using a tanh function however this was not possible for this analytical model as the anisotropy energy is non-integrable using this definition. Finally it is assumed that the applied anisotropy and magnetic field do not affect the structure of the domain walls. The ring and magnetisation state are shown schematically in Fig.5.2.

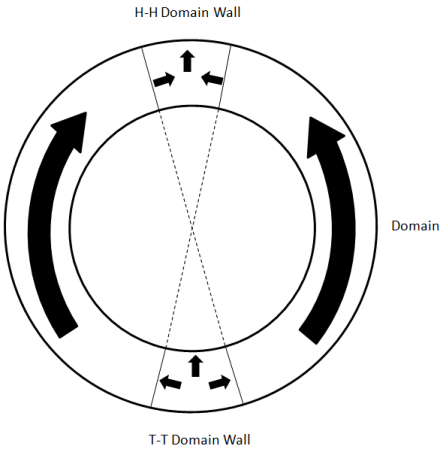

Fig.5.2 – Ring shape and magnetisation state.

The assumptions that the ring is perfectly circular means that results from this model will be most applicable if the quality of electron beam lithography and thin film deposition used to produce the rings is high. The assumption that the domain walls will always lie opposite each other is also most realistic for high quality rings as any edge roughness may pin the domain walls as they move through the ring breaking this symmetry. The assumption that the magnetisation in the domains follows the curve of the ring perfectly is most applicable in very soft magnetic materials and when low anisotropy is applied using stress, it is also more applicable when the shape anisotropy of the system is high which is achieved at higher ring radius and lower wire thickness and width. The assumption that the structure of the domains and domain walls are not affected by applied magnetic field and anisotropy mean that the model is most applicable when the applied field and anisotropy are low.

The dimensions of the ring are shown in Fig.5.3 with r representing the central ring radius, w the wire width, πΔ the domain wall width, t the wire thickness and Ψ an angular measurement of position within the ring with 0° chosen to be at the bottom of the ring. Domain wall width is measured at the midpoint of the wire for a more realistic representation and so the effective radius is measured from the centre of the ring to the midpoint of the wire. The central ring radius is used as the definition used for the domain wall is most suitable for the centre line of a magnetic nanowire. Note that factors of π are not removed when the value π is part of the term πΔ (the domain wall width) as the assumption is made that πΔ=w for the purposes of generating data from the completed model.

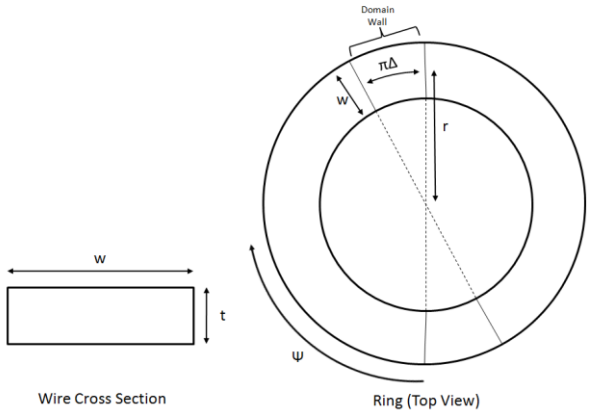

Fig.5.3 – Ring diagram with dimensions.

The high shape anisotropy of the ring is assumed to dictate the magnetisation state in the ring and so it has been assumed that the structures of the domains and domain walls will not change either due to application of field, anisotropy or change of position within the ring, note that these assumptions are most accurate at low field and applied anisotropy. With this assumption the calculated magnetostatic energy and exchange energy will remain constant as the domain walls move around the ring and so will be excluded from the model.

The two energies that will be calculated are the anisotropy energy (E_U) and the Zeeman energy (E_Z). E_U takes the form

$$E_U = K_u sin^2\theta \tag{5.1}$$

where K_u is a uniaxial anisotropy and θ is the angle between K_u and the direction of magnetisation. E_Z takes the form

$$E_Z = -\mu_0 mHcos\theta' \tag{5.2}$$

where μ_0 is the permeability of free space, m is a magnetic moment, H is the applied magnetic field and θ' is the angle between the magnetic moment and the magnetic field. In order to simplify the Zeeman term the magnetisation in the whole ring is averaged to a single effective magnetic moment $\bar{\boldsymbol{m}}$. Due to the symmetry of the system the centres of the domain walls will lie in the magnetisation direction of the averaged magnetic moment $\bar{\boldsymbol{m}}$. This simplified geometry is shown in Fig.5.4. K_{app} represents an applied uniaxial anisotropy and is used as a reference axis. Φ is the angle between K_{app} and $\bar{\boldsymbol{m}}$, Φ' is the angle between K_{app} and H. θ' is the angle between $\bar{\boldsymbol{m}}$ and H. Note that θ'=Φ'-Φ.

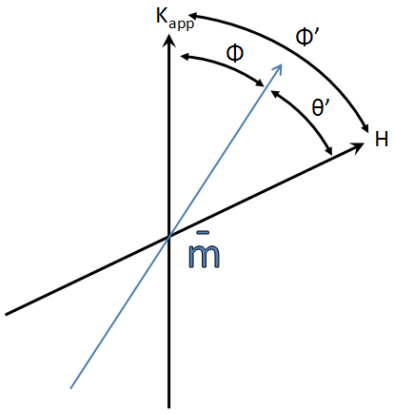

Fig.5.4 – Geometry used in Zeeman energy calculation.

Using this simplification the Zeeman energy of the ring system can be written as:

$$E_Z = -\mu_0 \bar{\boldsymbol{m}}.Hcos(\emptyset' - \emptyset) \tag{5.3}$$

Using this form requires that $\bar{\boldsymbol{m}}$ be calculated. First the average moment for a *single domain* ($\bar{\boldsymbol{m}}_{\mathbf{D}}$) between the domain walls will be calculated. Fig.5.5 shows the geometry used for this calculation.

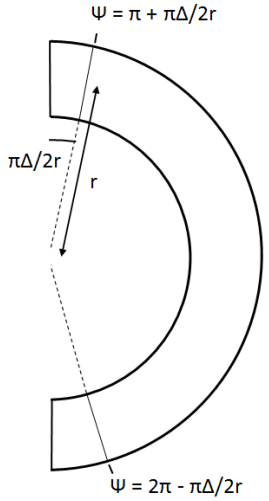

Fig.5.5 – Geometry for calculation of magnetisation in rings, $\bar{\boldsymbol{m}}_{\mathbf{D}}$.

The average moment is found by integrating the magnetisation in the domain. The limits for these integrals defined by the onset of the domain walls are shown in Fig.5.5 and are dependent on both the width of the domain walls and radius of the ring. The domain walls are aligned with the reference axis K_{app} for the purposes of this calculation and so the local magnetisation component in the K_{app} direction in this domain is:

$$m_D = -m_s sin\,\Psi$$

$$\bar{m}_D = m_s \frac{\int_{\pi+\frac{\pi\Delta}{2r}}^{2\pi-\frac{\pi\Delta}{2r}} -sin\Psi \; d\Psi}{\int_{\pi+\frac{\pi\Delta}{2r}}^{2\pi-\frac{\pi\Delta}{2r}} d\Psi} \tag{5.4}$$

$$\bar{m}_D = m_s \left(\frac{2cos\frac{\pi\Delta}{2r}}{\pi-\frac{\pi\Delta}{r}} \right) \tag{4.5}$$

Due to the symmetry of the system the average moment of the second domain is also equal to $\bar{\boldsymbol{m}}_{\mathbf{D}}$.

In order to calculate the average moment in each of the domain walls the magnetic structure of the domain walls must be defined. The geometry used for this is shown in Fig.5.6.

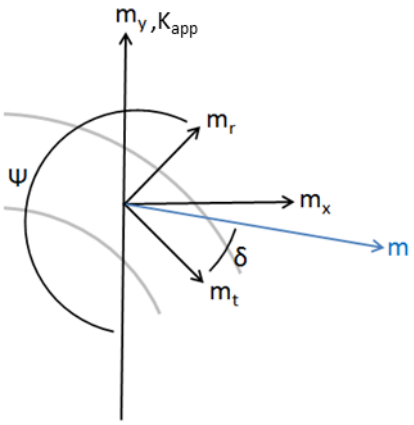

Fig.5.6 – Geometry used to define structure of domain walls. The anisotropy direction K_{app} is defined as the y axis. m_y= magnetisation in the y direction, m_x magnetisation in the x direction. m_t=magnetisation tangential to the ring and m_r=magnetisation radial to the ring. δ=angle between the local magnetisation direction (m) and the m_t direction.

The anisotropy direction K_{app} is defined as the y axis. The magnetisation in the y direction is defined as m_y and the in plane magnetisation perpendicular to this is defined as m_x. The values m_t and m_r are the tangential and radial magnetisations to the ring, respectively. The angle δ is the angle between the local magnetisation direction (**m**) and the m_t direction. Note that in the domains the angle δ is always zero while in the domain walls δ varies linearly with Ψ (position around ring) across the wall width. In order to find the magnetic moment of a domain wall m_y must be integrated over the range of Ψ for the domain wall. The local value of m_y can be calculated as:

$$m_y(\Psi) = sin(\Psi - \delta) \tag{5.6}$$

For a head-to-head (H-H) domain wall the angle δ is defined as:

$$\delta = \frac{\pi r\left(-q+\frac{\pi\Delta}{2r}+\Psi\right)}{\pi\Delta} \tag{5.7}$$

where q is the value of Ψ at the centre of the domain wall. For a tail-to-tail (T-T) domain wall, with the same absolute direction of magnetisation as the head-to-head wall and opposite chirality, the angle δ is defined as:

$$\delta = \frac{\pi r\left(q+\frac{\pi\Delta}{2r}-\Psi\right)}{\pi\Delta} \tag{5.8}$$

In order that the domain walls are aligned with the y axis for this calculation q is equal to π for the H-H domain wall and equal to zero for the T-T domain wall.

By substituting Eqn.5.7 into Eqn.5.6 and integrating over the range of Ψ for the H-H domain wall the average moment for this domain wall ($\bar{\boldsymbol{m}}_{\mathbf{H}}$) can be calculated as:

$$\bar{m}_H = m_s \frac{\int_{\pi-\frac{\pi\Delta}{2r}}^{\pi+\frac{\pi\Delta}{2r}} m_y \, d\Psi}{\int_{\pi-\frac{\pi\Delta}{2r}}^{\pi+\frac{\pi\Delta}{2r}} d\Psi} \tag{5.9}$$

$$\bar{m}_H = -m_s \frac{2r \, cos\frac{\pi\Delta}{2r}}{\pi\Delta - \pi r} \tag{5.10}$$

Similarly by substituting Eqn.5.8 into Eqn.5.6 and integrating over the range of Ψ for the T-T domain wall the average moment for this domain wall ($\bar{\boldsymbol{m}}_{\mathbf{T}}$) can be calculated as:

$$\bar{m}_T = m_s \frac{\int_{-\frac{\pi\Delta}{2r}}^{\frac{\pi\Delta}{2r}} m_y \, d\Psi}{\int_{-\frac{\pi\Delta}{2r}}^{\frac{\pi\Delta}{2r}} d\Psi} \tag{5.11}$$

$$\bar{m}_T = -m_s \frac{2r \, cos\frac{\pi\Delta}{2r}}{\pi\Delta + \pi r} \tag{5.12}$$

The value of $\bar{\boldsymbol{m}}$ can then be calculated by multiplying each of $\bar{\boldsymbol{m}}_{\mathbf{D}}$, $\bar{\boldsymbol{m}}_{\mathbf{H}}$ and $\bar{\boldsymbol{m}}_{\mathbf{T}}$ by the proportion of the ring taken up by the domains, H-H wall and T-T wall respectively and summing each as shown in Eqn.5.13 and Eqn.5.14.

$$\bar{m} = \frac{\pi r - \pi\Delta}{\pi r}\bar{m}_D + \frac{\pi\Delta}{\pi r}\bar{m}_H + \frac{\pi\Delta}{\pi r}\bar{m}_T$$

$$= \frac{2m_s}{\pi} \, cos\left(\frac{\pi\Delta}{2r}\right)\left[1 + \frac{\pi\Delta}{\pi r - \pi\Delta} - \frac{\pi\Delta}{\pi r + \pi\Delta}\right] \tag{5.14}$$

By using the value $\bar{\boldsymbol{m}}$ the Zeeman energy can be calculated by integrating the energy of this average moment (as defined in Eqn.5.3) over the volume of the ring:

$$E_Z = \int_0^{2\pi rwt} -\mu_0 \bar{m} H \cos(\Phi' - \Phi)\, dV \tag{5.15}$$

$$E_Z = -2\pi rwt \mu_0 \bar{m} H \cos(\Phi' - \Phi) \tag{5.16}$$

For the anisotropy energy calculations the domains and domain walls must be defined with respect to the fixed axis K_{app}. The angle Φ is the angle between K_{app} and the centre of the H-H domain wall. Thus the geometry used to calculate the anisotropy energy is shown in Fig.5.7.

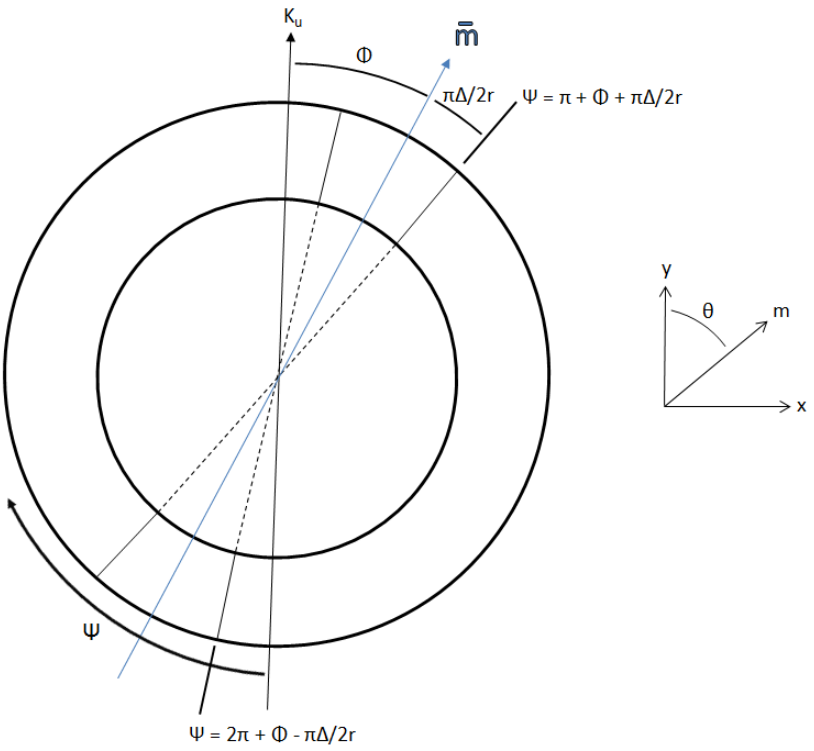

Fig.5.7 – Geometry used in anisotropy energy calculations.

First the anisotropy energy of a domain can be calculated simply by integrating Eqn.5.1 over the volume of the domain (V_d). The value of θ in the right hand domain is equal to Ψ-π/2. Since the integration is over the domain volume and the energy is in terms of Ψ, dV_d can be converted to dΨ in the integration by:

$$dV_d = 2\pi rwt\, d\Psi \tag{5.17}$$

Due to the symmetry of the ring the anisotropy energy of the two domains is equal and so the energy of both domains ($E_{U,D}$) can be calculated by doubling the energy of one domain. Therefore the combined energy of both domains is:

$$E_{U,D} = 4\pi rwt \int_{\pi+\Phi+\frac{\pi\Delta}{2r}}^{2\pi+\Phi-\frac{\pi\Delta}{2r}} K_U\, cos^2\Psi\, d\Psi \tag{5.18}$$

$$E_{U,D} = -2\pi rwtK_U \left(\frac{r\, cos2\emptyset\, sin\frac{\pi\Delta}{r} - \pi r - \pi\Delta}{r} \right) \tag{5.19}$$

In order to calculate the energies of the domain walls the angle θ is equal to Ψ-δ-π/2. When calculating δ for the H-H domain wall using Eqn.5.7 the value q is equal to π+Φ. When calculating δ for the T-T domain wall using Eqn.5.8 the value q is equal to Φ.

The anisotropy energy of the H-H domain wall ($E_{U,H}$) then becomes:

$$E_{U,H} = 2\pi rwt \int_{\pi+\Phi-\frac{\pi\Delta}{2r}}^{\pi+\Phi+\frac{\pi\Delta}{2r}} K_U\, cos^2(\delta - \Psi)\, d\Psi \tag{5.20}$$

$$E_{U,H} = 2\pi rwtK_U \left(\frac{(\pi\Delta)^2 - \pi r\pi\Delta + r\pi\Delta\, sin\frac{\pi\Delta}{r} cos2\Phi}{2r\pi\Delta - 2\pi r^2} \right) \tag{5.21}$$

The anisotropy energy of the T-T domain wall ($E_{U,T}$) is:

$$E_{U,T} = 2\pi rwt \int_{\Phi-\frac{\pi\Delta}{2r}}^{\Phi+\frac{\pi\Delta}{2r}} K_U \cos^2(\delta - \Psi)\, d\Psi \tag{5.22}$$

$$E_{U,T} = 2\pi rwtK_U \left(\frac{(\pi\Delta)^2 + \pi r\pi\Delta + r\pi\Delta \sin\frac{\pi\Delta}{r} \cos 2\Phi}{2r\pi\Delta + 2\pi r^2} \right) \tag{5.23}$$

Taking the sum of E_Z, $E_{U,D}$, $E_{U,H}$ and $E_{U,T}$ the total energy of the system is:

$$E = 2\pi rwtK_U \left(\frac{(\pi\Delta)^2 - \pi r\pi\Delta + r\pi\Delta \sin\frac{\pi\Delta}{r} \cos 2\Phi}{2r\pi\Delta - 2\pi r^2} + \frac{(\pi\Delta)^2 + \pi r\pi\Delta + r\pi\Delta \sin\frac{\pi\Delta}{r} \cos 2\Phi}{2r\pi\Delta + 2\pi r^2} - \frac{r\cos 2\emptyset \sin\frac{\pi\Delta}{r} - \pi r - \pi\Delta}{r} \right) - \mu_0 \bar{m} H 2\pi rwt \cos(\Phi' - \Phi) \tag{5.24}$$

In order to find the equilibrium domain wall positions the minima of Eqn.5.24 with respect to Φ must be found. Differentiating Eqn.5.24 and setting $\frac{dE}{d\Phi} = 0$ yields:

$$2\pi rwtK_U \left(\frac{2\pi^2 r^2 \sin 2\Phi \sin\frac{\pi\Delta}{r}}{\pi^2 r^2 - (\pi\Delta)^2} \right) = -\mu_0 \bar{m} 2\pi rwtH \sin(\Phi - \Phi') \tag{5.25}$$

Eqn.5.25 cannot be solved analytically so the Newton-Raphson method is used. The Newton-Raphson iterative formula becomes:

$$\Phi_1 = \Phi_0 + \frac{H\mu_0\bar{m}\pi^2 r^2 \sin(\Phi' - \Phi_0) - H\mu_0\bar{m}(\pi\Delta)^2 \sin(\Phi' - \Phi_0) - 2\pi^2 K_U r^2 \sin 2\Phi_0 \sin\frac{\pi\Delta}{r}}{H\mu_0\bar{m}\pi^2 r^2 \cos(\Phi' - \Phi_0) - H\mu_0\bar{m}(\pi\Delta)^2 \cos(\Phi\prime - \Phi_0) + 4\pi^2 K_U r^2 \cos 2\Phi_0 \sin\frac{\pi\Delta}{r}} \tag{5.26}$$

where Φ_0 is an initial chosen value that is used to calculate Φ_1. The calculated Φ_1 becomes the new Φ_0 in the next iteration of the formula. By iterating the formula the calculated Φ_1 values quickly converge on a solution to Eqn.5.25 with each iteration bringing the calculated Φ_1 closer to the exact solution. It should be noted that for an equation such as Eqn.5.25 which has many solutions it is important to pick initial Φ_0 values which will converge on the solutions which properly describe the physical behaviour being modelled provided an appropriate initial value. An appropriate initial value can be ensured using the threshold conditions described later in this chapter.

Most materials have an intrinsic anisotropy which may include crystalline and stress contributions. In thin film materials this anisotropy is generally an in plane anisotropy and so can be represented as a second anisotropy K_{int} in addition to K_U which lies at an angle X from the applied anisotropy. In order to calculate domain wall positions the anisotropies K_{int} and K_U are resolved into a single effective anisotropy K_{eff}.

$$K_{eff} = K_U cos\delta + K_{int} cos(X - d) \tag{5.27}$$

Where:

$$d = \tan^{-1} \frac{K_{int} \sin X}{K_U + K_{int} \cos X} \tag{5.28}$$

When using an intrinsic anisotropy K_{eff} replaces K_U in the calculation of domain wall positions. The angles Φ and Φ' are replaced by the angles Φ_d and Φ_d' (shown in Fig.5.1) respectively.

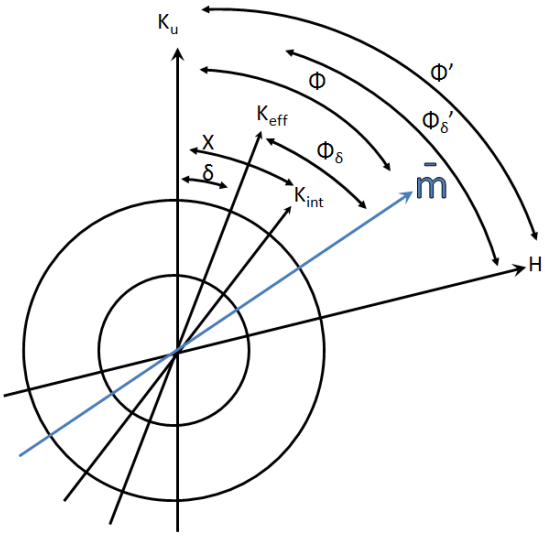

Fig.5.8 – Geometry used in simulation including intrinsic anisotropy K_{int}.

The domain wall position with respect to K_{eff} can therefore be found by solving Eqn.5.29 for Φ_d.

$$2\pi rwtK_{eff}\left(\frac{2\pi^2r^2\,sin2\emptyset_\delta\,sin\frac{\pi\Delta}{r}}{\pi^2r^2-(\pi\Delta)^2}\right)=-\mu_0\bar{m}2\pi rwtH\,sin(\emptyset_d-\emptyset_d{}') \tag{5.29}$$

Like Eqn.5.25, Eqn.5.29 cannot be solved analytically and so, again, the Newton-Raphson method is used.

Keeping K_U as being along the reference axis, the values Φ and Φ_d' are calculated as:

$$\emptyset=\emptyset_\delta+d \tag{5.30}$$

$$\emptyset'_\delta=\emptyset'-d \tag{5.31}$$

Using Eqn.5.29, Eqn.5.30 and Eqn.5.31 it is possible to calculate domain wall positions with respect to the applied anisotropy (Φ) for a magnetic field applied with respect to the

applied anisotropy (Φ') while taking into account the effect of a second in-plane intrinsic anisotropy.

Note that in this work the domain wall position is calculated based on the previous position of the domain wall, with the initial position of the domain wall always Φ=0°. This means that the domain wall may exist in a local energy minimum rather than the global energy minimum. This approach simulates the dynamic behaviour expected to occur experimentally. In order to accurately use the model in this way the initial value chosen for the Newton-Raphson iteration must converge on the correct energy minimum. To this end a more complete understanding of the model behaviour is required which will be detailed below.

5.1.2 - Model Results

Using the model developed in this chapter the influence of the parameters in Eq.5.29 on the motion of domain walls in magnetostrictive nanowires to be predicted. This is based on the assumption that the domain walls will follow the calculated energy minimum position. Experimentally it is expected that there will be some deviation from this due to phase lag caused by edge roughness as was shown by Negoita et al.[6]

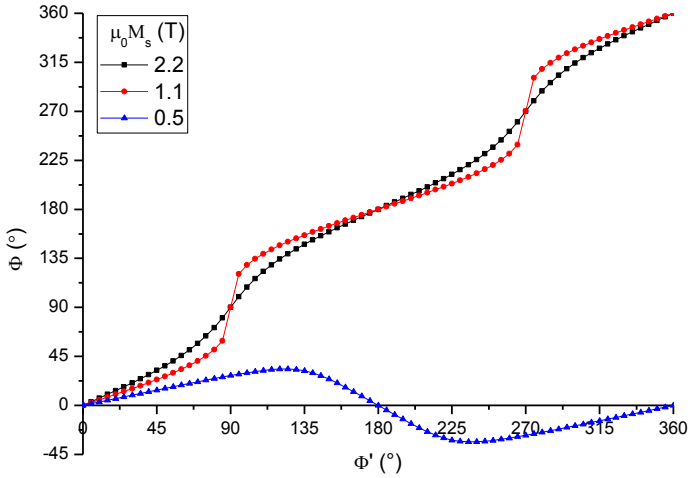

Fig.5.9 – Domain wall position (Φ) as a function of magnetic field angle (Φ') for various values of magnetic polarisation ($\mu_0 M_s$). r=1000 nm, w=100 nm, K_{eff}=2000 J/m^3, H=1.15 kA/m.

Fig.5.9 shows predictions of domain wall position (Φ) as a function of magnetic field angle (Φ') for various values of magnetic polarisation ($\mu_0 M_s$). The other variables in the model are fixed in order to show the effect of varying magnetic polarisation on the behaviour of the domain walls (r=1000 nm, w=100 nm, H=1.15 kA/m and the effective anisotropy K_{eff}=2000 J/m^3). For $\mu_0 M_s$=2.2 T the domain walls follow the applied field direction relatively closely. For $\mu_0 M_s$=1.1 T the domain wall position deviates further from the applied field direction. For $\mu_0 M_s$=0.5 T the domain wall position deviates strongly from the applied field direction and rather than rotating fully around the ring oscillates around the Φ=0° position. These results show that as $\mu_0 M_s$ increases the effect of the applied anisotropy decreases. This is due to the increased effect of magnetic field on materials with high magnetic polarisation.

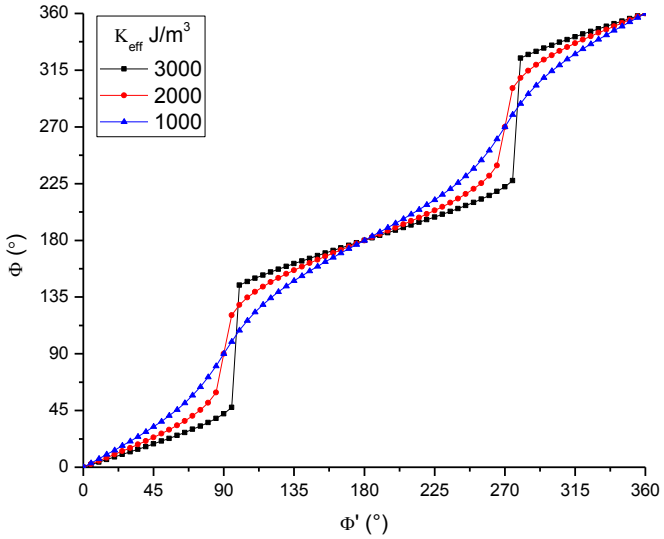

Fig.5.10 – Domain wall position (Φ) as a function of magnetic field angle (Φ') for various values of effective anisotropy (K_{eff}). r=1000 nm, w=100 nm, $\mu_0 M_s$=1.1 T, H=1.15 kA/m.

Fig.5.10 shows predictions of domain wall position (Φ) as a function of magnetic field angle (Φ') for various values of effective anisotropy (K_{eff}) and other terms constant (r=1000 nm, w=100 nm, H=1.15 kA/m and $\mu_0 M_s$=1.1 T). For K_{eff} =3000 J/m^3 the domain walls deviate strongly from the applied field direction but still rotate fully around the ring. A new behaviour is observed with two discontinuities in the plot showing sudden jumps in the energy minimum position as the field is rotated. For K_{eff} =2000 J/m^3 the domain wall position follows the applied field direction more closely and no discontinuities are present. K_{eff} =1000 J/m^3 the domain wall position follows the applied field direction more closely still. These results show that as K_{eff} increases the effect of the applied anisotropy increases.

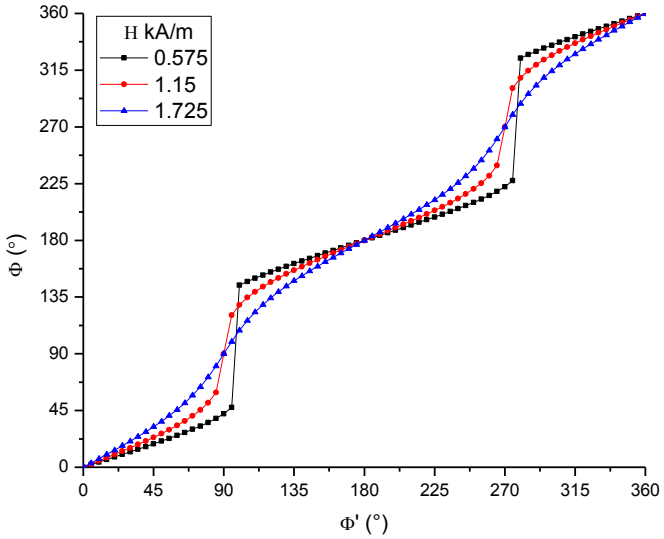

Fig.5.11 – Domain wall position (Φ) as a function of magnetic field angle (Φ') for various values of applied field (H). r=1000 nm, w=100 nm, $\mu_0 M_s$=1.1 T, K_{eff}=2000 J/m^3.

Fig.5.11 shows predictions of domain wall position (Φ) as a function of magnetic field angle (Φ') for various values of magnetic field (H), with other variables again fixed (r=1000 nm, w=100 nm, K_{eff}=2000 J/m^3 and $\mu_0 M_s$=1.1 T). For H=0.575 kA/m the domain walls deviate strongly from the applied field direction rotating fully round the ring with the same discontinuities shown in Fig.5.10. For H=1.15 kA/m the domain wall position follows the applied field direction more closely and no discontinuities are present. H=1.725 kA/m the domain wall position follows the applied field direction more closely still. These results show that as H increases the effect of the applied anisotropy decreases. Further it can be seen that the plots in Fig.5.11 are the same as those in Fig.5.10, this is because in this model doubling the applied field has the same effect as halving the effective anisotropy. A low edge roughness is expected to improve the ease of observing these differences as edge roughness results in a phase lag in the domain wall position[6].

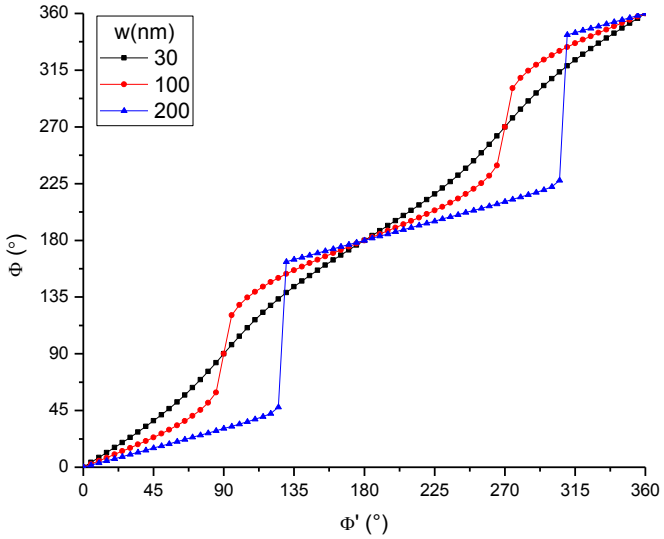

Fig.5.12 – Domain wall position (Φ) as a function of magnetic field angle (Φ') for various values of wire width (w). r=1000 nm, H=1.15 kA/m, $\mu_0 M_s$=1.1 T, K_{eff}=2000 J/m^3.

Fig.5.12 shows predictions of domain wall position (Φ) as a function of magnetic field angle (Φ') for various values of wire width (w; other values are r=1000 nm, K_{eff}=2000 J/m^3, H=1.15 kA/m and $\mu_0 M_s$=1.1 T). For w=30 nm the domain walls follow the applied field direction closely. For w=100 nm the domain wall position deviates more from the applied field direction. For w=200 nm the domain wall position deviates strongly from the applied field direction and once again discontinuities are seen. These results show that as w increases the effect of the applied anisotropy increases. This is because the domain walls interact stronger with the applied anisotropy than the domains and as w is increased the volume of the domain walls is increased with respect to the domains.

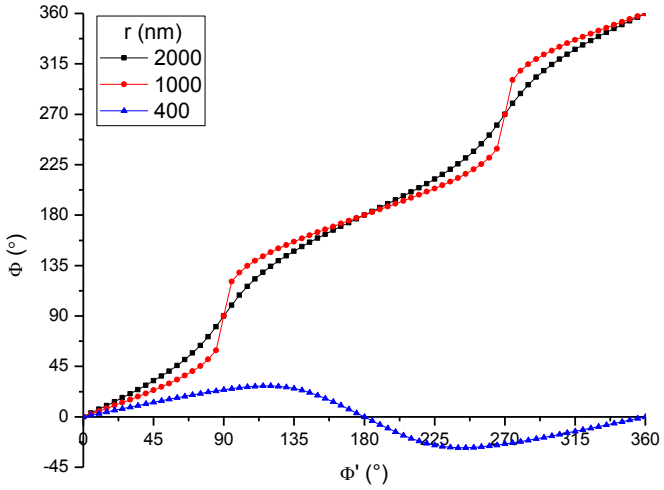

Fig.5.13 – Domain wall position (Φ) as a function of magnetic field angle (Φ') for various values of radius (r). w=100 nm, H=1.15 kA/m, $\mu_0 M_s$=1.1 T, K_{eff}=2000 J/m^3.

If the ring radius (r) is allowed to vary (Fig.5.13; w=100 nm, K_{eff}=2000 J/m^3, H=1.15 kA/m and $\mu_0 M_s$=1.1 T) similar dependence of domain wall position (Φ) on magnetic field angle (Φ') is seen again. This time, domain walls in the widest rings (r=2000 nm) follow the applied field direction most closely, while those in rings of intermediate width (r=1000 nm) deviate from this behaviour slightly. In narrow rings (r=400 nm) the domain walls do not track the rotating field and instead oscillate about the Φ=0° position, as was seen in Fig.5.9. Of course, the walls can be forced to track the field rotation again by increasing the field magnitude. These results show that as r increases the effect of the applied anisotropy decreases. This is because the domain walls interact much more strongly with the applied anisotropy than the domains due to their higher net magnetic moment and as r is increased the relative volume of the domain walls is decreased with respect to the domains.

Three distinct behaviours can be observed in Figs.5.8-5.13. The first, illustrated in Fig.5.14, is a smooth increase in Φ – i.e. the domain walls track the field rotation smoothly. The

second, shown in Fig.5.15, is of domain walls tracking the field rotation but with two discontinuities per field cycle. The third, shown in Fig.5.16, is a smooth oscillation of Φ about the Φ=0° axis, i.e. the walls do not rotate around the rings. Figures 5.14-5.16 also show schematic diagrams of the domain configurations at different parts of field cycle.

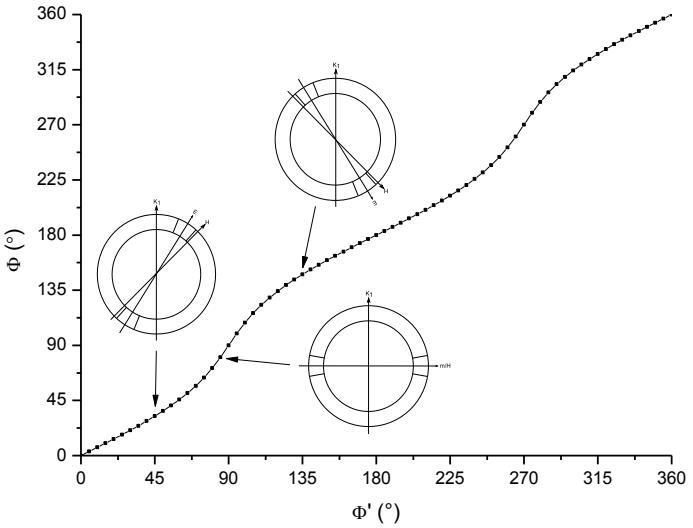

Fig.5.14 – Plot showing smooth tracking of domain wall position, Φ, with magnetic field angle, Φ'. Individual points are highlighted with diagrams of the modelled ring at those points highlighting the smooth transition through the point (90˚,90˚).

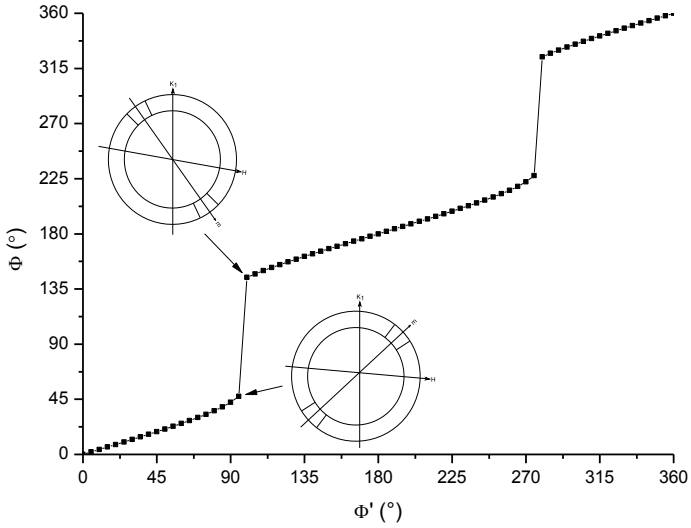

Fig.5.15 - Plot showing smooth increase in Φ with Φ’ with discontinuities. Individual points are highlighted with diagrams of the modelled ring at those points highlighting the discontinuity.

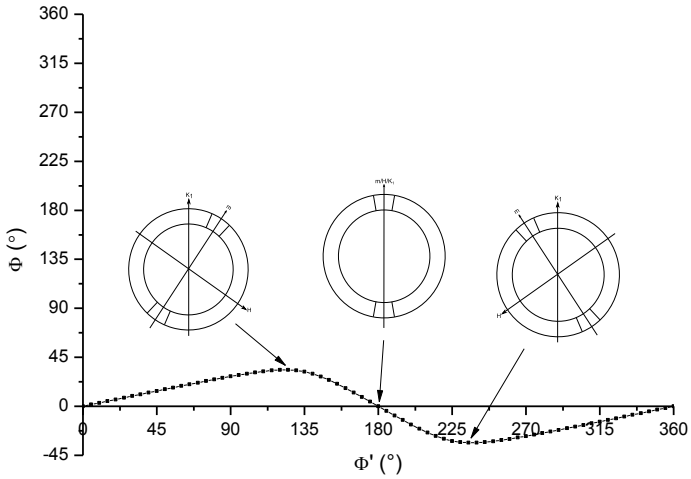

Fig.5.16 - Plot showing smooth a smooth oscillation around Φ=0°. Individual points are highlighted with diagrams of the modelled ring at those points highlighting the oscillation of the domain walls.

These behaviours can be understood more clearly by looking at the energy landscapes created by allowing the domain wall axis angle Φ to vary freely in any field angle Φ', and calculated using Eqn.5.24. All energy landscapes have been calculated using example values of r=2000 nm, w=300 nm, $\mu_0 M_s$=1.1 T and H=1.59 kA/m.

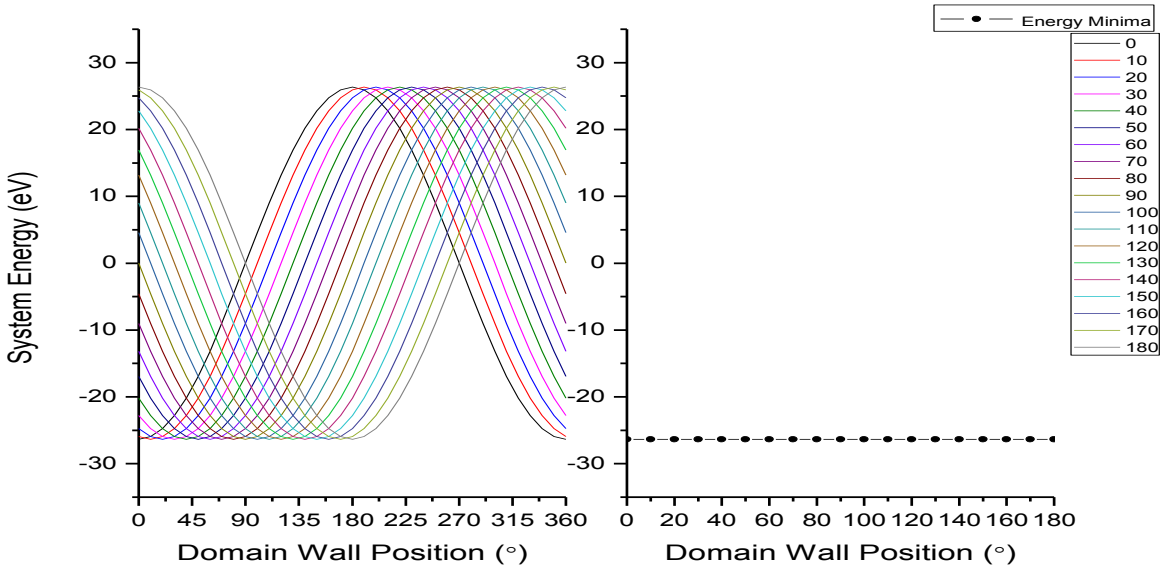

Fig.5.17 – Left: Energy landscapes for varying field angles. K_{eff}=0.001 J/m^3, r=2000 nm, w=300 nm, $\mu_0 M_s$=1.1 T, H=1.59 kA/m. Right: Plot of the energy minimum/local energy minimum occupied by the domain walls for each plotted field angle.

Fig.5.17 shows the energy landscapes of a ring with very low applied anisotropy of 0.001 J/m^3. The plot can be interpreted by viewing the domain wall position that gives an energy minimum for each field angle. The variation of the energy minimum position indicates the likely nature of the domain wall motion in a rotating field. The shape for low applied anisotropy in Fig. 5.17 shows energy minimum positions of $\Phi \approx \Phi'$, i.e. precise tracking of the field direction by the domain walls. This is expected when the Zeeman term is dominating and has been considered in non-magnetostrictive ring systems elsewhere [C].

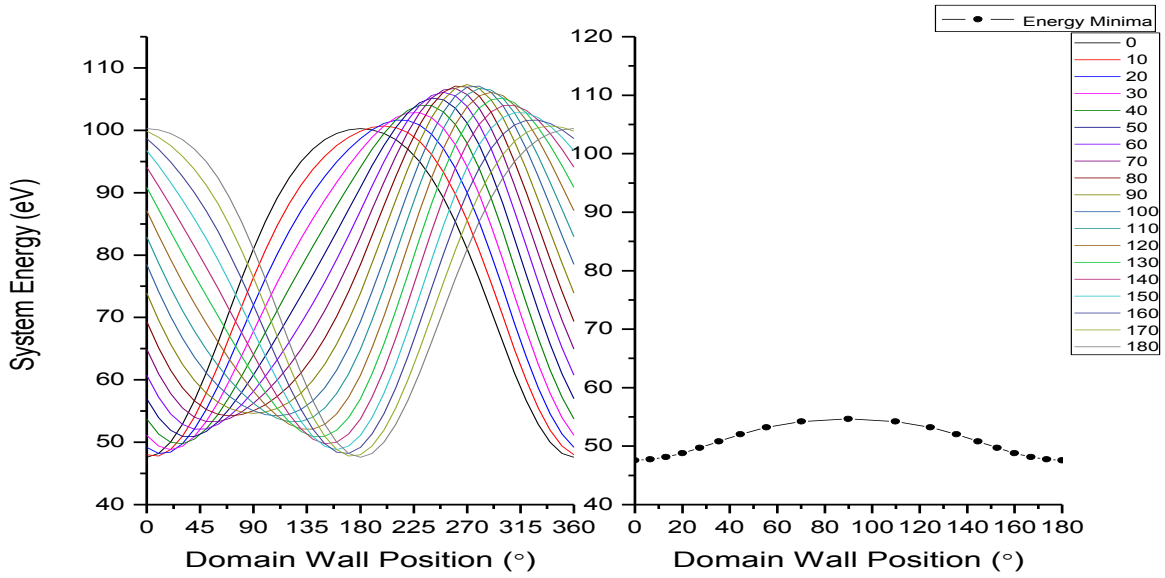

Fig.5.18 – Left: Energy landscapes for varying field angles. K_{eff}=1000 J/m^3, r=2000 nm, w=300 nm, $\mu_0 M_s$=1.1 T, H=1.59 kA/m. Right: Plot of the energy minimum/local energy minimum occupied by the domain walls for each plotted field angle.

At modest induced anisotropies of 1000 J/m^3 (Fig. 5.18) contribution of the anisotropy term distorts the energy landscape seen in Fig.5.17 to move all but one of the energy minima closer to the anisotropically favourable positions 0° and 180° (it should be noted that due to the ring geometry the 360° position is identical to the 0° position). Most importantly the energy minimum for Φ'=90° (field angle perpendicular to anisotropy direction) is located at Φ=90° (domain wall axis perpendicular to anisotropy direction).

Therefore it can be seen that at these relatively low anisotropies (or high fields) the domain walls will rotate fully around the ring as the field is rotated. This low anisotropy regime is characterised by a domain wall position of 90° when the field angle is 90° and a position of 180° when field angle is 180°. Due to the symmetry of the ring it can also be stated that the regime is also characterised by a domain wall position of 270° when the field angle is 270° and a position of 360° when field angle is 360°.

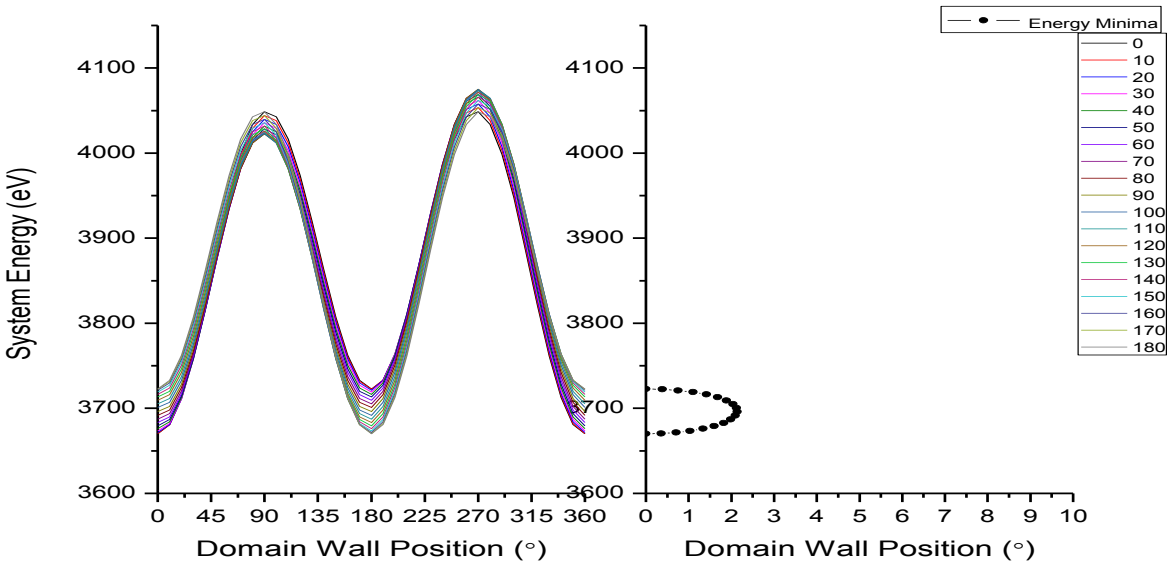

Fig.5.19 – Left: Energy landscapes for varying field angles. K_{eff}=50 kJ/m^3, r=2000 nm, w=300 nm, $\mu_0 M_s$=1.1 T, H=1.59 kA/m. Right: Plot of the energy minimum/local energy minimum occupied by the domain walls for each plotted field angle showing that the domain wall does not move around the ring.

Fig.5.19 shows the effect of a very high induced anisotropy of 50 kJ/m^3. The energy landscape fits closely to a $\cos^2\Phi$ function indicating that the anisotropy term is dominating. The Zeeman contribution distorts the energy landscape only by a small amount moving the energy minima closer to the field direction. It can be seen that the energy minima are clustered near to Φ=0°, Φ=180° and Φ=360° which corresponds to the axis of the applied anisotropy. There are two energy minima for each field direction (since Φ=0° is equivalent to Φ=360°) which are centred around Φ=0° and Φ=180°. The energy barriers between these two possible positions are very high meaning that a domain wall in the energy minimum centred around Φ=0° would not have sufficient energy to move to the minimum centred around Φ=180°. It can be seen from the energy minima that as the field angle is increased a domain wall starting at Φ=0° will move away from 0° reaching a maximum at Φ'=90° then

retrace its path back reaching Φ=0° when Φ=180°. The differences in the absolute value of system energy at energy minimum positions is due to oppositely signed Zeeman energies for the opposite arrangements of magnetisation in the ring relative to the applied magnetic field.

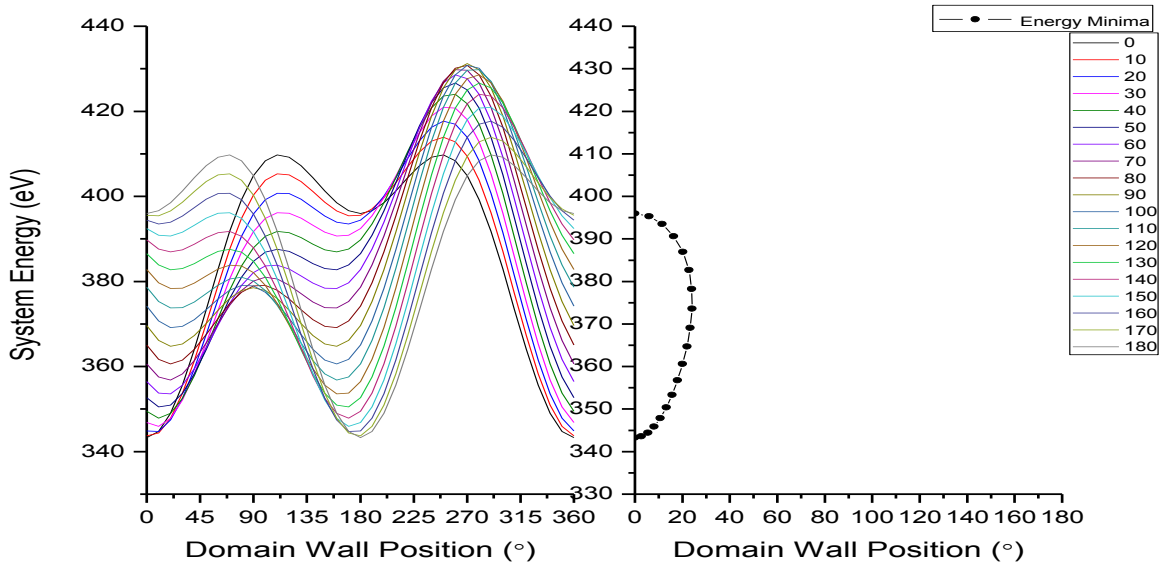

Fig.5.20 – Left: Energy landscapes for varying field angles. K_{eff}=5000 J/m^3, r=2000 nm, w=300 nm, $\mu_0 M_s$=1.1 T, H=1.59 kA/m. Right: Plot of the energy minimum/local energy minimum occupied by the domain walls for each plotted field angle showing that the domain wall does not move around the ring.

Fig.5.20 shows the effect of a moderately high anisotropy of 5000 J/m^3. The influence of the $\cos^2\Phi$ function of the anisotropy term can clearly be seen as a distortion of the Zeeman term. Though the influence of the Zeeman term is easier to see the same behaviour as in Fig.5.19 can be observed in Fig.5.20. However the energy minima as the field rotates are located further from Φ=0° and Φ=180° due to the lower relative contribution of the anisotropy energy and will result in the oscillation of domain wall position as the field rotates shown in Fig. 5.16.

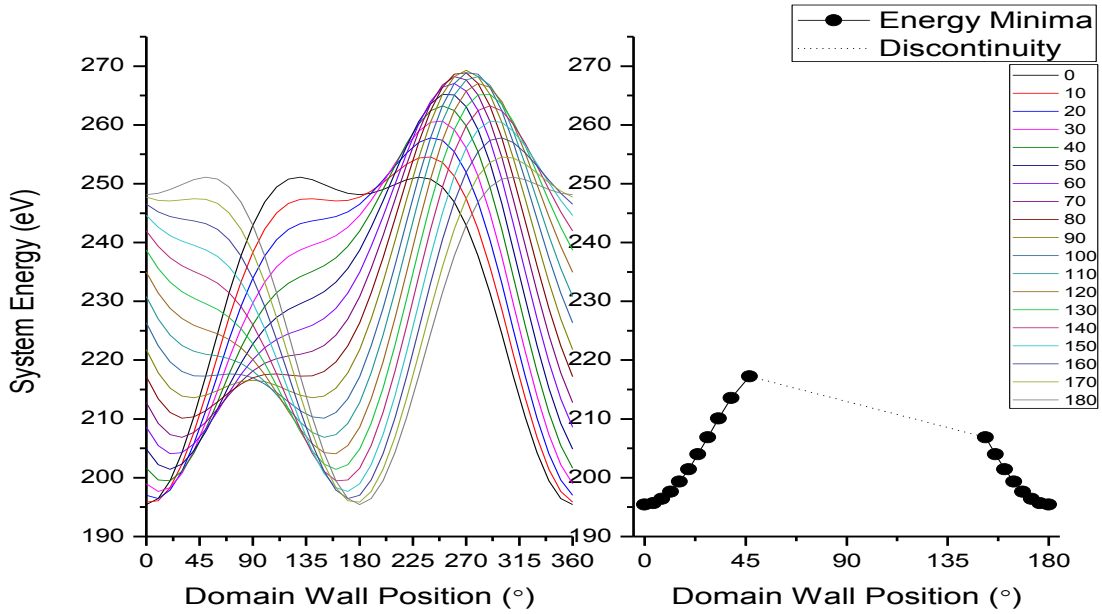

Fig.5.21 – Left: Energy landscapes for varying field angles. K_{eff}=3000 J/m^3, r=2000 nm, w=300 nm, $\mu_0 M_s$=1.1 T, H=1.59 kA/m. Right: Plot of the energy minimum/local energy minimum occupied by the domain walls for each plotted field angle with the discontinuity shown as a dotted line.

Fig.5.21 shows the effect of a more moderate anisotropy. The energy landscape is similar to that of Fig.5.20, however the effect of the anisotropy is not sufficient to provide energy minima below Φ=90° for all of the curves. Crucially however it can be seen that energy minima exist for Φ' greater than 90°. Looking at the curves for Φ' (field angle) =110° with its minima below Φ=90° and for Φ'=120° with its minima above Φ=90° it can be seen that a domain wall following these positions in the energy landscape would experience the discontinuity characteristic of the intermediate regimen (e.g. Fig. 5.15).

This shows more clearly how the three distinct regimens of domain walls interacting with an in-plane rotating field depend on how strongly the anisotropy affects the domain walls in comparison to the field:

Regimen 1: Low anisotropy. Domain walls move continuously around the ring.

Regimen 2: Intermediate anisotropy. Domain walls move around the ring with discontinuities.

Regimen 3: High anisotropy. Domain walls cannot move fully around the ring.

In order to calculate the range of regimen 1 the minimum anisotropy that allows the domain walls to reach Ø=90° when Ø'=90° must be calculated. Regimen 1 holds if no energy minimum exists in the range 0°≤Ø<90° when Ø'=90°. The threshold condition for this is a point of inflection in the function $\frac{dE}{d\emptyset}$ at Ø'=90°. This is shown graphically in Fig.5.22 and can be calculated as:

$$\frac{dE_{Z'}}{d\prime\emptyset} = \frac{dE_{U'}}{d\prime\emptyset} \text{ for } \emptyset = 90° \text{ and } \emptyset' = 90° \tag{5.31}$$

Substituting the specified values of Ø and Ø' the threshold anisotropy for regimen 2 ($K_{u,t2}$) can be calculated as:

$$K_{U,t2} = H\frac{\mu_0 \bar{m}(\pi^2 r^2 - (\pi\Delta)^2)}{4\pi^2 r^2 sin\left(\frac{\pi\Delta}{r}\right)} \tag{5.32}$$

In order to calculate the range of regimen 2 the maximum anisotropy that allows full rotation of the domain walls must be calculated. The maximum energy barrier due to anisotropy occurs at Ø=45°. The maximum driving force due to applied field occurs at Ø'=135°. Therefore the threshold condition for regimen 2 is:

$$\frac{dE_Z}{d\emptyset} = \frac{dE_U}{d\emptyset} \text{ for } \emptyset = 45° \text{ and } \emptyset' = 135° \tag{5.33}$$

When this condition is met an energy minimum occurs at Ø=45° and the domain walls will not rotate fully around the ring. This is shown graphically in Fig.5.23. Substituting the specified values of Ø and Ø' the threshold anisotropy for regimen 3 ($K_{u,t3}$) can be calculated as:

$$K_{U,t3} = H\frac{\mu_0 \bar{m}(\pi^2 r^2 - (\pi\Delta)^2)}{2\pi^2 r^2 sin\left(\frac{\pi\Delta}{r}\right)} \tag{5.34}$$

Since $K_{U,t3} = 2K_{U,t2}$ it is simpler to refer to a single threshold anisotropy ($K_{u,t}$) equal to $K_{u,t2}$.

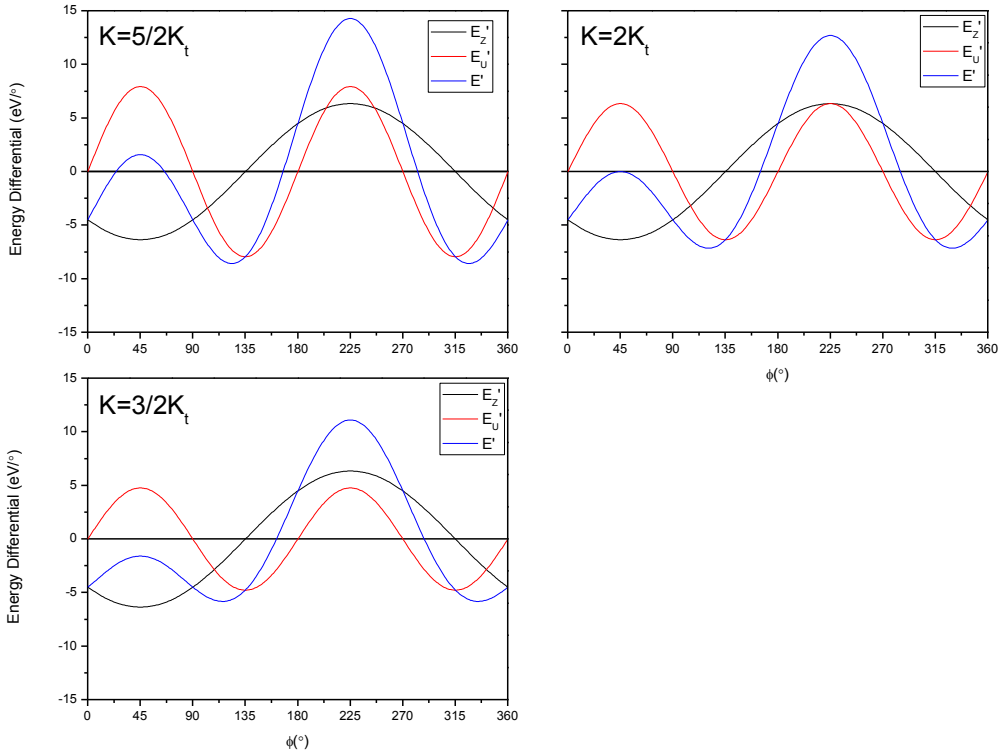

Fig.5.22 – Energy plots showing the energy differential of the Zeeman energy (E_z'), anisotropy energy (E_u') and system energy (E') for varying fractions of $K_{u,t}$ when Ø'=90°

illustrating the point of inflection at Ø=90° when $K_{eff}=K_{u,t}$. Note that all properties of the ring and the field strength are contained in the expression for K_t.

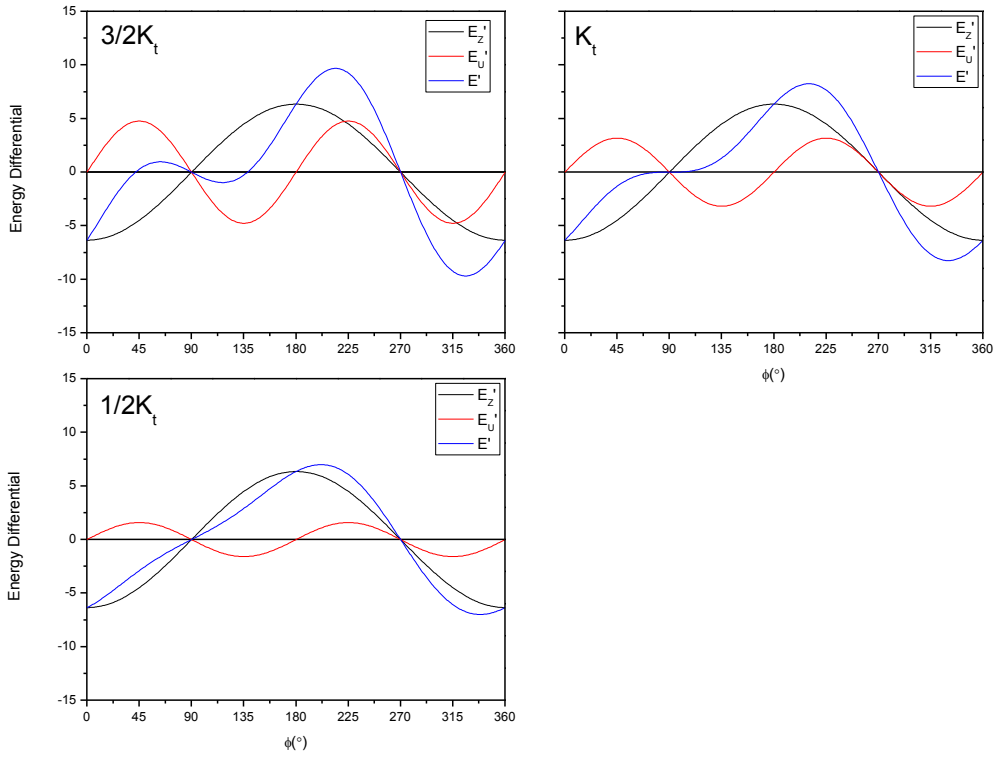

Fig.5.23 - Energy plots showing the energy differential of the Zeeman energy (E_z'), anisotropy energy (E_u') and system energy (E') for varying fractions of $K_{u,t}$ when and Ø'=135° illustrating limit of the appearance of energy minima below Ø=90°when $K_{eff}=2K_{u,t}$. Note that all properties of the ring and the field strength are contained in the expression for $K_{u,t}$.

In terms of $K_{u,t}$ the ranges of the three regimens are:

Regimen 1: $K \leq K_{U,t}(H, M_s, r, \Delta)$

Regimen 2: $K_{U,t}(H, M_s, r, \Delta) < K \leq 2K_{U,t}(H, M_s, r, \Delta)$

Regimen 3: $2K_{U,t}(H, M_s, r, \Delta) < K$

Having defined $K_{u,t}$ it is possible to produce a general set of hysteresis loops which apply to any ring geometry. Taking the ratio of K_{app} and $K_{u,t}$ for any ring the regimen can be predicted for any applied field magnitude. The hysteresis loops presented in Fig.5.24, Fig.5.25 and Fig.5.26 show simulated MOKE data where the x axis component of the rotating field H_x (normalised to the range of H_x) has been plotted against the measured x axis component of magnetisation M_x for the whole ring (normalised to the range of M_x for regimen 1).

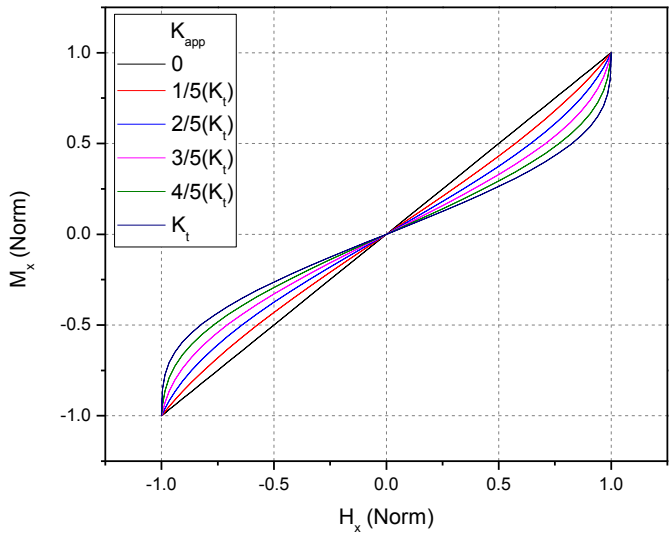

Fig.5.24 – Generalised hysteresis loops for rings in regimen 1 ($K \leq K_t$).

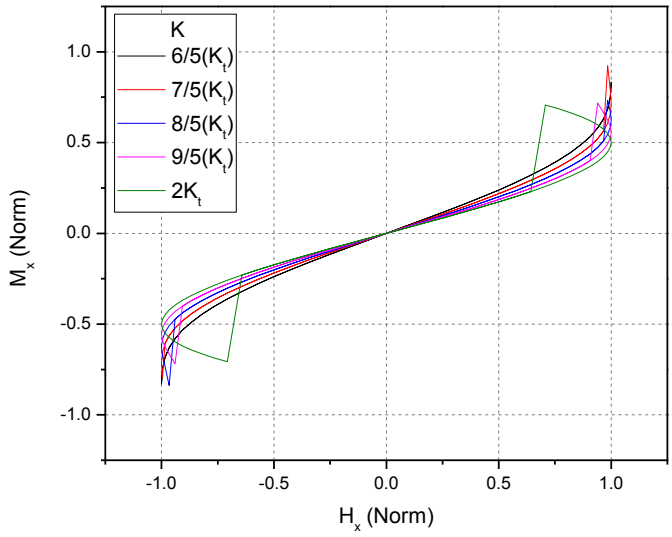

Fig.5.25 – Generalised hysteresis loops for rings in regimen 2 ($K_t < K \leq 2K_t$)

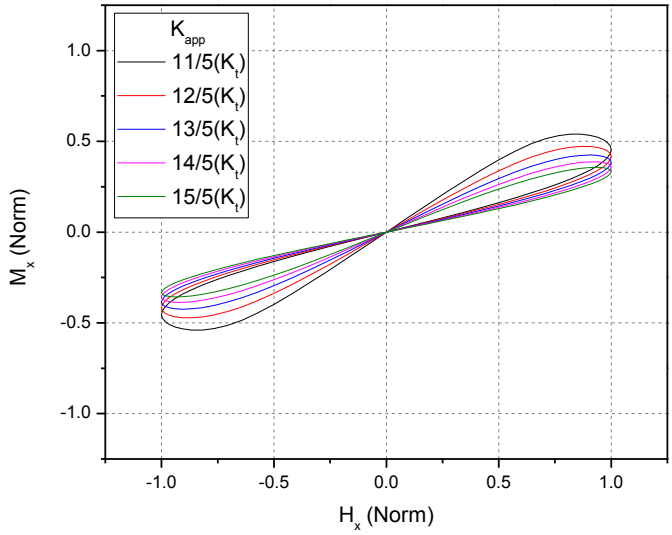

Fig.5.26 – Generalised hysteresis loops for rings in regimen 3 ($2K_t < K$).

With zero applied anisotropy the domain walls follow the applied field direction. This results in a linear relationship between the field and magnetisation components in the same direction (Fig.5.24). Applying anisotropy causes the domain walls to lag behind the field due to the competing energy term, which is seen as a distortion of the hysteresis loop

(Fig.5.24). As anisotropy is increased up to $K_{u,t}$ the domain walls lag further behind the field increasing the distortion in the loop characterised by an decrease in gradient followed by an increase as the normalised H_x approaches 1 (or -1). As the domain walls align with the field direction every 90° in regimen 1 all the normalised loops for this regimen have points at (1,1) and (-1,-1).

As the effect of the anisotropy increases up to $2K_{u,t}$ (Fig.5.25) the domain walls lag further behind the field, increasing the distortion seen in Fig.5.24, and the points (1,1) and (-1,-1) are no longer present. Regimen 2 is characterised by a discontinuity at field angles above Ø'=90° (and Ø'=270°) at the point that the effect of the field increases sufficiently to rotate the domain walls past Ø'=90° (or Ø'=270°). As the effect of anisotropy increases the discontinuity occurs at larger values of Ø', due to the representation of the rotating field used this is seen as a discontinuity at lower values of H_x.

Above $2K_{u,t}$ (Fig.5.26) the effect of anisotropy is strong enough to prevent the domain walls from rotating fully around the ring. Experimentally the phase lag caused by edge roughness is expected to open up the hysteresis loops[C} and so it is not expected that experimental data will match the idealised loops presented here perfectly.

5.2 - Ring Model By Finite Element

In order to gain information regarding the behaviour of domain walls in a ring with uniaxial anisotropy subjected to an in plane rotating magnetic field, finite element models were run using the finite element modelling (FEM) femme code. The aim of the simulations was to better understand the effect of anisotropy and ring geometry in order to design as effective an experiment as possible to observe a stress effect on domain walls.

The rings designed using the GiD package were circular with no edge roughness and had varying ring diameters and wire widths. The wire thickness for each ring was set to 5nm (significantly lower than the wire width values used) in order to ensure the shape anisotropy favoured magnetisation in the plane of the ring and a mesh size of 5nm was used. This design is shown schematically in Fig.5.27 with the defined x and y axes.

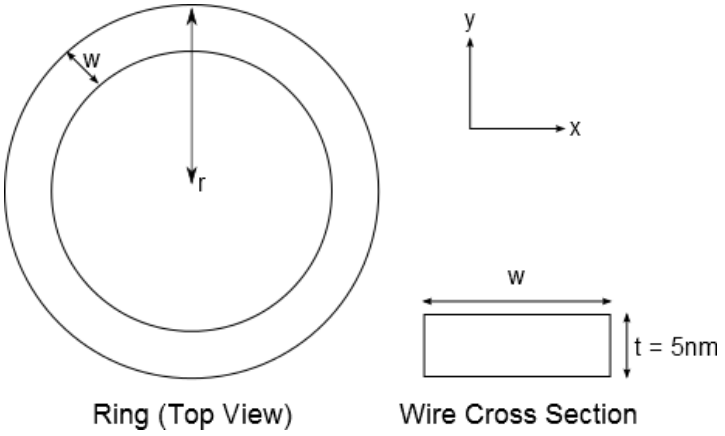

Fig.5.27 – Ring design used for FEM simulations with x and y axes defined for the ring's top view.

The material properties used in these simulations are those for Fe-Ga:

Anisotropy constant (from applied stress) $K_1 = 1500$ J/m ^{3}, $K_2 = 0$ J/m ^{3}

Magnetic polarisation $J_s = 1.1$ T [10]

Exchange constant = 1×10^{-11} J/m

Damping constant $\alpha = 0.02$ (unless stated)

Generic values for exchange and damping constant have been used. The first step in simulating the ring's behaviour was to initialise the model to the onion state such that there were two domain walls opposite each other in the ring. This was achieved by applying a magnetic field induction (B) greater than the magnetic polarisation of 1.1T to the ring in

the x direction. The field induction used was 2T and completely saturated the magnetisation of the ring in the x direction. Then the field was removed to allow the magnetic configuration to relax for 10ns. Due to the initial saturation the ring relaxes into the onion state with two transverse domain walls with magnetisation within the domain wall in the x direction. These steps are done using a damping constant α =1 as domain wall dynamics are not of interest during the initialisation and it is undesirable for the domain walls to be allowed to move during the initialisation stage.

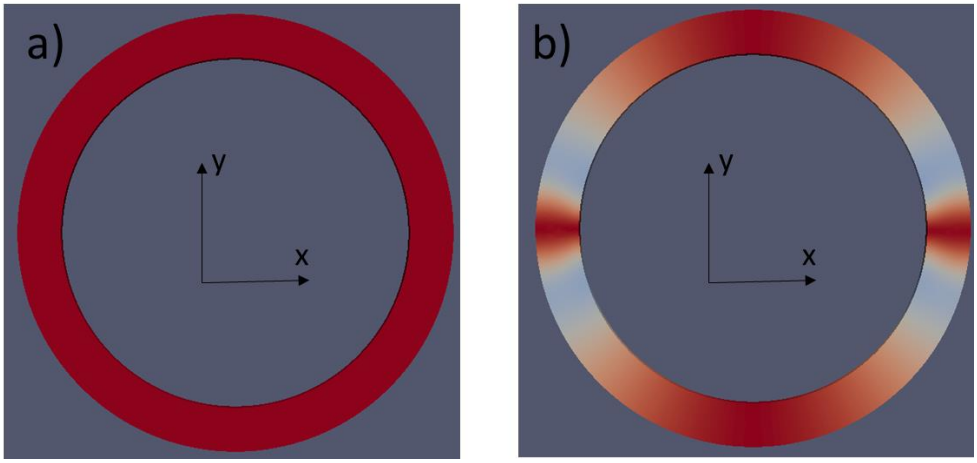

Fig.5.28 – a) Simulated ring saturated completely in the x direction during initialisation at 2 T applied field. b) Simulated ring relaxed into the onion state at 0 T applied field after saturation. Red represents magnetisation in the x direction and blue in the y direction.

In order to simplify the simulations an approach was taken where the domain walls were held in place using an applied field of 0.001T in the x direction and simulations were run using applied anisotropies at varying angles (θ) from the x direction ranging from 0° to 90°. This approach is shown schematically in Fig.5.29.

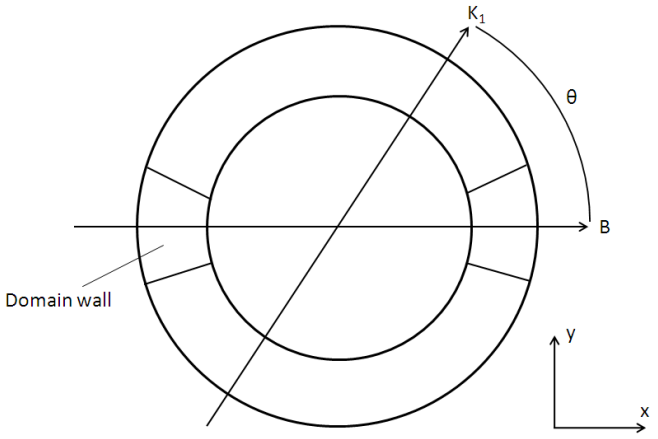

Fig.5.29 – Schematic diagram showing approach taken in FEM simulations.

The energy values follow a $\sin^2\theta$ relationship which indicates that the change in energy with θ is due to the applied anisotropy. Since the domain walls are held in place the energy of the system increases as the direction of the anisotropy moves away from the x axis. An example of one of these plots is shown in Fig.5.10.

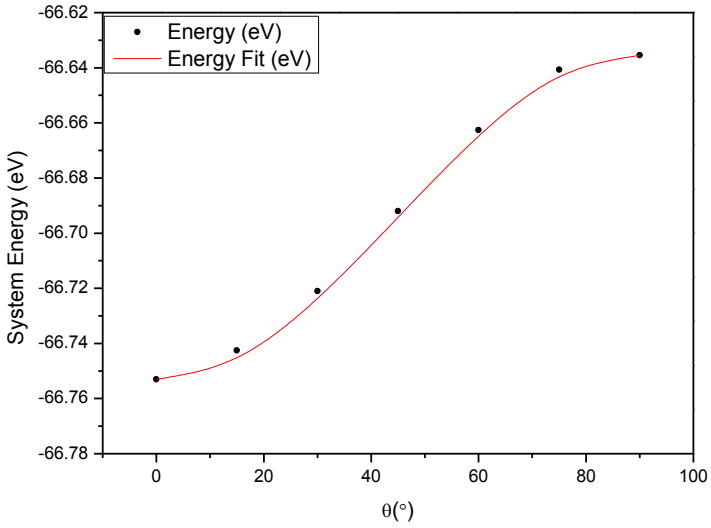

Fig.5.30 – Calculated system energies and fit for a ring with dimensions d=300nm, w=50nm.

The curve fit can be found for a data set using the following equation:

$$E_{fit} = E_0 + (E_{90} - E_0)sin^2\theta \quad (5.35)$$

Where E_0 is the energy of the system when θ is 0° and E_{90} is the energy of the system when θ is 90°.

The differential of this function gives the energy gradient for any value of θ. The energy gradient is of interest as it is this which will cause a domain wall to move to line up with an applied anisotropy due to the effective force experienced by the domain wall in the energy gradient. The effective force acts on the domain wall to move it towards the energy minimum position. It is possible to produce an energy gradient radially in the ring using a uniaxial anisotropy because of the curved geometry of the ring. The function for the energy gradient is therefore:

$$\frac{dE_{fit}}{d\theta} = 2(E_{90} - E_0)sin\theta cos\theta \quad (5.36)$$

An example of an energy gradient plot calculated in this way is shown in Fig.5.31.

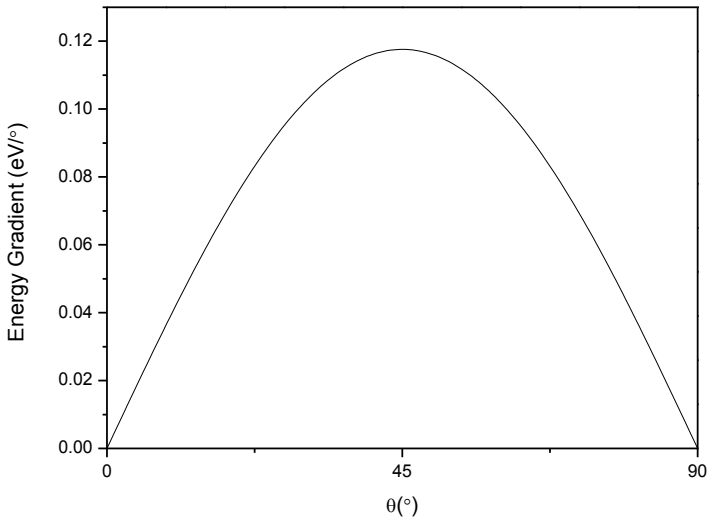

Fig.5.31 – Energy gradient as a function of θ for ring a ring with dimensions d=300nm, w=50nm.

It can be seen that the energy gradient is at its maximum when the domain wall is located at 45° to the anisotropy direction and that even though it is in its highest energy position when located at 90° to the anisotropy direction there is in fact no energy gradient at this position to cause it to move.

Using the results of the simulations two useful values can be calculated in order to assess the behaviour of different ring geometries. The first is the effective field acting on the wall (H_{eff}) which can be calculated as:

$$H_{eff} = \frac{1}{2\mu_0 m_s wt}\left(\frac{dE_{fit}}{d\Psi}\right) \tag{5.37}$$

Where μ_0 is the permeability of free space, m_s is the saturation magnetisation and Ψ is the radial distance of the domain wall from the anisotropy direction. Note that the differential in this case is different and can be calculated as:

$$\frac{dE}{dx} = 2(E_{90} - E_0)sin\theta cos\theta \frac{2\pi}{\pi d} \quad (5.38)$$

The second value that can be calculated is an estimate of the thermal stability of the domain wall when it is located in the energy well located in the anisotropy direction. This can be found by comparing the energy difference between E_0 and E_{90} with an estimate of the thermal energy in the ring at room temperature E_T given by:

$$E_T = kT \quad (5.39)$$

Where k is Boltzmann's constant and T is the temperature in Kelvin (taken to be 300K at room temperature). Therefore a figure of merit for the thermal stability is given by:

$$\frac{E_{90} - E_0}{kT} \quad (5.40)$$

If this figure is very low then the thermal energy in the system is high compared to the energy well the domain wall is located in and there is a high chance that the domain walls will overcome the energy well and annihilate. In order for the domain walls to be stable in the energy well the figure of merit should be as high as possible.

Fig.5.32 shows H_{eff} values calculated for domain walls located at 45° to the anisotropy direction (the maximum for any given ring) for a range of ring radii and wire widths.

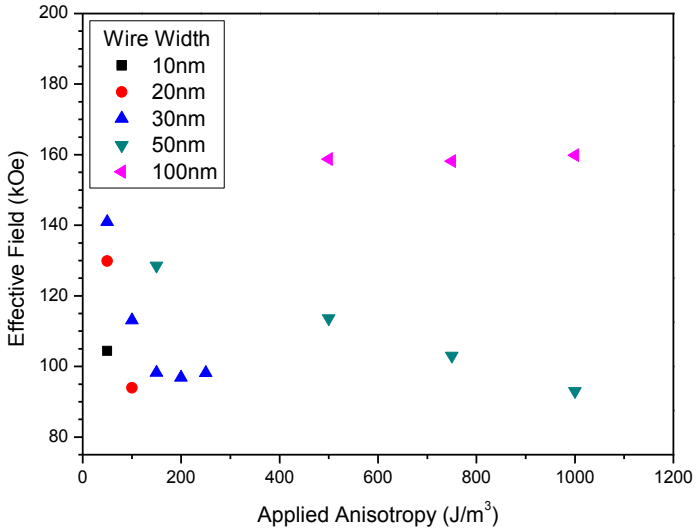

Fig.5.32 – Anisotropy induced effective fields at θ=45° for rings of varying radius and wire widths.

From Fig.5.32 it can be seen that the effective field acting on a domain wall is larger in wider wires and that the effective field is also greater in rings of lower radius. The reason that H_{eff} is greater in wider wires is likely be because of the greater domain wall volume in a wider wire which increases the total energy of the system when the domain wall is not aligned with the anisotropy direction. H_{eff} will be greater in rings with smaller radii because the distance between the high and low energy points on the ring is lower leading to a higher energy gradient. Due to the high energy gradient found in small rings the calculated values of H_{eff} are encouragingly large and suggest that if a similar anisotropy gradient can be created in a straight wire the position of domain walls in the wire could be controlled in this way. The magnitudes of the fields are particularly encouraging as a domain wall can be propagated with a field of only a few hundred Oe compared to the calculated effective fields of several kOe.

Fig.5.33 shows thermal stability figures of merit for various wire widths plotted as a function of the volume of the ring.

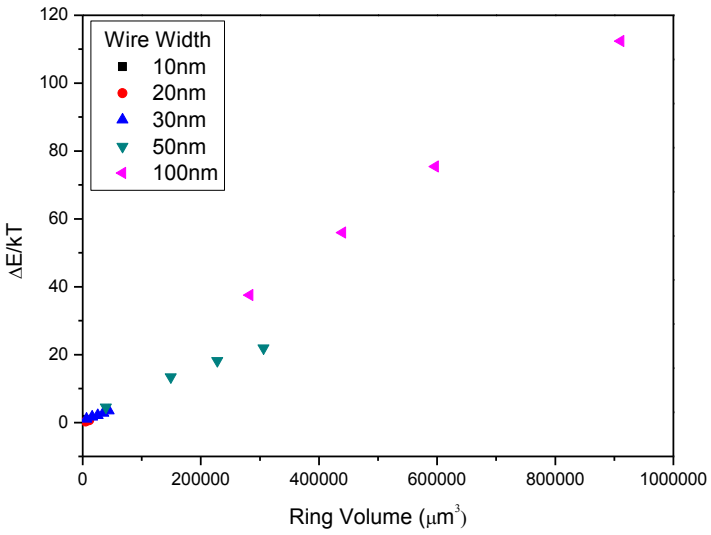

Fig.5.33 – Thermal stability figures of merit for varying ring volume (legend shows wire widths).

Fig.5.33 shows that the thermal stability is greater in rings of larger volume and wire width. The trend for greater stability in rings of greater width is again due to the larger domain wall volume which leads to a greater contribution to the system energy when the walls are not in the anisotropy direction. Because of this, the energy difference between the minimum and maximum energy is greater and thus more difficult to overcome through thermal energy. The trend for greater stability in rings of greater volume is due to the contribution to the system energy from the domains which is also lower when the domain walls are aligned with the anisotropy. Thus the difference between the high and low energy positions is significantly larger in rings with greater volume.

Even though the results indicate that rings with large widths and radii are more stable the energy well is still several times greater than kT at room temperature even in rings with radii as low as 150nm.

5.3 Experimental Measurements

In order to observe the effect of uniaxial anisotropy on the behaviour of magnetic rings subjected to a rotating field arrays of rings were prepared on Si substrates using EBL and thin film deposition techniques. The EBL was performed by Mark Rosamond at Leeds University using a JEOL JBX-6300FS. Two samples were prepared, the first with 30nm of sputtered METGLAS and the second with 25nm of thermally evaporated Ni. METGLAS was chosen due both to its ease of deposition and high expected magnetostrictive response. Ni was chosen based on the success in stress based movement of domain walls in Ni rings by Hockel *et al.*[7] The substrates were bonded to piezoelectric actuators from Piezomechanik using epoxy similarly to the device described in in detail in §6.2.1. This allowed in plane uniaxial strain to be applied to the rings by application of a voltage to the piezoelectric actuator. A schematic of the device used to test the ring structures is shown in Fig.5.34.

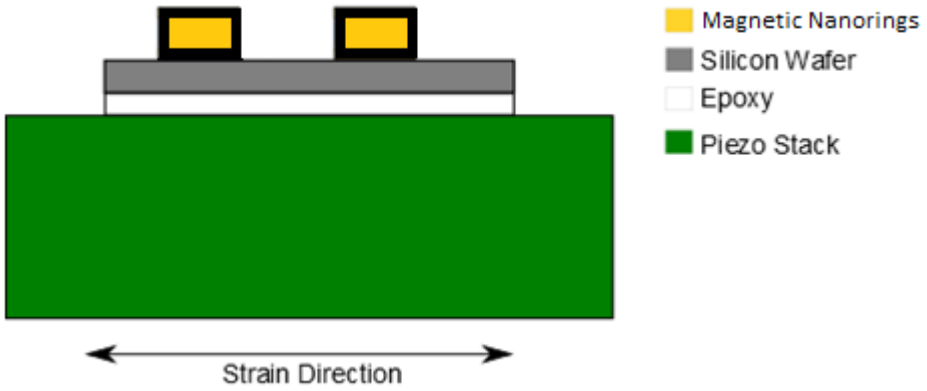

Fig.5.34 – Schematic of the device used to investigate the effect of uniaxial in plane strain on magnetic nanorings.

Though METGLAS was expected to exhibit a larger induced anisotropy than Ni for a given strain it was decided that the Ni rings should be investigated as the quality of the deposited structures was visibly superior in the Ni sample. In each of the arrays the rings were spaced at a distance of 2D to prevent interactions between the rings. The following are preliminary results for an array of Ni rings with dimensions w=200nm and D=500nm obtained using focussed MOKE. The focussed MOKE has a spot size of around 4 µm allowing several rings in the array to be measured simultaneously providing an average result for all measured rings. The rings were initialised by application of a high magnetic field to saturate them in plane then removing the field to allow them to relax to the onion state. A rotating magnetic field was applied and averaged hysteresis loops were measured at various applied voltages.

Fig.5.35 and Fig.5.36 show averaged hysteresis loops plotting the x component of the applied rotating field against the x component of magnetisation measured in the ring array for an applied voltage of 0V and 30V.

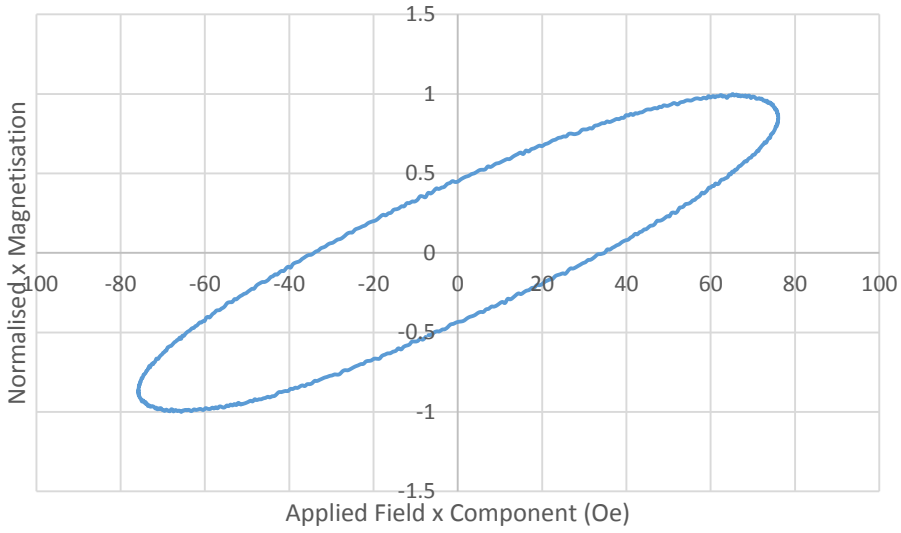

Fig.5.35 – Hysteresis loop for a ring array with dimensions w=200nm and D=500nm at an applied voltage of 0V.

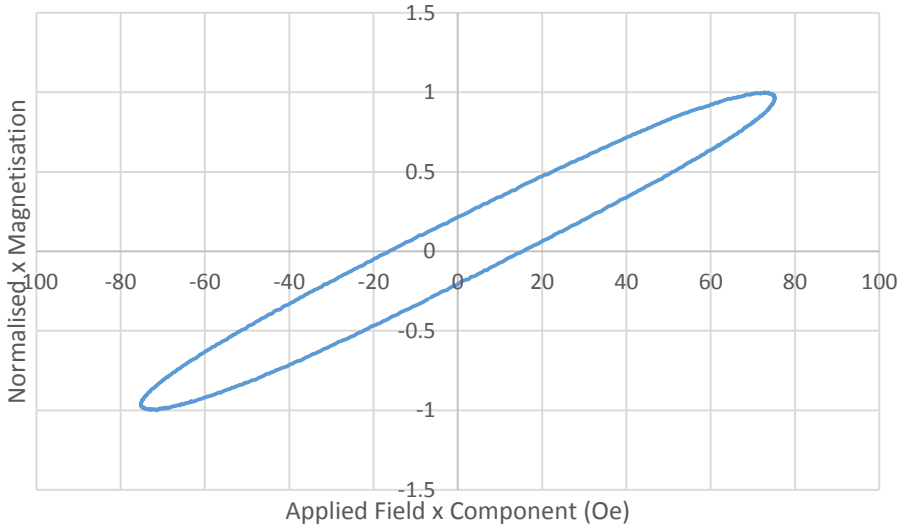

Fig.5.35 – Hysteresis loop for a ring array with dimensions w=200nm and D=500nm at an applied voltage of 30V.

It can be seen that the application of a voltage to the piezoelectric has the effect of distorting the measured loop, however the loops contain a much larger distortion from the idealised loops calculated above. This is assumed to be due to the phase lag between the field and domain wall direction caused by edge roughness. In order to attempt to remove

this phase lag distortion it was assumed that the loop for 0V does not exhibit any distortion due to uniaxial anisotropy. The phase lag for this loop was measured and the Kerr signal data was shifted by the measured amount to line up with the applied field peak resulting in the hysteresis loop in Fig.5.36.

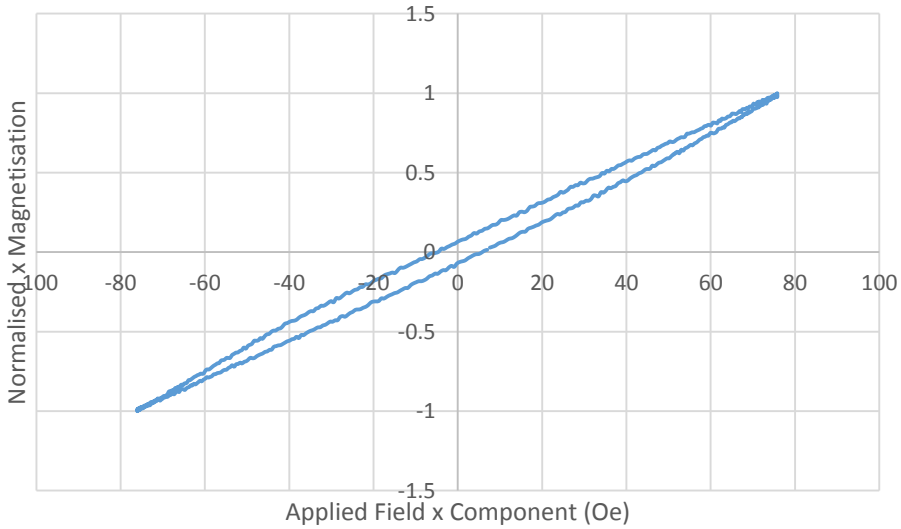

Fig.5.36 - Hysteresis loop for a ring array with dimensions w=200nm and D=500nm at an applied voltage of 0V with phase shift removed.

With the phase shift removed the hysteresis loop matches much more closely to the expected behaviour of a ring with domain walls following the applied field direction. The same phase shift was then applied to the loop for 30V resulting in Fig.5.37.

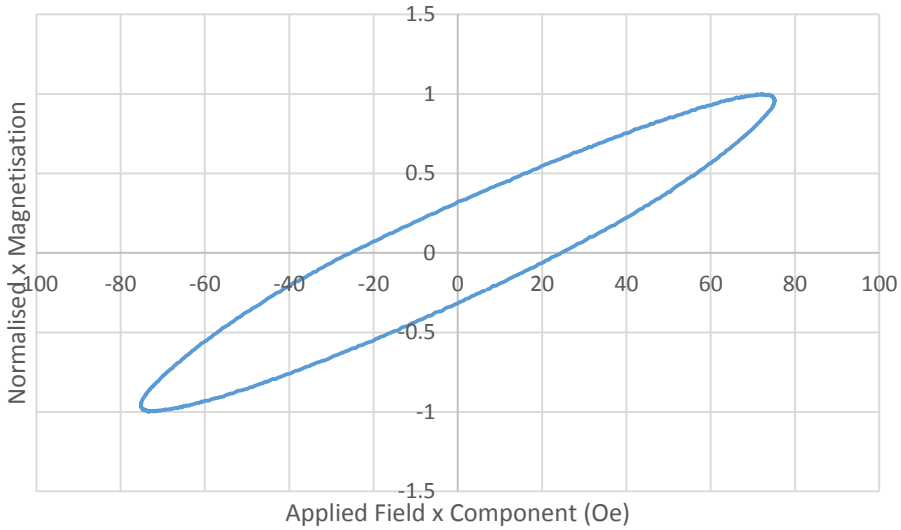

Fig.5.37 - Fig.5.36 - Hysteresis loop for a ring array with dimensions w=200nm and D=500nm at an applied voltage of 30V with phase shift removed.

The resulting loop still exhibits a distortion which is assumed to be caused by additional phase lag due to and applied in plane uniaxial anisotropy caused by the applied strain from the piezoelectric.

These initial results show that this system shows promise in the investigation of the effect of uniaxial in plane anisotropy on domain walls in soft magnetic nanorings. Future work with higher applied voltages and lower applied field should yield more quantitative results.

5.3 - Conclusions

An analytical model was created to simulate a soft magnetic nanoring magnetised in the onion state with an in plane uniaxial anisotropy and an in plane magnetic field. The model calculates the position of the head to head and tail to tail transverse domain walls in the ring for given values of r=ring centre radius, w= wire width, t= wire thickness, m_s=

saturation magnetisation, K_{app}= applied anisotropy, H= applied magnetic field and Ø'=angle between applied field direction and applied anisotropy direction. The position of the domain walls is calculated by calculating the energy minima of the total system energy which is made up of an anisotropy energy contribution and a Zeeman energy contribution. This model was used to determine the behaviour of a soft magnetic ring in the onion state with an applied in plane uniaxial magnetic anisotropy subjected to a rotating in plane magnetic field. It was found that the application of a uniaxial anisotropy causes the domain walls not to follow the field direction exactly as it rotates around the ring. The strength of this effect increases as r decreases, w increases, m_s decreases, K_{app} increases and H decreases. Three regimens were found depending on the strength of the effect of the effect. When the effect of the anisotropy is low the domain walls rotate around the ring smoothly lagging behind the magnetic field. For an intermediate effect the domain walls rotate around the ring fully but discontinuities exist where the domain walls suddenly move to a new position in the ring. For a large effect the domain walls do not move around the ring fully but oscillate around their start position as the magnetic field is rotated. It was shown that the anisotropy thresholds for these effects could be expressed in terms of the anisotropy K_t which is a function of r, w, m_s and H. It was then shown that generalised hysteresis loops could be produced which simulate the behaviour of rings with any combination of properties expressed in terms of K_t.

Magnetic nanorings were also simulated using finite element modelling. Each ring was initialised to produce the magnetic onion state and the domain walls were pinned using an applied magnetic field. In plane uniaxial anisotropy was applied at varying angles and the magnetic system energy of the simulation was measured for each angle. The system energy increased with a $\sin^2\theta$ relationship to the change in anisotropy direction allowing an energy gradient to be calculated for the system for varying alignment of the domain walls with the

anisotropy direction. It is predicted that domain walls will move in an energy gradient to seek the energy minimum point. The effective fields acting on the domain walls due to the applied anisotropy at the highest energy gradient point were calculated showing that the effective field is highest for low ring radius and high wire width. This is because the low ring radius maximises the anisotropy gradient experienced by a domain wall in a curved wire with a uniaxial applied anisotropy and the high wire width increases the volume of the domain wall being acted on. This is consistent with the predictions of the analytical model which also predicts that low radius and high wire width will maximise the effect of applied anisotropy on domain walls in a ring. A figure of merit was calculated from the simulations which calculated the difference in energy between the highest energy from the simulations for each ring (domain walls aligned 90° from the anisotropy direction) and the lowest energy from the simulations for each ring (domain walls aligned with the anisotropy direction) and compared this value to the thermal energy kT. This showed that the rings with the higher volume and rings with wider wire widths had higher had a higher figure of merit for thermal stability. The thermal stability figures of merit for all but the smallest rings were much greater than 1 suggesting that a device based on domain wall control by anisotropy gradients would have good thermal stability.

Both of these models suggested that the use of anisotropy gradients is a good candidate for the control of domain walls in nanowires.

Initial MOKE data from an array of Ni nanorings with dimensions w=200nm and D=500nm initialised to the onion state and subjected to an in plane rotating field showed a distortion in the measured hysteresis loops when strain was applied using a piezoelectric transducer. Loops modified to account for phase lag caused by edge roughness suggest that the

difference observed with applied voltage is not caused by edge roughness and could be accounted for by strain induced anisotropy. This system shows promise for further work.

5.4 - References

[1] D.Atkinson, D.S.Eastwood and L.K.Bogart, *Appl. Phys. Lett.*, **92**, 022510 (2008)

[2] D.Atkinson, D.A.Allwood, G.Xiong, M.D.Cooke, C.C.Faulkner and R.P.Cowburn, *Nat. Mater.*, **2**, 85 (2003)

[3] S.P.Parkin, M.Hayashin and L.Thomas, *Science*, **320**, 190 (2008)

[4] C. Faulkner, M.D.Cooke, D.A.Allwood, D.Petit, D.Atkinson and R.P.Cowburn, *J. Appl. Phys.*, **95**, 11, 6717 (2004)

[5] M. Kläui, C.A.F. Vaz, L.J. Heyderman, U. Rüdiger and J.A.C. Bland, *J. Magn. Magn. Mater.*, **290**, 61 (2005)

[5] J.Dean, M.T.Bryan, T.Schrefl and D.A.Allwood, *J. Appl. Phys.*, **109**, 023915 (2011)

[6] M.Negoita, T.J.Hayward, J.A.Miller and D.A.Allwood, *J. Appl. Phys.*, **114**, 013904 (2013)

[7] J.L.Hockel, A.Bur, T.Wu, K.P.Wetzlar and G.P.Carman, *Appl. Phys. Lett.*, **100**, 022401 (2012)

6 - Uniaxial Stress Applied to Magnetostrictive Notched Wires

The control of magnetic domain walls in magnetic nanowires is of much interest due to applications in magnetic logic and memory devices [1][2][3]. One of the most well studied methods of controlling domain walls is the use of artificial 'pinning' sites, usually in the form of notches, along the length of the wire [4][5]. As a domain wall is driven through a wire, for example by a magnetic field, it interacts magnetostatically with the notch, requiring a higher driving force, in this case a higher field, to pass through the notch [4][5]. If a high enough driving force is not provided it will become pinned at the notch [4][5]. Pinning and de-pinning of domain walls at notches is very sensitive to the structure of the domain walls [6] and shows a large degree of stochasticity, meaning it is very difficult to predict at what field a domain wall will be de-pinned. Some attempts to introduce selective switching, e.g. through controlled exchange bias [7], have been made. This chapter follows this principle and investigates how application of a uniaxial strain-induced magnetic anisotropy to a notched wire system affects the pinning of domain walls at notches. This could offer a controllable way to change the driving force required to de-pin a domain wall from a notch.

6.1 – Finite Element Model

6.1.1 - Modelling of Domain Wall De-pinning From Notched Wires

Finite element analysis was used in order to predict the effects of uniaxial anisotropy on the de-pinning of domain walls from a notched wire. This represents the uniaxial anisotropy resulting in a uniaxially strained magnetostrictive material such as could be induced in a

wire coupled to a piezoelectric substrate. There was assumed to be no other anisotropy contribution in the material other than the induced anisotropy.

Notched wire models were designed and meshed using tetrahedral elements in the finite element package GiD[8] and the resulting models were solved using femme and visualised using Paraview[9] (see §4.6 for details). Fig.6.1 shows the design used in the notched wire models. The value x will be referred to as the wire width. In each of the models the wire thickness was 5nm, wire length was 2 μm and the mesh size was 5nm for wire widths of 50, 100 and 200 nm (Fig. 6.1). A notch halfway along the length of the wire had width and depth of $x/4$ to maintain a constant proportion of the wire width. The pointed wire ends prevent nucleation of domains at the wire ends. The material properties were selected to simulate the behaviour of Fe-Ga:

Magnetic polarisation [10]: 1.1 T

Exchange stiffness constant, A=1.1 X 10^{-11} J/m

Damping constant, α= 0.02

The values used for exchange stiffness and damping constant are generic values. Each simulation was initialised to produce a transverse head-to-head domain wall approximately 500 nm to the left of the notch. A small field perpendicular to the wire was used to initialise the domain wall to either the 'up' or 'down' chirality. This was performed with a damping constant of α=1 to allow the initialisation to be completed quickly and without the domain wall moving in the wire. Following initialisation the damping constant was reset to α=0.02 and an applied magnetic field H increased at a rate of 80 (A/m)/ns in the direction of the wire long axis direction as shown in Fig.6.1. Induced uniaxial anisotropy represented by a

magnetocrystalline anisotropy of different strengths was applied either perpendicular (K_{perp}) or parallel (K_{par}) to the wire for each simulation (see Fig.6.1).

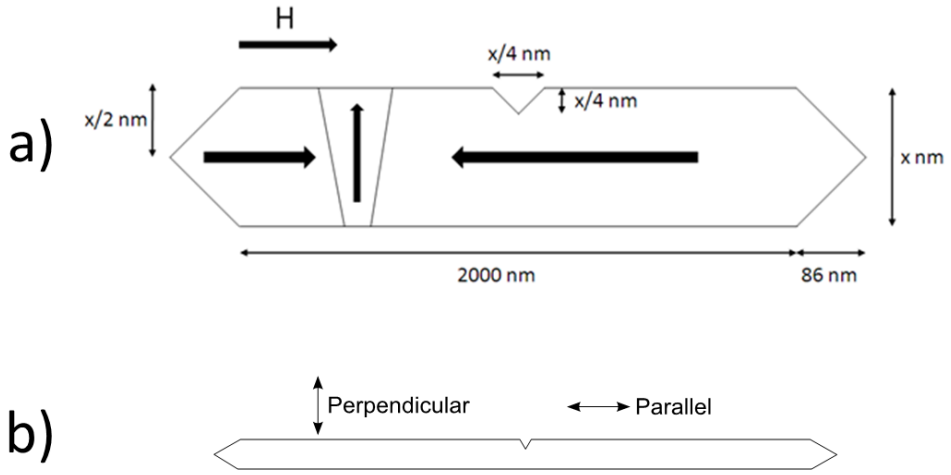

Fig.6.1 – Diagrams of notched wire design showing a) dimensions of the model and applied magnetic field direction (H), and b) parallel and perpendicular anisotropy directions.

The increasing applied magnetic field caused the domain wall to propagate towards the notch where it becomes pinned. Once the applied field was high enough it would allow the domain wall to overcome the pinning potential and continue its propagation down the wire. The rapid motion of a domain wall upon de-pinning caused a sudden reduction in various energy terms, including magneto-static, exchange and, most notably, Zeeman energy. The de-pinning field for each simulation was found by plotting the magnetic system energy as a function of applied field. When the domain wall de-pinned from the notch the system energy rapidly decreased as can be seen in the examples shown in Fig.6.2. For each of the induced anisotropy terms domain wall de-pinning mechanism was determined by observing the magnetisation configurations from the simulations.

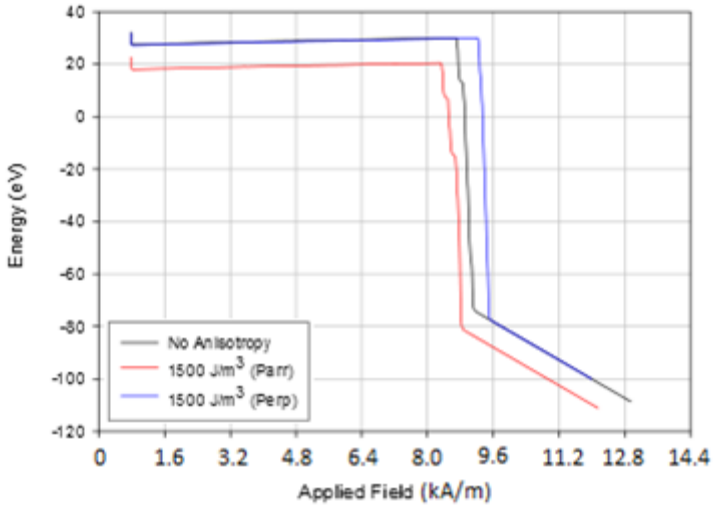

Fig.6.2 – Simulated system energy as a function of applied field for a 100nm wide notched wire for no applied anisotropy and 1500 J/m^3 applied parallel (Parr) and perpendicular (Perp) to the wire long axis.

Fig.6.3 shows how de-pinning field depended upon induced anisotropy in a 100 nm wide wire with the transverse wall in the 'up' chirality shown in Fig.6.4. In the up chirality the moments at the centre of the transverse wall are oriented towards the edge of the wire containing the notch. Note that in all simulated domain images red represents positive magnetisation in the wire long axis direction, blue represents negative magnetisation in the wire long axis direction and white represents either positive or negative magnetisation perpendicular to the wire long axis direction.

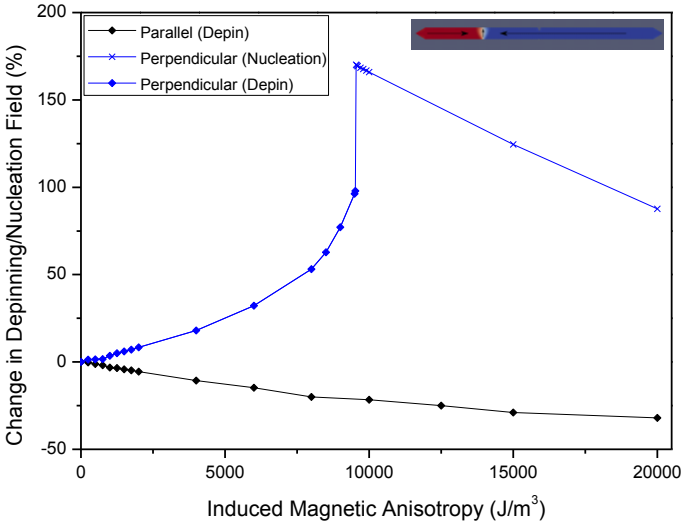

Fig.6.3 – Modelled change in de-pinning fields for 100 nm wide wire with an 'up' chirality transverse domain wall.

Fig.6.4 – 'Up' chirality head to head transverse domain wall in 100 nm wide wire showing magnetisation direction in domains and centre of domain wall.

The de-pinning field decreased with anisotropy applied parallel to the wire and increased with anisotropy applied perpendicular to the wire until a critical anisotropy of 9525 – 9550 J/m^3 was reached. Above this point the de-pinning field increased sharply and any further increase in anisotropy resulted in a linear decrease in the de-pinning field. It will be shown later that this critical anisotropy was associated with a change in the 'de-pinning' mechanism of the domain wall accounting for the sudden change in behaviour.

Figures 6.5 – 6.9 show simulated images of domain walls under increasing applied fields both pinned and shortly after de-pinning from a notch, with different degrees of induced

anisotropy in each figure. With no uniaxial anisotropy (Fig. 6.5), the domain wall is pinned to the left of the notch and de-pins once a high enough field is reached. This behaviour is consistent with an energy barrier to de-pinning [5]. Similar de-pinning behaviour was observed when a large anisotropy (20 kJ/m^3) was applied parallel to the wire (Fig. 6.6) although the de-pinning field is much lower than before, indicating a lower energy barrier with anisotropy in the wire direction. It is interesting to note that the domain wall width is significantly reduced now as the wall magnetisation is in the hard axis direction and this may result in a reduced magneto-static interaction of the wall with the notch geometry. For moderate anisotropy (8 kJ/m^3) applied perpendicular to the wire (Fig. 6.7), similar behaviour to that seen in Figs. 6.5 and 6.6 is again observed, although now with de-pinning requiring larger magnetic fields. However, larger perpendicular anisotropy, e.g. 15 kJ/m^3, applied to the wire (Fig. 6.8) results in a change in de-pinning behaviour. Rather than the pinned domain wall de-pinning, a new domain was nucleated from the right hand side of the notch to create two new domain walls. One of these annihilated the pinned domain wall while the other propagated through the wire to effect magnetisation reversal. It was even possible for this process to leave a 360° domain wall pinned at the notch as shown in Fig.6.9 obtained with an anisotropy of 20 kJ/m^3 perpendicular to the wire.

H=0.88 kA/m

H=9.47 kA/m

H=9.51 kA/m

H=9.55 kA/m

Fig.6.5 – De-pinning of 'up' head to head transverse domain wall with no applied anisotropy for various applied magnetic field, H.

H=5.97 kA/m

H=6.01 kA/m

H=6.05 kA/m

Fig.6.6 – De-pinning of 'up' head to head transverse domain wall with 20,000 J/m^3 applied parallel to wire for various applied magnetic field, H.

H=13.37 kA/m

H=13.41 kA/m

H=13.45 kA/m

Fig.6.7 – De-pinning of 'up' head to head transverse domain wall with 8000 J/m^3 applied perpendicular to wire for various applied magnetic field, H.

19.50 kA/m

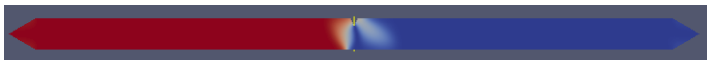

19.54 kA/m

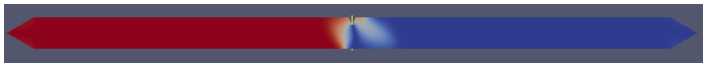

19.58 kA/m

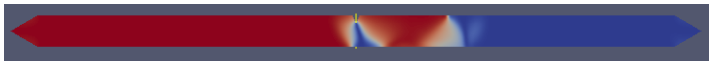

19.61 kA/m

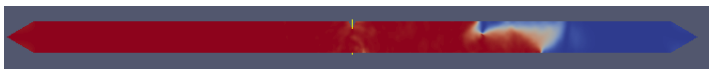

Fig.6.8 – De-pinning of 'up' head to head transverse domain wall by nucleation of a reverse domain with 15,000 J/m^3 applied perpendicular to wire for various applied magnetic field, H.

H=16.28 kA/m

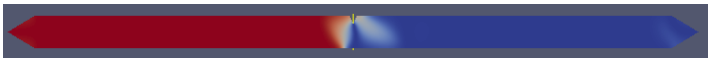

H=16.31 kA/m

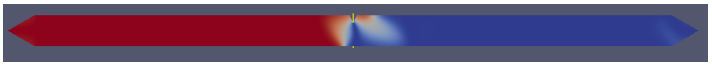

H=16.35 kA/m

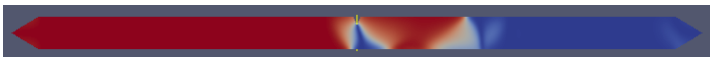

H=16.39 kA/m

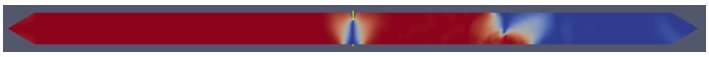

H=20.69 kA/m

Fig.6.9 – 360° domain wall left at notch after nucleation of a reverse domain with 20,000 J/m^3 applied perpendicular to wire.

Fig.6.10 shows the de-pinning/nucleation fields for the domain wall and the switching fields for the saturated wire (no initialised domain wall present) as a function of uniaxial anisotropy. It can be seen that as anisotropy perpendicular to the wire is increased the switching field of the saturated wire decreases linearly. Simulations showed that the nucleation of reverse domains occurs at the notch for the saturated wire, this was true for each of the wire widths studied and each of the simulations of saturated wires. This is the same trend observed in the wires where the domain wall 'de-pins' by nucleation. It can also

be seen that the presence of the domain wall at the notch decreases the field required to nucleate the new domain at the notch. This is probably due to the stray field from the domain wall at the notch contributing to the nucleation of the new domain.

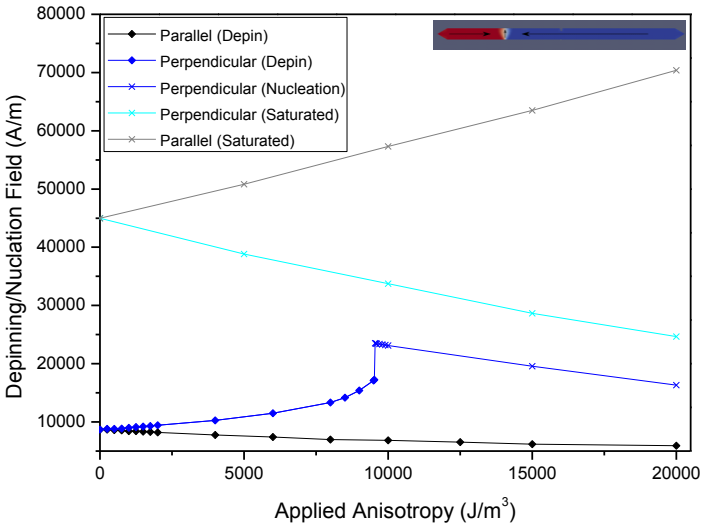

Fig.6.10 – Comparison of de-pinning fields of ‘up’ head to head transverse domain walls to switching fields of saturated wire for 100 nm wide wire.

Fig.6.11 shows the change in de-pinning fields for the 100nm wide wire with a transverse wall in the 'down' chirality shown in Fig.6.32. In the down chirality the moments at the centre of the transverse wall are oriented towards the edge of the wire without the notch.

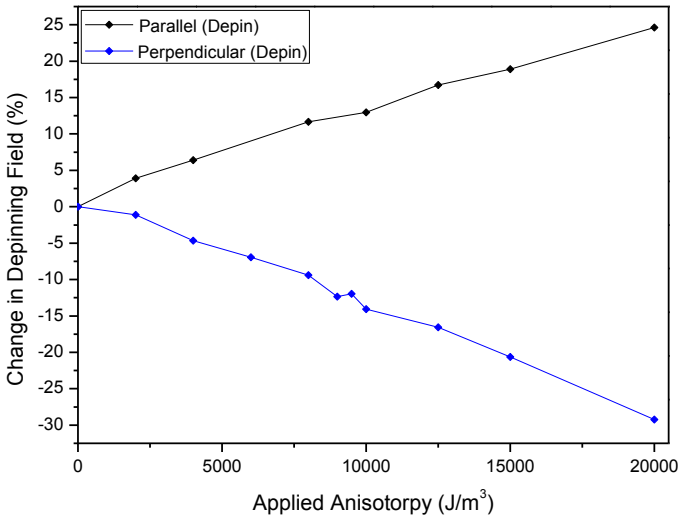

Fig.6.11 – Modelled change in de-pinning fields for 100 nm wide wire with ‘down’ chirality transverse domain wall.

Fig.6.12 - ‘Down’ chirality head to head transverse domain wall in 100 nm wide wire showing magnetisation direction in domains and centre of domain wall.

Unlike the 'up' chirality increasing parallel anisotropy increases the de-pinning field and perpendicular anisotropy decreases the de-pinning field for the ‘down’ chirality on the 100nm wide wire. Fig.6.13 shows the de-pinning mechanism for the 'down’ chirality. The domain wall is pinned at the centre of the notch and de-pins when a high enough field is reached. This behaviour is consistent with an energy well[5]. There was no switching by nucleation of a reverse domain for the ‘down’ chirality.

Fig.6.13 - De-pinning of 'down' head to head transverse domain wall with no applied anisotropy for various applied magnetic field, H.

In order to determine the effect of a wider wire simulations with a wire width of 200 nm were performed. Fig.6.14 shows the change in de-pinning fields for the 200nm wide wire with a transverse wall in the 'up' chirality. The de-pinning field decreases linearly with increasing anisotropy perpendicular to the wire.

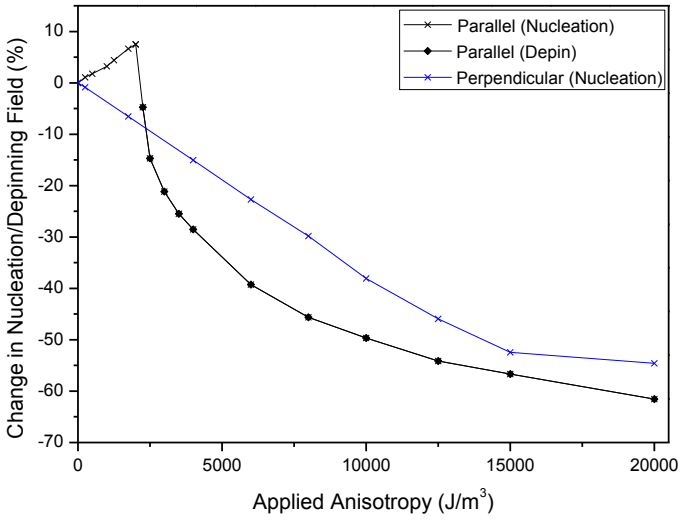

Fig.6.14 – Modelled change in de-pinning fields for 200 nm wide wire with 'up' chirality head to head transverse domain wall at various applied anisotropies.

The de-pinning field increases linearly with increasing parallel anisotropy up to a critical anisotropy between 2000 J/m^3 and 2250 J/m^3 at which point the de-pinning field decreases

sharply and any further increase in anisotropy results in a decrease in the de-pinning field. It will be shown that as in the 100nm wire the change is associated with a change in 'de-pinning' mechanism. The resulting changes in depinning field are large enough that they should be observable experimentally.

Fig.6.15 shows the de-pinning of a domain wall with no anisotropy applied. It can be seen that with no field applied the de-pinning mechanism is in fact a nucleation event of the type shown in Fig.6.8.
This explains the differing behaviour of this wire width compared to the 100nm wide wire.

Increasing perpendicular anisotropy promotes nucleation of the new domain lowering the de-pinning field and increasing parallel anisotropy inhibits nucleation increasing the de-pinning field. At the critical parallel anisotropy the de-pinning mechanism switches to the type shown in Fig.6.3 for the 100nm wire. This de-pinning mechanism is promoted by parallel anisotropy and so the de-pinning field decreases with increasing anisotropy.
Fig.6.16 shows the 200nm wire switching with a parallel anisotropy of 15,000 J/m^3, high enough to exceed the critical anisotropy.

13.70 kA/m

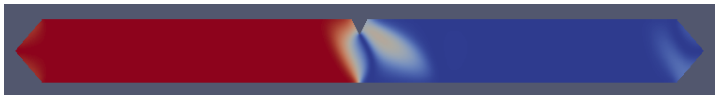

13.81 kA/m

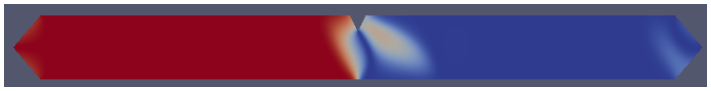

13.92 kA/m

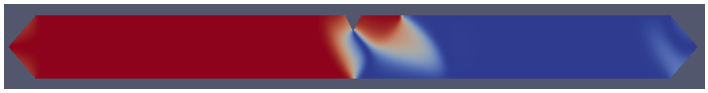

14.04 kA/m

Fig.6.15 – De-pinning of 'up' head to head transverse domain wall in 200 nm wide wire by nucleation of a reverse domain with no applied anisotropy for various applied magnetic field, H.

57.73 kA/m

62.17 kA/m

64.43 kA/m

65.58 kA/m

66.72 kA/m

Fig.6.16 – De-pinning of 'up' head to head transverse domain wall with 15,000 J/m^3 applied parallel to wire for various applied magnetic field, H.

Fig.6.17 shows the de-pinning/nucleation data for the domain wall and the switching fields for the saturated wire. It can be seen that as anisotropy perpendicular to the wire is

increased the switching field of the saturated wire decreases linearly. As in the 100nm wide wire the nucleation of the reverse domains occurs at the notch for the saturated wire. This is the same trend observed in the wires where the domain wall 'de-pins' by nucleation. Like the 100 nm wide wire the presence of the domain wall at the notch decreases the field required to nucleate the new domain at the notch.

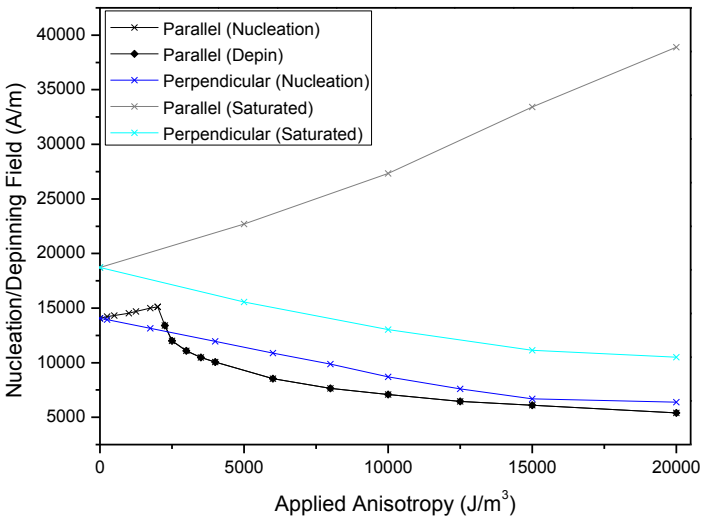

Fig.6.17 – Comparison of de-pinning fields of ‘up’ head to head transverse domain walls to switching fields of saturated wire.

In order to determine the effect of a narrower wire simulations with a wire width of 50 nm were performed. Fig.6.18 shows the change in de-pinning fields for the 50nm wide wire with a transverse wall in the 'up' chirality.

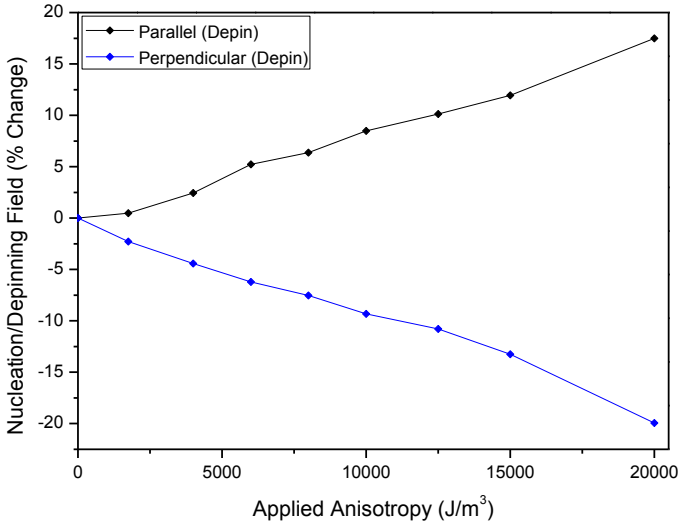

Fig.6.18 – Modelled change in de-pinning fields for 50 nm wide wire with 'up' head to head chirality transverse domain wall.

For the 50 nm wide wire increasing perpendicular anisotropy decreases the de-pinning field while an increase in parallel anisotropy increases the de-pinning field. This trend is opposed to the observed trends for the 100 nm and 200 nm wide wires and it is readily apparent that this is due to a different pinning mechanism at the notch.

Fig.6.19 – Transverse 'up' head to head domain wall pinned at notch in 50nm wide wire.

Fig.6.19 shows that in the 50nm wide wire 'up' chirality domain walls pass through to the right hand side of the notch and are pinned. It is this difference in pinning that is responsible for the difference in behaviour. In contrast to the pinning mechanism of the 100 nm and 200 nm wires this mechanism's behaviour is consistent with an energy well.

Fig.6.20 - De-pinning of 'up' head to head transverse domain wall with no applied anisotropy for various applied magnetic field, H.

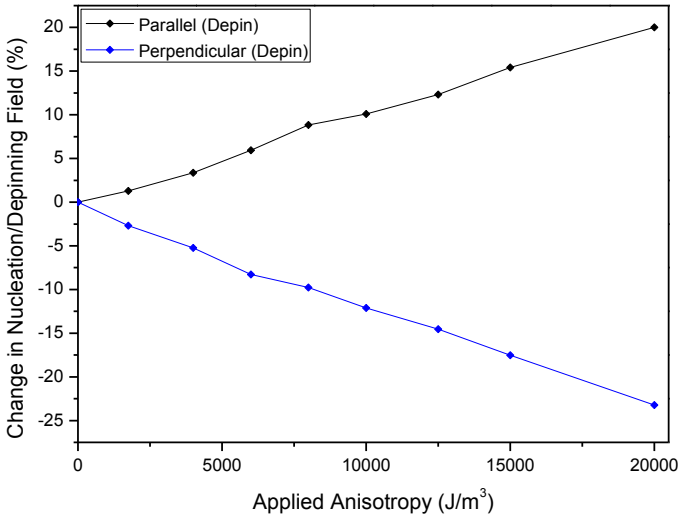

Fig.6.21 – Modelled change in de-pinning fields for 500 nm wide wire with 'down' head to head chirality transverse domain wall.

Fig.6.21 shows data for a 50 nm wide wire with domain wall in the 'down' chirality. An increase in perpendicular anisotropy decreases the de-pinning field while an increase in parallel anisotropy increases the de-pinning field. This is consistent with the behaviour observed in the 100 nm and 200 nm wide wires.

H=15.21 kA/m 

H=15.33 kA/m 

H=15.44 kA/m 

Fig.6.22 - De-pinning of ‘down’ head to head transverse domain wall with no applied anisotropy for various applied magnetic field, H.

In order to test the effect of anisotropy on de-pinning behaviour experimentally it was decided that a symmetrical square notch would be a better structure than an asymmetrical triangular notch. This was decided firstly as it has been reported that square notches have the least variation in de-pinning field[11], secondly because no control of domain wall chirality is required when testing a symmetrical notch and thirdly as the square notch can be produced more reliably using the EBL facilities available. Fig.6.23 shows the change in de-pinning fields for a 100 nm wide wire with a head to head transverse wall and a symmetrical square notch with combined notch depth of 25 nm.

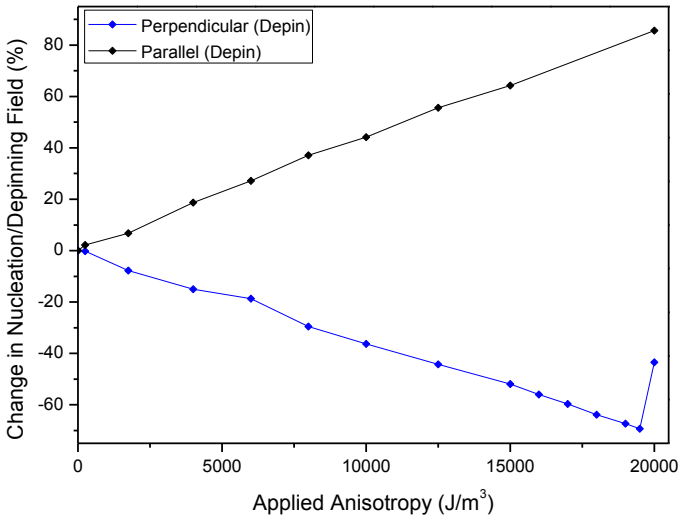

Fig.6.23 – % change in de-pinning fields for 100 nm wide symmetrical square notch wire with head to head transverse domain wall.

It can be seen from Fig.6.23 that as parallel anisotropy is increased the de-pinning field increases and that as perpendicular anisotropy is increased de-pinning field decreases. This is consistent with the energy well behaviour observed in the down chirality simulations for the asymmetric triangular notches. It can also be seen in Fig.6.24 that the domain walls sit inside the symmetrical square notch which is consistent with energy well behaviour [5].

The only exception to the observed trend is the 20,000 J/m^3 perpendicular simulation shown in Fig.6.25. In this case the anisotropy has increased the domain wall size to such a degree that it no longer sits at the centre of the notch. Rather it sits to the left of the notch and de-pins at a higher field than the 19,500 J/m3 perpendicular simulation. This behaviour is consistent with an energy barrier[5] as observed in the up chirality triangular notch simulations.

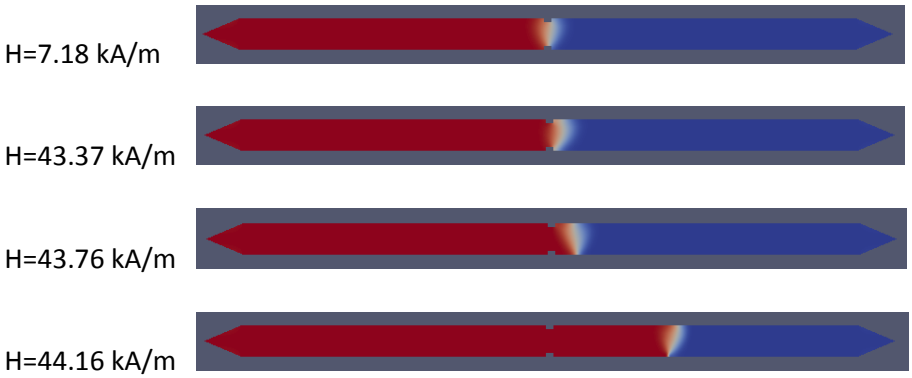

Fig.6.24 – De-pinning of head to head transverse domain wall in a 100nm wide wire with symmetrical square notch with no applied anisotropy for various applied magnetic field, H.

Fig.6.25 – De-pinning of head to head transverse domain wall with 20,000 J/m^3 applied perpendicular to wire for various applied magnetic field, H. Note that the high applied perpendicular anisotropy and the stray field from the domain wall cause moments in the domain after the notch to cant away from being parallel to the wire, shown in this figure as white sections in the blue domain.

6.1.2 - Summary of Modelling Work

Results from a simulated 100 nm wide wire showed that for a domain wall in the 'up' chirality application of uniaxial anisotropy parallel to the wire reduced de-pinning fields while application of uniaxial anisotropy perpendicular to the wire increased de-pinning fields up to a critical anisotropy at which point the wire reverses due to nucleation of a new domain after the notch rather than de-pinning of the wall, at anisotropies above the critical value the de-pinning field decreases linearly with applied anisotropy. The presence of the domain wall at the notch decreases the field required to nucleate the reverse domain. Results from the 100 nm wide wire with a 'down' chirality show an increase in de-pinning field with anisotropy applied parallel to the wire and a decrease with the anisotropy applied perpendicular to the wire. Due to the difference in the pinning mechanism for the 'down' chirality none of the wires switched by nucleation of a reverse domain.

In the wider 200 nm wide wires with ‘up’ chirality domain walls the predominant switching mechanism was nucleation of a reverse domain at the notch. Like the 100 nm wide wire application of uniaxial anisotropy perpendicular to the wire reduced the field required for switching by nucleation. Application of uniaxial anisotropy parallel to the wire increased the switching field until a critical anisotropy is reached at which switching by nucleation is suppressed and de-pinning of the wall becomes favourable. As the anisotropy applied parallel to the wire is increased above this point the de-pinning field is reduced similarly to the case of the 100 nm wide wire.

For a narrower 50 nm wide wire a domain wall in the ‘up’ chirality pins to the right of the notch rather than to the left as was seen for the ‘up’ chirality in the 100 nm and 200 nm wide wires. This results in different behaviour with an increase in de-pinning field as anisotropy is applied parallel to the wire and a decrease with the anisotropy applied perpendicular to the wire similar to the behaviour of the 100 nm wide wire with a domain wall in the ‘down’ chirality.

For the 100 nm wide wire with a symmetrical square notch there is no chirality dependent behaviour and the results show behaviour similar to the 100 nm wide wire with triangular notch and ‘down’ chirality. An increase in de-pinning field as anisotropy is applied parallel to the wire and a decrease with the anisotropy applied perpendicular to the wire.

The modelling described in this section suggests that application of uniaxial anisotropy to a notched wire can have a significant influence on the de-pinning field and on the de-pinning mechanism of a transverse domain wall with changes in de-pinning field up to 175% seen in the 100 nm wide wire for the ‘up’ chirality. The width of the wire and type of notch both have significant effects on the pinning and de-pinning mechanisms of transverse head to

head domain walls. As the mechanisms of pinning and de-pinning were so different the results do not show the optimum wire dimensions to maximise this effect. Because the symmetrical square notch and triangular notch with domain wall in the 'down' chirality did not show switching between de-pinning and nucleation as a switching mechanism and the de-pinning field varied linearly with applied anisotropy these geometries would be best suited for devices utilising this effect.

6.2 – Experimental Measurement

6.2.1 - Experimental Measurement of Domain Wall De-pinning In Notched Wires

In order to experimentally observe the effect of strain on notched wire systems a device prepared by Andrew Rushforth's group at Nottingham University was analysed. These wire widths used in these wires were wider than those described above (100 nm – 1000 nm) and so it was expected that the domain walls in these wires would be vortex walls rather than transverse walls.

The piezoelectric component used in the device is a PZT stack manufactured by Piezomechanik. The poling direction of the PZT layers in the stack is perpendicular to the internal electrodes which are coupled to supply electrodes on opposite sides of the stack in order to apply an electric field to the PZT layers. An image of a PZT stack and schematic of the internal structure can be seen in Fig.6.26.

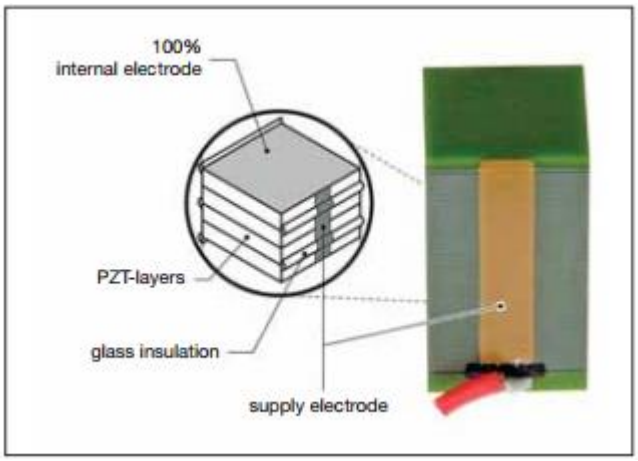

Fig.6.26 – Image of a Piezomechanik PZT stack showing supply electrode and a schematic of the internal structure of a stack. [12]

The notched wire nanostructures were manufactured on a silicon substrate by electron beam lithography, sputtering and lift off. The silicon substrate was then coupled to the PZT stack using epoxy. The device had a range of notched wire structures of 10nm thick sputtered cobalt with a 3nm Pt seed layer and a 3 nm thick Pt capping layer as oxidation protection. Each structure consisted of a circular nucleation pad with a diameter of 10µm and a 20µm long wire containing a triangular notch at its midpoint and a tapered end as shown in Fig.6.27. The wires had widths of 100, 200, 300, 500 and 1000nm and notch depths of 0, 20, 50 and 75%.

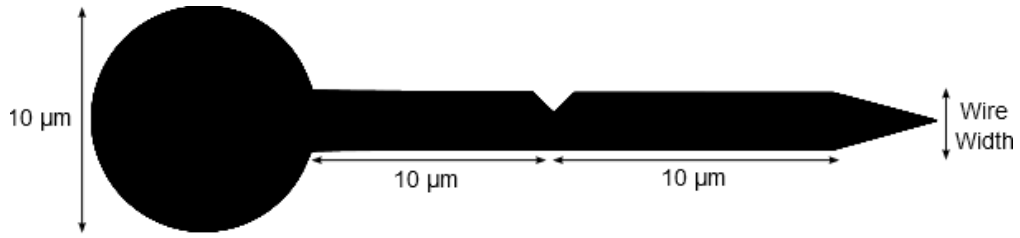

Fig.6.27 – Diagram of showing dimensions used in the manufactured notched wire and pad structures.

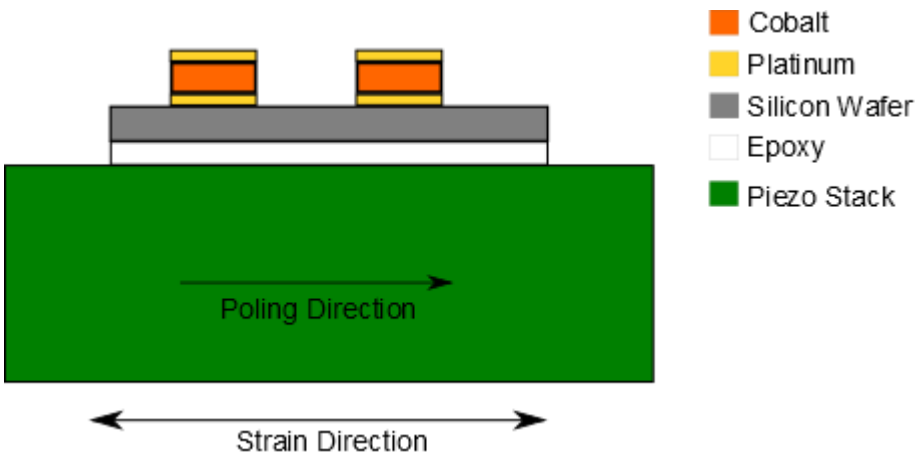

Fig.6.28 – Schematic of the layer structure of the device prepared at Nottingham University. (Note that while only two structures are shown the actual device has many).

Applying a voltage to the contacts on the piezoelectric transducer induces strain in the stack. Each layer is mechanically coupled to the next resulting in a strain in the Co nanostructures when the voltage is applied. The efficiency of this device will be reduced compared to a device with nanostructures patterned directly onto a piezoelectric substrate due to strain relaxation in the epoxy and silicon layers. The effects of strain relaxation were minimised by use of 150 µm thick silicon wafer.

Even though the efficiency of this design is lower than that offered by direct application of structures onto a piezoelectric substrate it offers significant advantages in terms of construction of the device. Use of commercial silicon wafer substrates ensures the low surface roughness required for deposition of nanostructures and is well established as a substrate for use in EBL and sputtering processes requiring no special treatment.

When an increasing magnetic field was applied to this structure along the wire axis the magnetisation in the nucleation pad reverses first due to the large nucleation volume it has compared to the wire, as the field increases further a domain wall is ‘injected’ into the wire

at the junction of the wire and pad. The domain wall propagates along the wire due to the applied field and provided the injection field is below the de-pinning field for the domain wall at the notch it will be pinned at the notch. When sufficient field is applied to overcome the magnetostatic interaction of the domain wall with the notch it will de-pin from the notch and propagate through the rest of the wire completing the magnetic reversal of the structure. By measuring the magnetisation of the wire segment after the notch the de-pinning fields of domain walls can be measured; the field at which this segment reverses magnetisation is the de-pinning field for that domain wall. The injection field can also be measured by measuring the field at which the wire segment before the notch reverses magnetisation. These regions are shown schematically on Fig.6.29.

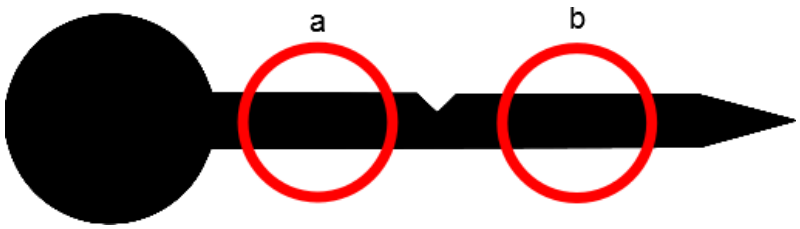

Fig.6.29 – Diagram of a notched wire and pad with measuring regions highlighted. a) Region for measurement of injection field. b) Region for measurement of de-pinning field.

By applying various voltages to the piezoelectric transducer the structures can be strained in order to induce a uniaxial magnetic anisotropy. Any effect of this on the de-pinning of domain walls can then be measured using focussed MOKE. From the finite element analysis already discussed it is expected that a strain induced uniaxial anisotropy will have a measurable effect on the de-pinning behaviour of domain walls and that in wires with asymmetric notches, such as the ones on this device, the chirality of the domain wall plays an important role in the resulting behaviour. Due to the width of the wires on this device it is expected that the domain walls formed will be vortex walls rather than the transverse walls discussed previously. Finite difference analysis performed in OOMFF by Andrew

Rushforth suggests that the de-pinning behaviour investigated the effect of the chirality of vortex walls. The wires in these simulations had widths of 1 µm, were 11 µm in length and had triangular notches in the centre of either 500 nm or 750 nm depth. Head to head vortex domain walls of both chiralities were initialised to the left of the notch and a ramping field was applied along the long axis of the wire to drive the domain wall into the notch and de-pin it. The edges at the ends of the wires had conditions applied negating their magnetostatic contributions in order to prevent the domain walls from interacting with the wire ends. Uniaxial anisotropy was applied perpendicular to the long axis of the wires. Data from these simulations is shown in Fig.6.30.

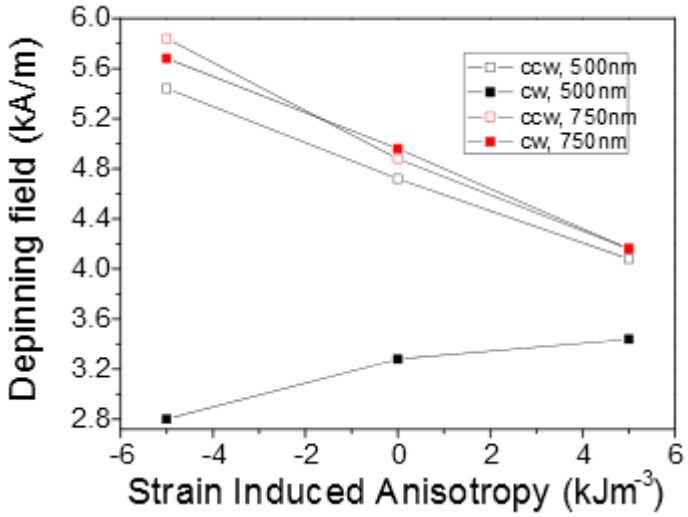

Fig.6.30 – Simulated de-pinning fields for clockwise (cw) and counter-clockwise (ccw) vortex walls (simulations performed by Andrew Rushforth).

Fig.6.30 shows that applying anisotropy to a notched wire alters the de-pinning field of a vortex domain wall. The results suggest that as positive anisotropy is applied perpendicular to the long axis of the wire vortex walls with magnetisation oriented both clockwise and counter clockwise with respect to a wire with the notch in the top of the wire will have their de-pinning field reduced for a notch depth of 750 nm (75%). For a notch depth of 500 nm (50%)the simulations show a decrease in de-pinning field with increasing anisotropy for

the counter clockwise chirality but an increase in de-pinning field for the clockwise chirality. The de-pinning fields are also significantly lower for the clockwise chirality for the 500 nm notch depth. This suggests that the de-pinning mechanism for the two chiralities are different.

Images from these simulations show that the two chiralities interact with and de-pin from the notch very differently.

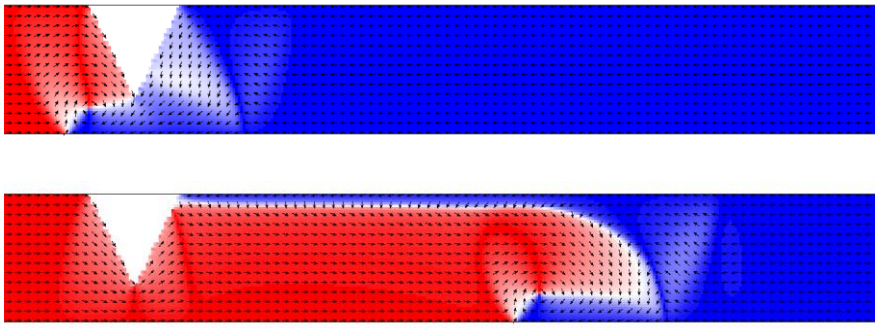

Fig.6.31 – Simulated pinning and de-pinning of clockwise head to head domain wall (simulations performed by Andrew Rushforth).

Fig.6.31 shows the case of a clockwise domain wall. The vortex core is pinned near the bottom of the notch as the moments in the wall are aligned with the edge of the notch reducing magnetostatic energy. As the domain wall de-pins the core moves through the notch and along the wire.

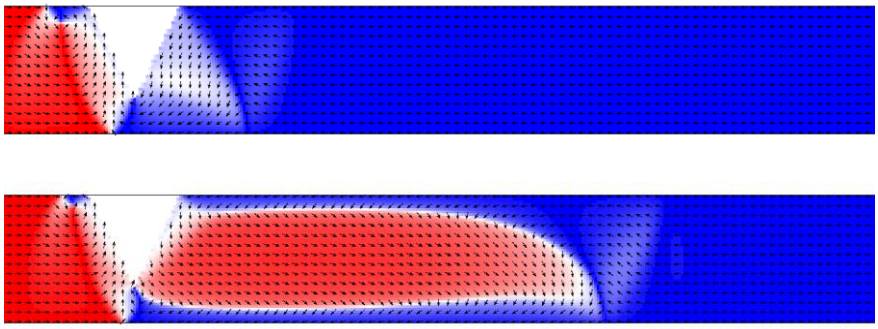

Fig.6.32 – Simulated pinning and de-pinning of counter-clockwise head to head domain wall (simulations performed by Andrew Rushforth).

Fig.6.32 shows the case of a counter-clockwise vortex wall. The core pins near to the top of the notch in order to minimise magnetostatic energy. The energy barrier to move the core through the notch is thus higher and so a new domain is nucleated after the notch with a transverse like character. At the nucleation field for the new domain the vortex wall remains pinned before the notch even though the magnetic reversal after the wire means that it has effectively de-pinned. The stray field from the pinned domain wall significantly lowers the field required to nucleate the new domain wall after the notch and the wire reverses at a lower field than is required to de-pin a vortex wall with the opposite chirality.

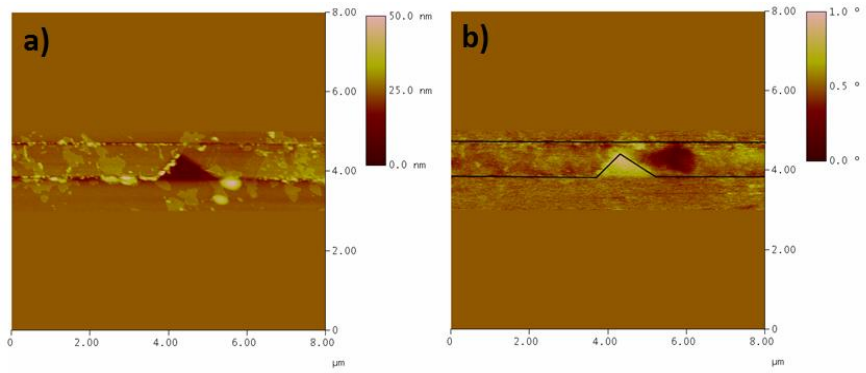

Fig.6.33 – a) AFM image of notched section of wire 1000nm width 75% notch depth. b) MFM image at the same notch.

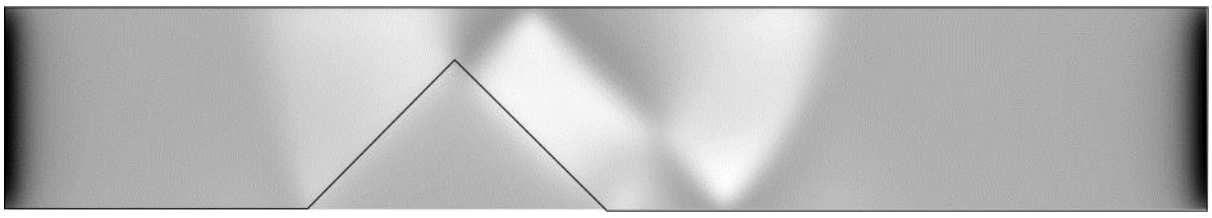

Fig.6.34 – Simulated MFM image of anti-clockwise domain wall pinned at a triangular notch. 1000 nm wire width, 75% notch depth.

Fig.6.33 shows an AFM and MFM image of one of the notched wire structures with dimensions 1000nm width and 75% notch depth. Comparing the MFM image to the simulated MFM data in Fig.6.34 appears to confirm the presence of a vortex domain wall in the wire which is consisent with the type of wall expected for these wire dimensions.

6.2.2 - Structure 1: 1000nm wide, 75% notch depth.

Structure 1 was a wire with a width of 1000 nm and a 75% notch depth oriented such that strain from the piezoelectric stack was applied perpendicular to the long axis of the wire. Whenever measurements were taken over a range of voltages an initial voltage of 60 V was applied then the voltage was reduced and measurements taken at each desired voltage. This was done to avoid taking measurements at different sections of the hysteresis curve of the piezoelectric stack.

In order to ensure that domain walls were pinning at the notch the injection fields for this structure were measured by probing the structure at site a shown in Fig.6.29 using focussed MOKE. A field sweep rate of 27 Hz was used and multiple hysteresis loops were measured and averaged to produce the averaged loops shown in Fig.6.35.

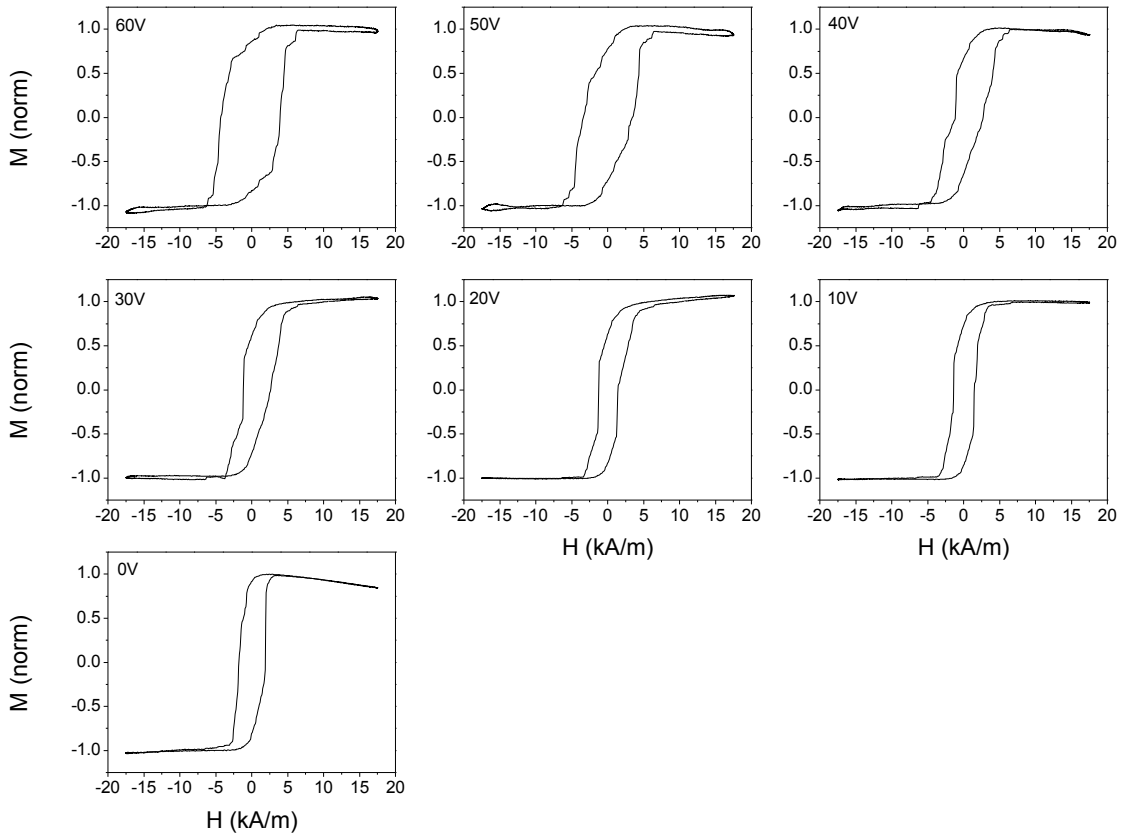

Fig.6.35 – Averaged domain wall injection hysteresis loops for structure 1. Measurements taken at site a as shown in Fig.6.29.

For each of these hysteresis loops the points at the beginning and end of switching have been identified and the midpoint on the line joining them calculated to give a value for the injection field. Since each hysteresis loop contains a switching field for both positive and negative field two injection fields are calculated per hysteresis loop, the average of these were taken for each loop and plotted against applied voltage in Fig.6.37.

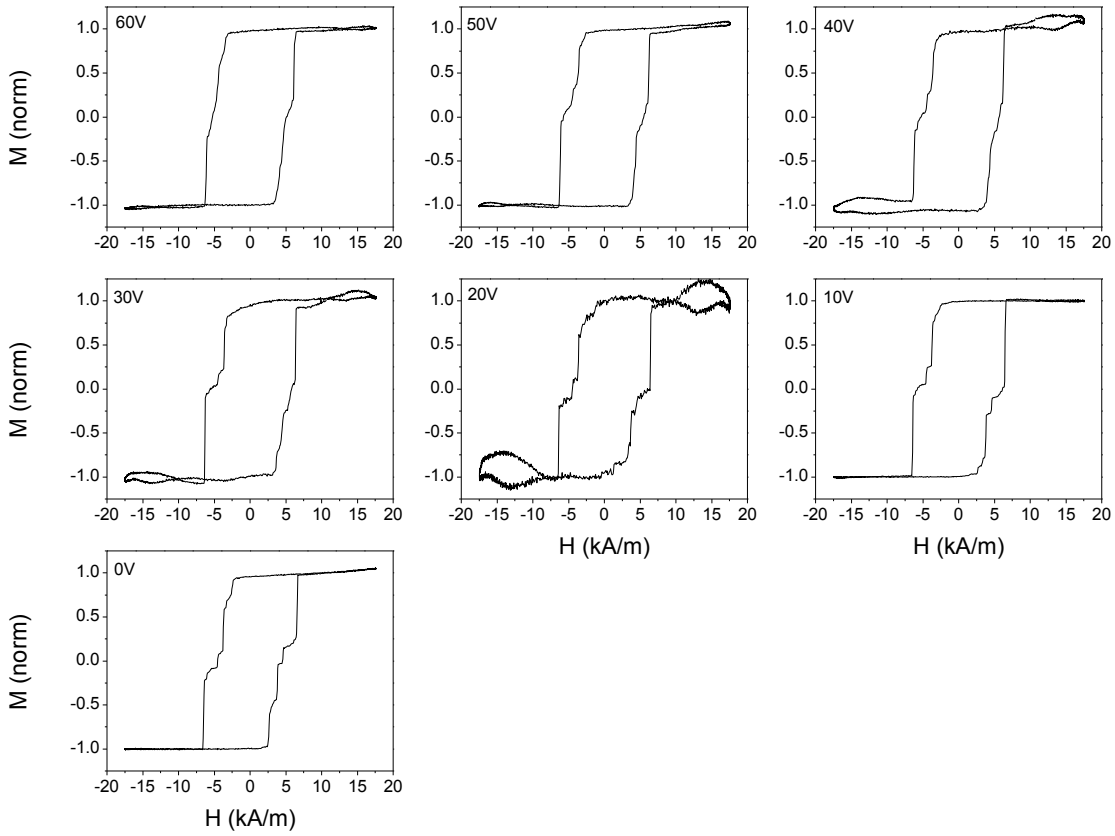

Fig.6.36 – Averaged domain wall de-pinning hysteresis loops for structure 1. Measurements taken at site b as shown in Fig.6.29.

Fig.6.36 shows averaged hysteresis loops for structure 1 probed at site b as shown in Fig.6.29. The loops show double switching, as would be expected of chirality dependent switching, however there it appears that each chirality exhibits a range of de-pinning fields. Since the simulated data is calculated for perfectly smooth wires it cannot account for the many small variations in pinning behaviour that a real domain wall can exhibit due to the edge roughness of the wire. As the de-pinning field of a domain wall is dependent on the structure of the pinned wall at the notch these small variations should account for the multiple de-pinning fields shown in these loops. Some of the switching was not sharp which

indicates the presence of many possible small variations in structure resulting in a tightly grouped range of de-pinning fields. Where the switching was sharper the switching was better defined.

Similarly to the data in Fig.6.35 the switching fields have been determined from the data in Fig.6.36 by finding the midpoint on each switching event. This results in between three and five de-pinning fields for each half of each hysteresis loop. Averages have been calculated for each loop by assuming that there are two main modes of switching for this structure, one for each chirality, and grouping the fields accordingly before taking the averages which have been plotted in Fig.6.38.

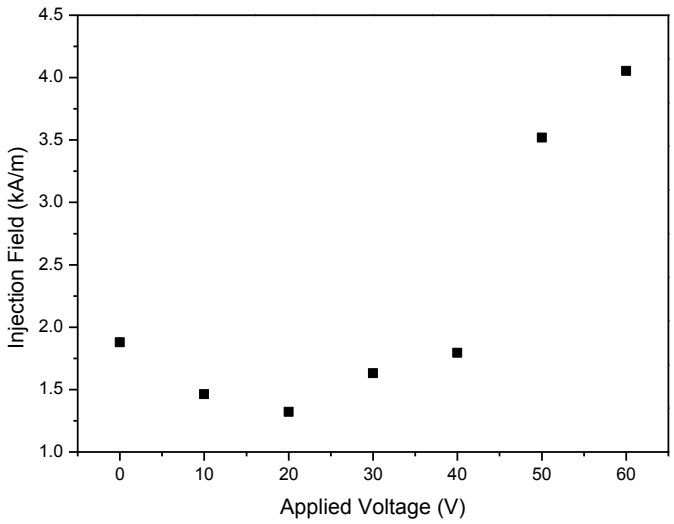

Fig.6.37 – Domain wall injection fields as a function of applied voltage for structure 1 (1000nm wide wire, 75% notch depth). Measurements taken at site a as shown in Fig.6.29.

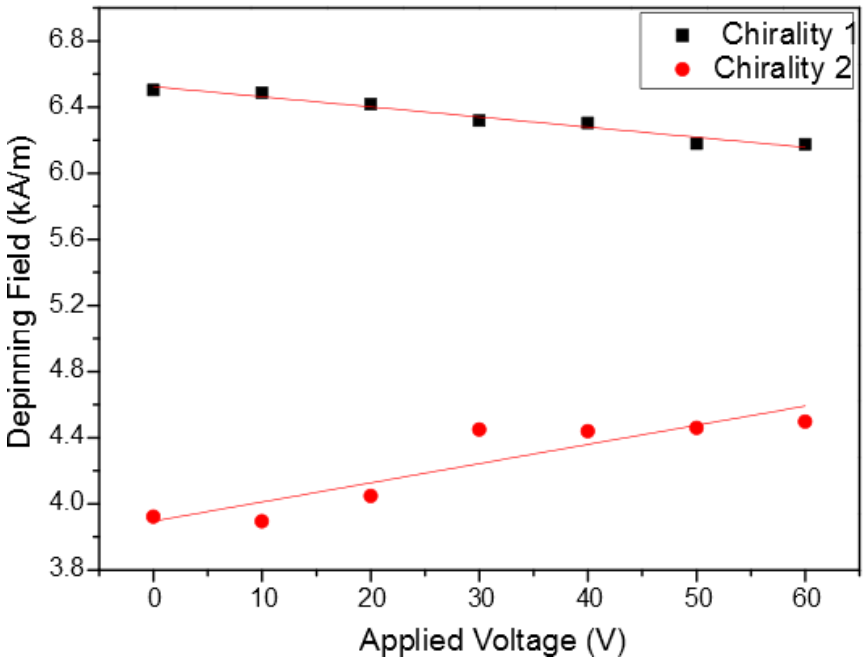

Fig.6.38 – Average de-pinning fields taken from averaged hysteresis loops of structure 1 (1000nm wide wire, 75% notch depth). As this data is consistent with the behaviour expected for clockwise and anticlockwise vortex walls it is assumed that the two data sets represent the two chiralities.

Fig.6.37 shows that as voltage is increased the injection field reduces from 1.9 kA/m to 1.4 kA/m as voltage increases from 0V to 20V, then as voltage is increased to 60V the injection field increases to 4.1 kA/m. Since this section of the wire is symmetrical, no chirality dependence on the injection field is expected.

Fig.6.38 shows that the de-pinning fields for domain walls follow the trend predicted by the finite element analysis (see Fig.6.30). Transitions at higher fields can be made to occur at lower fields by applying anisotropy to the structure. Transitions at lower fields can be made to occur at higher fields by applying anisotropy. In both cases the trend seems to be linear, particularly in the higher field de-pinning. Since this effect is so consistent with the predicted effects it is assumed that clockwise vortex walls are responsible for the de-

pinning data at higher fields and that anti-clockwise vortex walls are responsible for the data at lower fields. According to the linear fitting functions the de-pinning field of the clockwise domain walls reduces at a rate of 6.2 A/m/V and the anti-clockwise domain wall de-pinning field increases at a rate of 11 A/m/V.

The lowest de-pinning field for an applied voltage of 60V, is below the measured injection field at this applied voltage (see Fig.6.37) suggesting that this point may not in fact represent a de-pinning event but instead be due to an injected domain wall passing directly through the notch. The lowest de-pinning field for an applied voltage of 50V is close to the injection field at this applied voltage (see Fig.6.37) and so it is possible that this also represents a domain wall passing through the notch without pinning. All other points in Fig.6.38 are distinct from the injection fields in Fig.6.37 and so appear to be due to domain walls de-pinning from the notch.

Fig.6.39 shows an example of a single shot loop from this structure. Each single shot loop contains data from one field cycle resulting in a square loop with two coercivities each representing a de-pinning field. The single shot loops such as the one shown in Fig.6.39 also exhibit a linear offset which must be taken into account when analysing them. In order to process a large number of these loops a python script was used which introduces a linear correction into the data, identifies the forward and reverse field sweeps and for each sweep calculates a value for coercivity by finding the x intercept of a linear equation passing through the two points either side of the field axis. The values from the single shot loops were then binned and plotted in histograms which are shown in Fig.6.40.

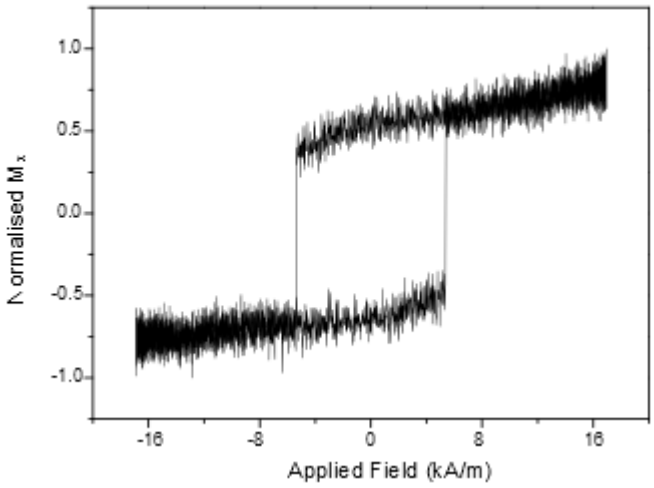

Fig.6.39 – Example of a single shot loop from structure 1 (1000nm wide wire, 75% notch depth) probed at site b as shown in Fig.6.29. Switching fields in this loop are caused by domain wall de-pinning.

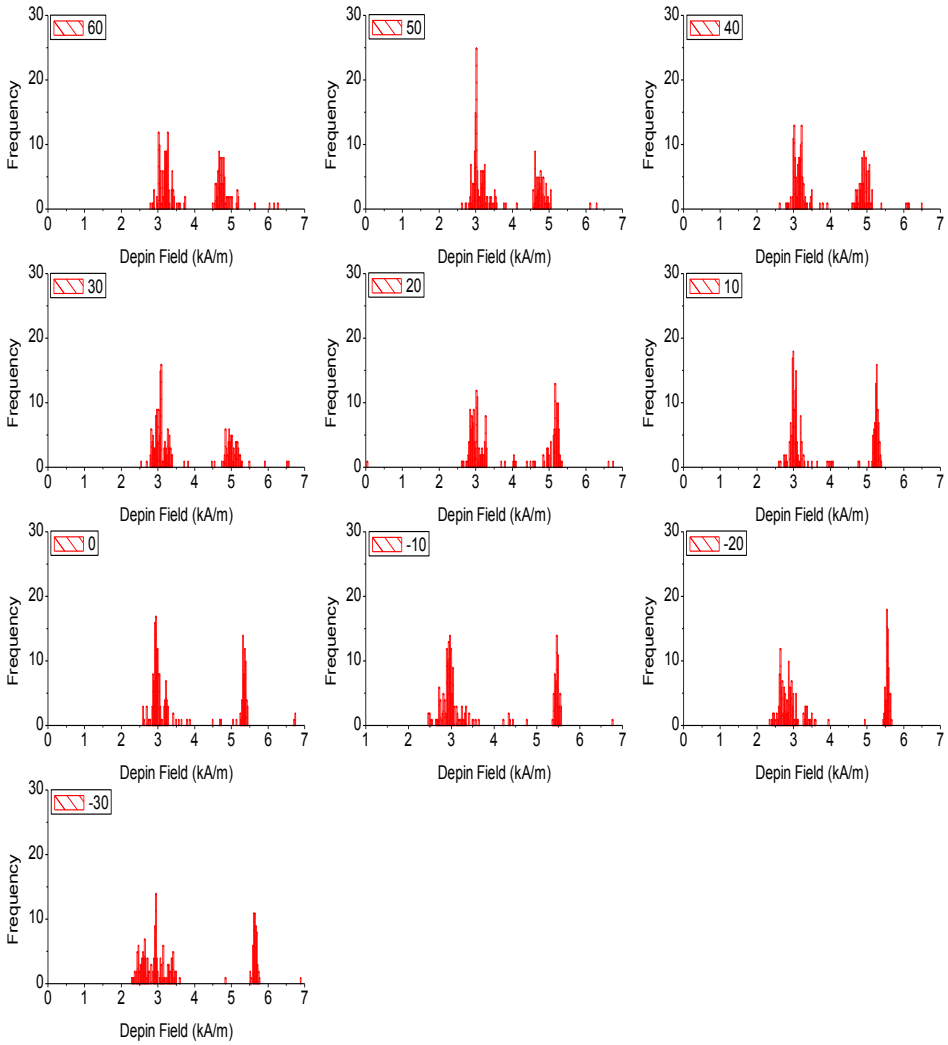

Fig.6.40 – Histograms showing binned one shot data from structure 1 (1000nm wide wire, 75% notch depth).

The histograms in Fig.6.40 show two distinct regions of peaks which is consistent with the interpretation that the two chiralities of domain wall behave differently. The data in each of these two regions has been averaged and plotted in Fig.6.41. For each average bars are plotted to indicate the value of the 10th and 90th percentile value such that 80% of the measured values fall between the bars.

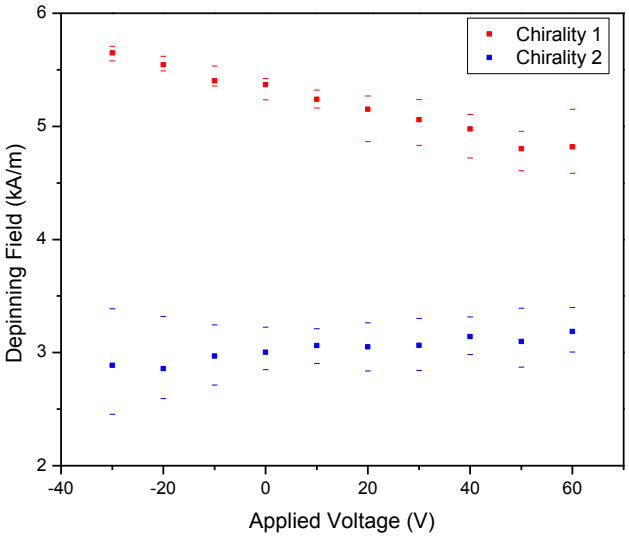

Fig.6.41 – Averaged de-pinning fields calculated from single shot data of structure 1 (1000nm wide wire, 75% notch depth) with 10th and 90th percentile bars.

The data in Fig.6.41 also matches extremely well with the predicted values from the finite element analysis producing the same trends as shown in Fig.6.38. According to the linear fitting functions the de-pinning field of the clockwise domain walls reduces at a rate of 9.6 A/m/V and the anti-clockwise domain wall de-pinning field increases at a rate of 3.28 A/m/V. These values from Fig.6.38 do not match exactly but are both within an order of magnitude and reasonably close taking error bars into account. It can also be seen that the application of anisotropy affects the spread of the de-pinning fields. This is most apparent in the higher de-pinning field where an increase in applied anisotropy increases the range between the 10th and 90th percentile, whereas in the lower de-pinning data decreasing the applied anisotropy increases the range for voltages below 10V and seems to have little effect for voltages above 10V.

The single shot data shown in Fig.6.41 also shows that the two chiralities' trends for change in de-pinning field with application of voltage to the device extend to the application of

negative voltage resulting in compressive strain on the device and application of anisotropy perpendicularly to the anisotropy resulting from a tensile strain.

6.2.3 - Structure 2: 1000nm wide, 75% notch depth.

Structure 2 was a wire with a width of 1000 nm and a 75% notch depth oriented such that strain from the piezoelectric stack was applied perpendicular to the long axis of the wire. Fig.6.42 shows averaged hysteresis loops for structure 2 taken at site b as shown in Fig.6.29 using focussed MOKE with a field sweep rate of 27. The loops in Fig.6.42 show fewer switching modes and sharper switching than those in Fig.6.36 and so it was decided that it may provide a clearer study of the effect of chirality on the domain wall behaviour as it is assumed that this structure exhibits less of the additional complexity caused by variations in domain wall structure caused by edge roughness.

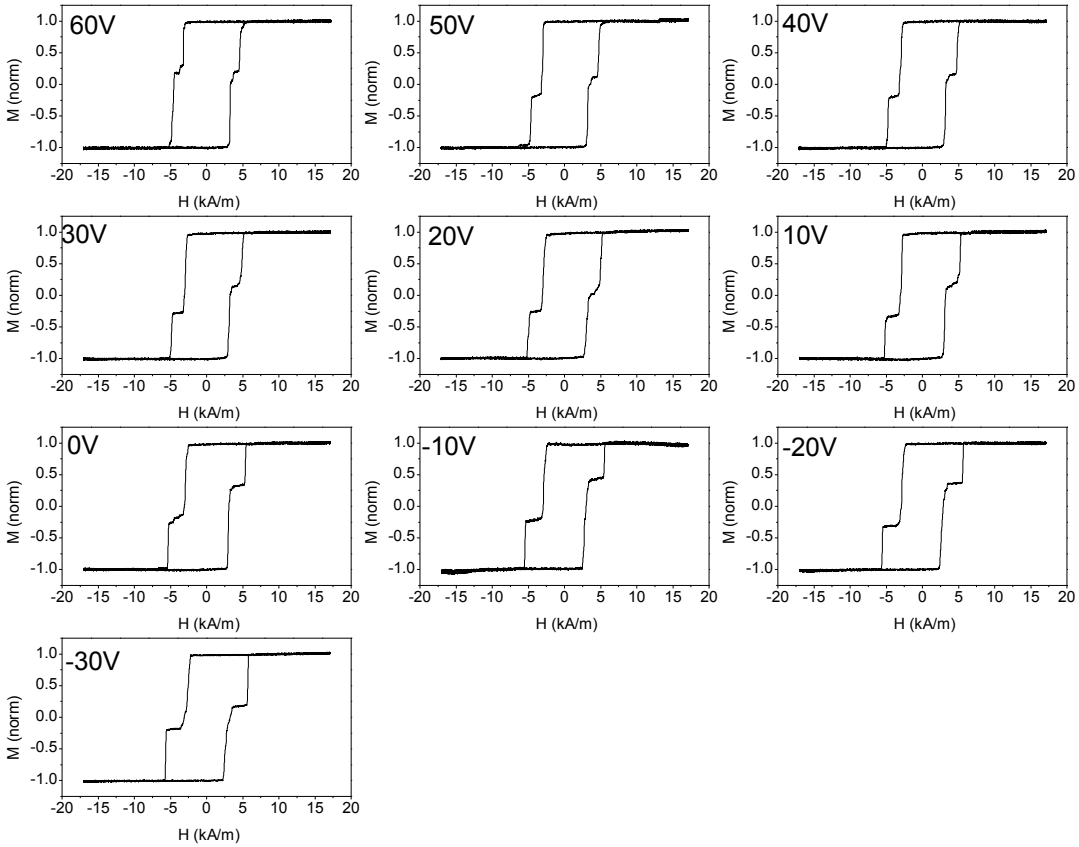

Fig.6.42 – Averaged hysteresis loops for structure 2 (1000nm wide wire, 75% notch depth). Measurements taken at site b as shown in Fig.6.29.

Using the same method as was used for the loops in Fig.6.36 de-pinning fields were taken from the loops in Fig.6.42 and have been plotted in Fig.6.29. Due to the sharper switching and the lower number of switching events in each loop each half of each loop provided fewer de-pinning fields than were found for structure 1 resulting in less need to average groups of fields.

As the switching for this structure is well defined in comparison to structure 1, the loops show a distinct double switching shape. Note that as each loop is an average of many

individual loops of the sort shown in Fig.6.39 the double switching is caused by the differing switching fields of the two chiralities. The average switching field for each chirality is given by the switching events on each side of the step.

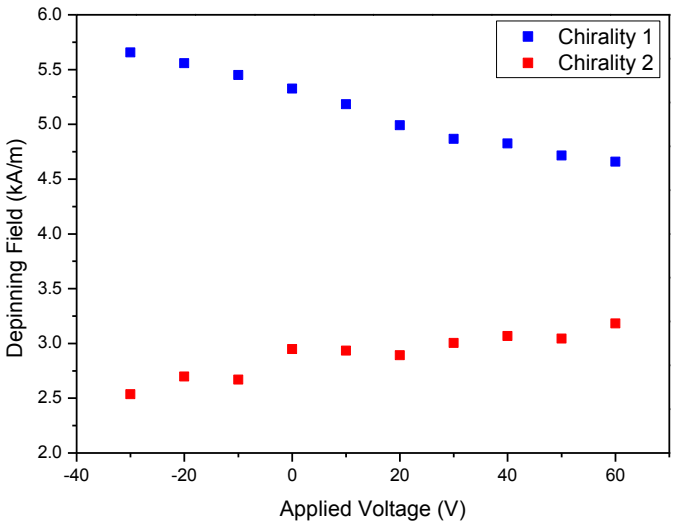

Fig.6.43 - Average de-pinning fields taken from averaged hysteresis loops of structure 2 (1000nm wide wire, 75% notch depth).

The data in Fig.6.43 once again show the behaviour predicted by the finite element analysis with the low de-pinning fields tending to increase with applied voltage and the high de-pinning fields to decrease with applied voltage. According to the linear fitting functions the de-pinning field of the clockwise domain walls reduces at a rate of 12 A/m/V and the anti-clockwise domain wall de-pinning field increases at a rate of 6 A/m/V.

Once again single shot measurements were taken in order to plot the distribution of de-pinning fields for this structure. In order to test for any hysteresis in the piezoelectric behaviour of the actuator the voltage was cycled from -60V up to 30V and back down to -60V. If any hysteresis in the actuator is present it is expected that the return pass will not follow the same de-pinning fields as the initial pass due to the residual strain in the device.

It is expected that if residual tensile strain remains in the device after a voltage sweep form low to high voltage the applied anisotropy will be higher when the voltage is swept back down resulting in higher de-pinning fields for clockwise vortex walls and lower de-pinning fields for anti-clockwise vortex walls than would be measured at the same voltages during the upwards voltage sweep. The de-pinning field for these single shot measurements have been determined using the python script described above and are displayed in the histograms shown in Fig.6.39.

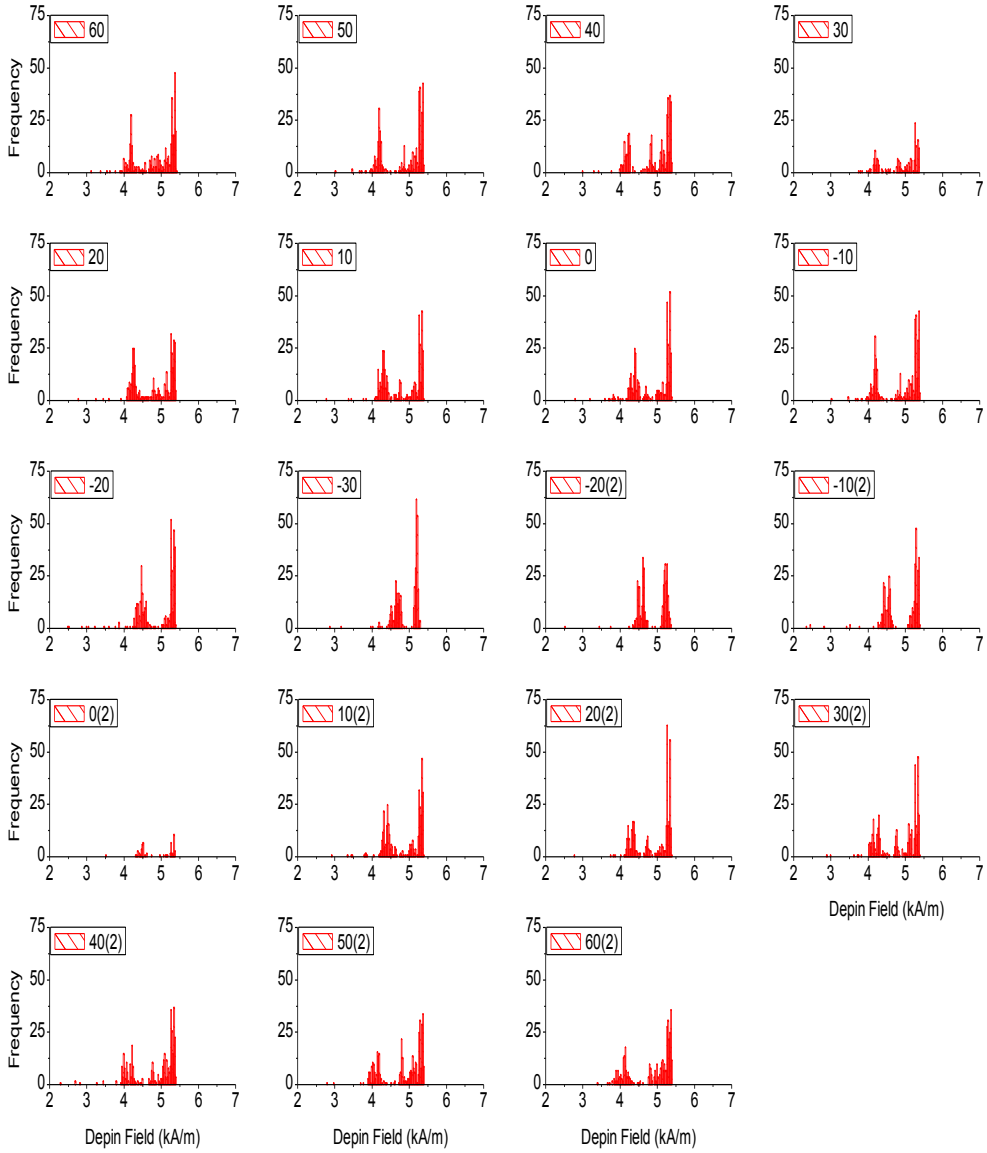

Fig.6.44 - Histograms showing binned one shot data from structure 2 (1000nm wide wire, 75% notch depth).

Fig.6.45 shows an attempt to separate the single shot data into the data for the two chiralities and take averages. The data in Fig.6.44 does not show such well defined separation of chiralities as in Fig.6.40. It was expected that structure 2 would show more

well defined peaks however these measurements were made some time after the measurements in Fig.6.40 and Fig.6.42 and so the data may include more noise due to a lower quality set up of the focussed MOKE or the sample may have sustained some minor damage in the intervening time increasing the edge roughness of the structure.

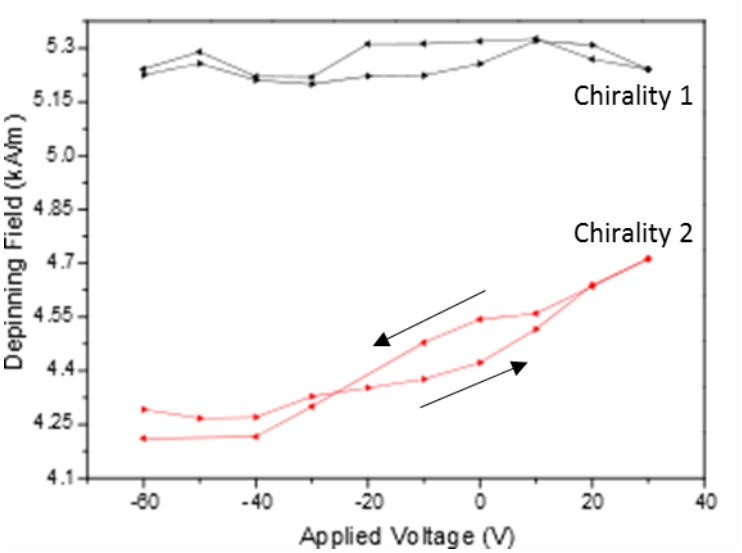

Fig.6.45 - Averaged de-pinning fields calculated from single shot data of structure 2 (1000nm wide wire, 75% notch depth). Direction of triangles indicate direction of voltage sweep.

Fig.6.45 shows the averages calculated from the single shot data of structure 2. The trends for the high de-pinning fields do not seem to show a correlation with applied voltage however the low de-pinning fields show an increase in de-pinning field with applied voltage. The lower de-pinning fields are also higher than those in Fig.6.43 which would suggest a change in the shape of the wire in the time between the measurements being taken, perhaps some damage resulting in an increase in edge roughness.

There does appear to be some hysteretic effect present in the device after the sweep reverses from -30 back up to 30V with de-pinning fields remaining higher than on the forwards sweep due to residual strain in the piezoelectric transducer. This trend and the linear trend of the change in de-pinning field does not seem to apply between 40V and 60V

which also suggests that the applied voltages may be oppositely signed since the piezoelectric transducer is not designed to be used at voltages below -30V.

In an attempt to identify the full range of de-pinning fields for this structure the multiple peak fitting tool in OriginPro[13] was used to identify peaks in the histogram data. An example of the peak analysis is shown in Fig.6.46.

Peak Analysis

Data Set:% ([Book1]FitPeaks1,@WL,Input.IDTR1.IDTC2) Date:29/07/2015

BaseLine:End Points Weighted

Chi^2=-- Adj. R-Square=-- # of Data Points=% ([Book1]FitPea

SS=-- Degree of Freedom=% ([Book1]FitPeaks1,@WL,RegStats.C1.DOF)

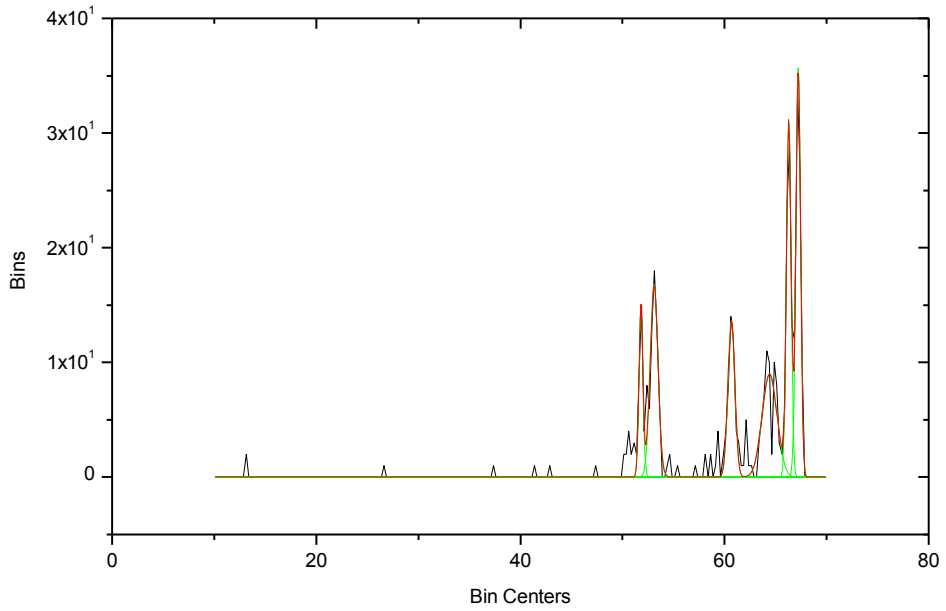

Fitting Results

Peak Index	Peak Type	Area Intg	FWHM	Max Height	Center Grvty	Area IntgP
1	Gaussian	7.49409	0.46956	14.99313	51.81565	8.35756
2	Gaussian	16.23951	0.90964	16.77147	53.09738	18.11063
3	Gaussian	11.4793	0.79312	13.59697	60.67667	12.80195
4	Gaussian	16.33675	1.70586	8.99686	64.40988	18.21908
5	Gaussian	17.52673	0.53309	30.88657	66.29898	19.54617
6	Gaussian	20.59199	0.54274	35.6429	67.21704	22.9646

Fig.6.46 – Example peak fitting data for structure 2 (1000nm wide wire, 75% notch depth).

Each histogram was analysed in this way using the bin centres and frequencies as the points of the data to be fitted. Due to the way the data is bunched together at the high de-pinning fields the peak analysis tool was not able to converge on a solution for some of the histograms. Because of this not every histogram's data is represented in Fig.6.47 and Fig.6.39.

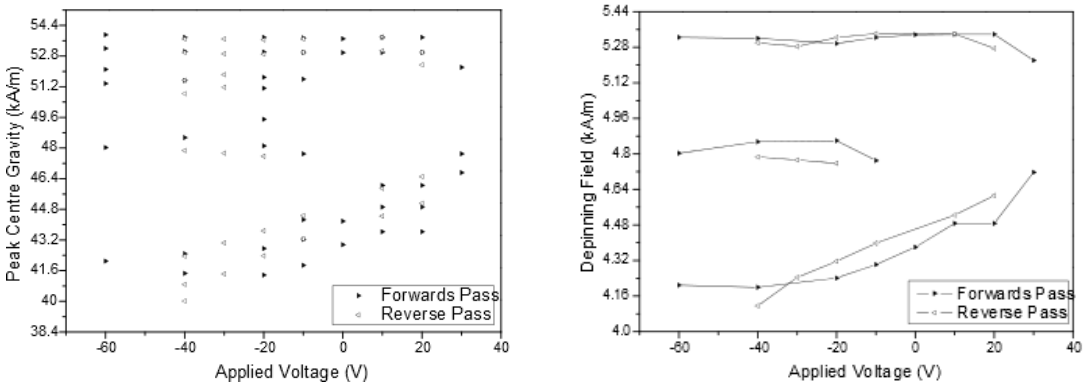

Fig.6.47 and Fig.6.48 - Left: Peak centre gravities from peak fitting. Right: Averaged peak fitting data for structure 2 (1000nm wide wire, 75% notch depth). Direction of triangles indicate direction of voltage sweep. Triangles pointing left are measurements made during the initial upwards voltage sweep and triangles pointing right are measurements made during the subsequent downward voltage sweep.

Fig.6.47 shows the peak centre gravities from the peak fitting data for structure 2. Each peak would represent a de-pinning mode and the peak centre gravity represents the average value of the de-pinning field for that mode. These data also shows change in the high de-pinning fields due to applied voltage. This analysis also reveals an intermediate set of de-pinning fields at 60 Oe which are not affected by the applied voltage. The linear increase in de-pinning field with increase in applied voltage appears to be present for the lower de-pinning fields.

In order to separate the three main modes from Fig.6.47 the centre gravities were separated into three groups and averaged with each centre gravity weighted by its max height. These averaged values are plotted in Fig.6.48.

Fig.6.48 also shows no change in the high and intermediate de-pinning fields with applied voltage. The low de-pinning fields follow the same trend as was observed in Fig.6.29 and the data for structure 1. The hysteretic effect observed on Fig.6.45 is also present suggesting that residual strain in the piezoelectric transducer had an effect on the behaviour of the device resulting in higher de-pinning field for clockwise domain walls as applied voltage was ramped down from high to low. Due to the quality of the data for the counter clockwise domain walls' de-pinning fields it is unclear what effect hysteresis in the piezoelectric transducer had on these domain walls.

6.2.4 - Structure 3: 1000nm wide, 50% notch depth.

In order to analyse the effect of a shallower notch on the change in de-pinning fields due to anisotropy structure 3 with dimensions 1000 nm wire width and 50% notch depth was analysed. Since the domain walls interact with a notch magnetostatically it was expected that the domain walls would interact less strongly with a shallower notch and so the change application of anisotropy would have less effect on the domain walls.
Single shot measurements were taken and analysed using the python script described above. Histograms of this data are presented in Fig.6.49.

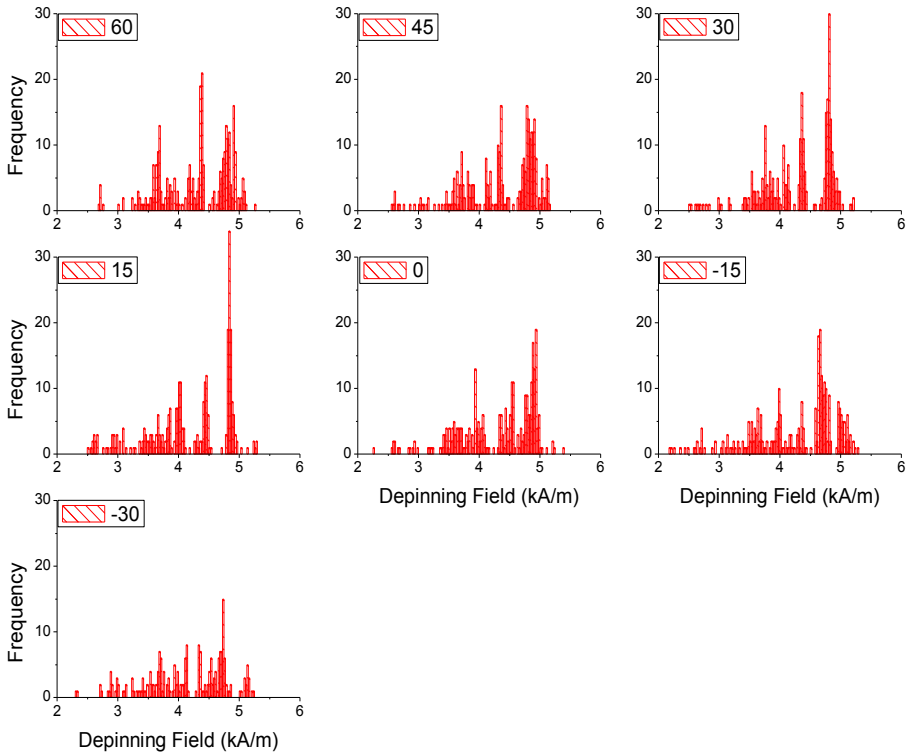

Fig.6.49 - Histograms showing binned one shot data from structure 3.

The data in Fig.6.49 do not clearly show separate regions for the two chiralities of domain walls and more de-pinning modes are present than were observed in structure 1 and structure 2. Therefore it is necessary to identify the peak locations in order to observe the trends in this data.

The ranges for each of the peaks were found and the de-pinning values in each of these ranges was averaged to calculate an average de-pinning field for each de-pinning mode. These averaged have been plotted in Fig.6.50.

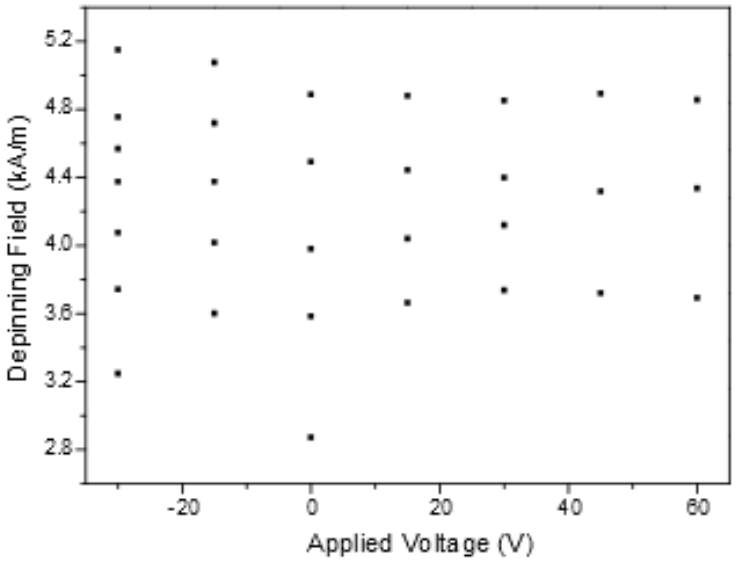

Fig.6.50 - Averaged de-pinning fields calculated from single shot data of structure 3.

The data in Fig.6.50 shows the same trend for change in de-pinning field as was observed in the structures with 75% notch depth, however the effect of the applied anisotropy is not as strong for the smaller notch depth of 50%. It is also clear that the difference in de-pinning field for the two chiralities is lower than it was for the 75% notch depth to the point that de-pinning modes with intermediate de-pinning fields for the two chiralities appear to converge at voltages above 45V.

The pinning of a domain wall at a notch is a magnetostatic interaction which depends on the structure of the domain wall and the size and shape of the notch. By reducing the size of the notch the strength of this interaction is reduced and so changes in the domain wall structure due to chirality or applied anisotropy have a smaller effect on the behaviour of the system.

6.2.5 - Structure 4: 500nm wide, 75% notch depth.

In order to determine the effects of a narrower wire width a 500 nm wide wire with a notch depth of 75% was analysed using focussed MOKE. Single shot measurements were taken at site b shown in Fig.6.29. The loops were analysed using the Python script described above, the de-pinning fields were binned, plotted as histograms and the ranges of the peaks identified. The averaged de-pinning field for each peak was calculated and plotted in Fig.6.51.

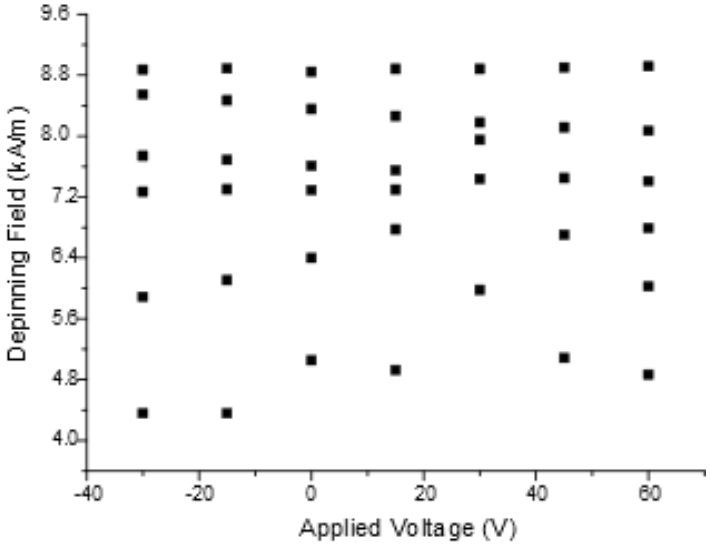

Fig.6.51 – Averaged de-pinning fields calculated from single shot data of structure 4 (500nm wide, 75% notch depth).

Fig.6.51 shows that applied voltage had no measurable effect on the higher de-pinning fields suggesting that there was no effect on clockwise domain walls. The lower de-pinning fields appear to show a small increase in de-pinning field with applied voltage. It is clear that the effect of the applied anisotropy is reduced for narrower wires. The reason for this is likely to be the reduced volume of the domain wall in the wire.

Note that the 1000 nm wide wire with 50% notch depth showed a greater effect. This suggests that the wire width is has a larger effect on the response to applied uniaxial anisotropy than the notch depth.

6.2.6 - Summary of Experimental Work

Notched Co nanowires deposited onto silicon wafer bonded to a piezoelectric stack were analysed using focussed MOKE to determine the effects of application of strain to the nanostructures by application of a voltage to the piezoelectric stack. The strain induced uniaxial magnetic anisotropy resulted in changes in the de-pinning fields of vortex domain walls from the wire notches which was dependent on the chirality of the domain wall. The domain walls can be differentiated because the vortex walls with moments oriented counter-clockwise pin with their core near the top of the notch and de-pin at higher fields and the vortex walls with their moments oriented clockwise pin at the bottom of the notch and de-pin at lower fields. This effect is greatest at the largest notch depth of 75%. Application of uniaxial magnetic anisotropy perpendicular to the wire long axis decreases the de-pinning fields of the counter-clockwise domain walls and increases the de-pinning fields of the counter-clockwise domain walls. This effect was greatest in the wires with 1000 nm wire width and 75% notch depth showing that wider wires and deeper notches produce the strongest effect. This is likely due to the larger domain wall volume interacting with the applied anisotropy and the larger notch interacting with the domain wall. The MOKE results for the 100 nm wide wires with 75% notch depth match well to the simulations performed by Andrew Rushforth suggesting that the effects observed are a result of applied uniaxial anisotropy and the chirality of vortex domain walls. MFM analysis suggests the presence of vortex domain walls in these structures.

A stronger effect could be seen in a device with nanostructures deposited directly onto a piezoelectric substrate preventing the strain relaxation which would be present in the device tested. Using a piezoelectric with a higher piezoelectric coefficient than PZT, such as PMN-PT could also produce a stronger effect as it would be possible to apply higher strains, the energy efficiency would also be higher as higher strains could be achieved for the same voltages. Using a magnetic material with high E and λ_s could also produce a stronger effect as the applied anisotropy would be higher for a given strain.

6.3 - Conclusions

Notched wires with widths of 50, 100 and 200 nm were simulated to determine the effect of uniaxially applied anisotropy to the de-pinning of a transverse head to head domain wall. It was shown that the chirality of the domain wall and the wire dimensions affected the simulated switching field and switching mechanism. The de-pinning field either increased or decreased with anisotropy applied perpendicularly to the wire or parallel and this was dependent on the pinning mechanism of the domain wall at the notch. The pinning mechanism was dependent on the chirality of the wall, the geometry of the notch and the width of the wire.

Notched Co nanowires were analysed using focussed MOKE to determine the de-pinning field of vortex domain walls from a triangular notch. Structures with dimensions of 1000 nm wire width and 75% notch depth, 1000 nm wire width and 50% notch depth and 500 nm wire width and 75% notch depth were tested. The results showed that the two chiralities of vortex walls de-pin at different fields and respond differently to uniaxial anisotropy applied perpendicular to the wire long axis. Application of uniaxial magnetic anisotropy perpendicular to the wire long axis increases the de-pinning fields of the clockwise domain walls and decreases the de-pinning fields of the anti-clockwise domain walls. This effect

was greatest in the wires with 1000 nm wire width and 75% notch depth showing that wider wires and deeper notches produce the strongest effect.

Both sections of this study suggest the devices could be produced which control domain wall de-pinning from a notch using strain induced anisotropy, however because the Co nanowires were so sensitive to the wire width it is possible that it would be difficult to produce a measurable effect from very narrow wires such as those in the transverse wall simulations.

6.4 - References

[1] D.Atkinson, *Appl. Phys. Lett.*, **92**, 022510 (2008)

[2] S.P.Parkin, *Science*, **320**, 190 (2008)

[3] D.A.Allwood, G.Xiong, C.C.Faulkner, D.Atkinson, D.Petit and R.P.Cowburn, *Science*, **309**, 1688 (2005)

[4] C. Faulkner, *J. Appl. Phys.*, **95**, 11, 6717 (2004)

[5] D.Petit, *J. Appl. Phys.*, **103**, 114307 (2008)

[6] J.Akerman, *Phys. Rev. B*, **82**, 064426 (2010)

[7] I.Polenciuc, A.J.Vick, D.A.Allwood, T.J.Hayward, G.Vallejo-Fernandez, K.O'Grady and A.Hirohata, *Appl. Phys. Lett.*, **105**, 162406 (2014)

[8] http://gid.cimne.upc.es/

[9] http://www.paraview.org/

[10] A.E.Clark, M.Wun-Fogle, J.B.Restorff, K. W. Dennis, T.A.Lograsso, and R.W.McCallum, *J. Appl. Phys.*, **97**, 10M316 (2005)

[11] J.Akerman, M.Muñoz, M.Maicas and J.L.Prieto, *Phys. Rev. B*, **82**, 064426 (2010)

[12] L.Pickelmann, Low voltage multilayer piezo-ceramic stacks, rings, chips, Piezomechanik GmbH

[13] http://www.originlab.com/

7 - Conclusions

First the effect of a strain induced magnetic anisotropy gradient on transverse domain walls in a soft magnetic nanowire was considered by approximating the system using a soft magnetic nanoring subjected to a uniaxial strain induced magnetic anisotropy. The ring approximates a curved wire and the uniaxial magnetic anisotropy creates a radial anisotropy gradient. As the effect of an in plane rotating magnetic field produces a well-defined response in the domain walls in magnetic nanorings in the onion state it was proposed that the perturbation from this behaviour would give a measure of the effect of the anisotropy gradient on the domain walls in the ring.

An analytical model was created which simulates the domain wall positions in the ring relative to a reference axis defined by the uniaxial anisotropy direction K_{app} for any direction of applied in plane magnetic field. This was achieved by calculating the energy minima for the system considering the magnetic anisotropy energy and the Zeeman energy of the system. The variables used in the model were the ring centre radius (r), the wire width (w), the domain wall width ($\pi\Delta$), the wire thickness (t), the saturation magnetisation of the material (m_s), the applied anisotropy (K_{app}) and the applied field (H). The model showed that applied anisotropy caused the domain walls to lag behind the applied field due to a change in the energy minimum positions in the ring. This effect was found to be greatest for small values of r, large values of w, small values of m_s large values of K_{app} and small values of H. The effect was found to be independent of t. Three regimens of domain wall behaviour were identified from the model. At low K_{app} it was found that the domain walls rotate full around the ring as the applied field is rotated, lagging behind the field direction. The degree of lag increases as the K_{app} is increased and the domain walls align with the field direction at every every 90° of field rotation. At intermediate K_{app} it was found that domain walls rotate fully around the ring lagging behind the field direction but no

longer align with the field direction every 90°. In this regimen it was found that the domain walls move around the ring with two discontinuities as the field is rotated. At high K_{app} the domain walls do not rotate fully around the ring as the field is rotated but oscillate around the K_{app} direction. The anisotropy thresholds for these three regimens were found to depend on a single anisotropy defined as K_t which is a function of r, w, m_s and H. This allowed generalised hysteresis loops of the ring system to be calculated.

Finite element modelling was used to simulate the system energy of a soft magnetic rings in the onion state with varying diameter (D) and wire width (w). The domain walls were pinned by an in plane applied magnetic field and in plane uniaxial anisotropy was applied at varying angles from the applied field. The energy of the system was found to follow a $\sin^2\theta$ relationship to the angle between the applied anisotropy and the applied field. Using a fitting function the maximum energy gradient for the system was calculated for each ring and this was used to calculate an effective driving field experienced by the domain walls in the system (H_{eff}). It was found that H_K was maximised for low valued of D and high values of w. This correlated with the findings from the analytical model suggesting that low values of r and high values of w maximise the effect of anisotropy on the system. A figure of merit for the thermal stability of the pinning of domain walls in an energy well caused by an anisotropy gradient was also calculated from the energies calculated by the finite element model. It was found that the thermal stability is expected to be highest for rings with large volumes and for rings with high values of w.

Initial MOKE measurements on an array of Ni rings showed that application of uniaxial strain to the rings distorted the measured hysteresis loops suggesting that induced anisotropy had altered the phase lag experienced by the domain walls rotating around the ring. These initial results are promising and further tests at lower applied field and higher applied voltages could provide improved results.

The work on this system has provided useful data regarding the optimisation of strain based control of domain walls in rings through appropriate choice of material and ring dimensions. The potential for well defined controllable domain wall energy minima has potential as a method of data storage and the results may also be useful in studying other systems such as straight wires with a magnetic anisotropy gradient.

Next the effect of a strain induced uniaxial anisotropy on the depinning of domain walls from notches in soft magnetic nanowires was considered.

Finite element modelling was used to simulate the depinning of transverse head-to-head domain walls from triangular notches in nanowires of various wire widths. The modelling showed that an applied in plane magnetic anisotropy changes the depinning field of the domain walls. The change in depinning field was dependent on the width of the wire, the magnitude of the applied anisotropy and the chirality of the domain wall. It was found that transverse head-to-head domain walls in the 'up' chirality (magnetisation in the domain wall oriented towards the edge of the wire containing the notch) pin to the side of the notch in 100 nm and 200 nm wide wires. Application of anisotropy perpendicular to the wire direction was found to increase the field required for depinning while anisotropy applied parallel to the wire direction was found to decrease the field required for depinning. It was also found that Anisotropy allied perpendicular to the wire decreased the field required for an alternative switching mechanism wherein a new domain is nucleated from the notch. It was found in the 100 nm wide wires that at a critical applied anisotropy the switching mechanism changes from depinning to nucleation of a reverse domain. For the 200 nm wide wire it was found that with no applied anisotropy the wire switches by nucleation of a reverse domain and at a critical applied anisotropy applied perpendicular to the wire the switching mechanism changes to domain wall depinning as the nucleation mechanism is suppressed. In 50 nm wide wires with domain walls in the 'up' chirality it was

found that the domain walls pin at the opposite side of the notch. It was found that applying anisotropy perpendicular to the wire increased depinning field linearly and anisotropy parallel to the wire decreased the depinning field linearly. The same trend was observed for 'down' chirality (magnetisation in the domain wall oriented towards the edge of the wire not containing the notch) transverse head-to-head domain walls in a 100nm wide wire and transverse head-to-head domain walls (chirality independent) in a 100 nm wide wire with a symmetrical square notch. This behaviour was attributed to energy well behaviour.

A device constructed by Andrew Rushforth's group at Nottingham University was analysed to observe the effect of uniaxial strain induced anisotropy on the depinning of domain walls from a triangular notch. The device consisted of notched Co nanowires with nucleation pads deposited on a Si substrate which had been mechanically coupled to a piezoelectric actuator. Voltage applied to the actuator was used to strain the structures. The depinning fields for domain walls injected into the wires from the nucleation pads were measured using focussed MOKE. It was found that some domain walls depinned at higher field and some at lower fields. It was found that application of voltage (producing strain perpendicular to the wire direction) reduced the depinning fields of the domain walls depinning at higher fields and increased the depinning fields of the domain walls that depinned at lower fields. The increase or decrease in depinning field followed a linear trend with the increase in voltage. It was shown that this effect was greatest for the widest wires tested (1000 nm wide) and for the deepest notches tested (75% notch depth). Finite element simulations performed by Andrew Rushforth suggested that the domain walls in wires of the dimensions tested (1000 nm wide and 500 nm wide) were vortex walls, MFM data from the sample appears to confirm this. Data from the simulations suggested that the chirality of the vortex walls is responsible for the differences in depinning behaviour with 'clockwise' vortex walls depinning at lower fields and increasing in depinning field with

applied voltage and ‘anti-clockwise’ vortex walls depinning at higher fields and reducing in depinning field with applied voltage.

The controllable domain wall depinning fields shown in this work offer the potential for improved predictability of domain wall movement in racetrack like memory or domain wall logic. The results presented also suggest possible ways to maximise the effect through appropriate choice of materials and geometry.